

©[2012]

Bumsu Lee

ALL RIGHTS RESERVED

**Functionalization of Organic Semiconductors and Other Carbon-based Materials by
Self-Assembled Monolayers (SAMs) and Charge Transport in Organic Field-effect
Transistors (OFETs)**

by

Bumsu Lee

A Dissertation submitted to the
Graduate School-New Brunswick
Rutgers, The State University of New Jersey

in partial fulfillment of the requirements

for the degree of

Doctor of Philosophy

Graduate Program in Physics

written under the direction of

Professor Vitaly Podzorov

and approved by

New Brunswick, New Jersey

May, 2012

Abstract of the Dissertation

Functionalization of Organic Semiconductors and Other Carbon-based Materials by
Self-Assembled Monolayers (SAMs) and Charge Transport in Organic Field-effect
Transistors (OFETs)

by

Bumsu Lee

Dissertation Director :

Vitaly Podzorov

In the first part of the thesis, studies of the charge carrier transport in organic semiconductors performed using organic field-effect transistors (OFETs) with polymeric gate dielectric (parylene) are presented. By combining OFET and ultraviolet photoelectron spectroscopy (UPS) studies, the effect of bias-stress instability at the semiconductor/insulator interface have been investigated and understood. The effect is understood in terms of the transfer of holes from an accumulation channel of the semiconductor to localized states of the insulator that depends on energetic overlap between HOMO band tails of the semiconductor and the insulator.

Second, surface functionalization of various materials such as organic single crystals, conjugated semiconductor polymers, graphene and carbon nanotubes (CNTs) with Self-Assembled Monolayers (SAMs) is described. In most cases, an enhanced surface conductivity is observed as a result of SAM treatment. Especially, fluorinated alkyl-silane (FTS) SAM induces the highest density of *p*-type charge carriers (in excess of an order of 10^{13} cm^{-2}), which leads to a strong surface hole-doping of these materials. In this thesis, (1) the mechanism of SAM nucleation, growth process and doping effect at the surface of

organic single crystals and graphene is revealed. SAM nucleation occurs predominantly at molecular step edges or defect sites present at the surface and a consecutive lateral growth proceeds by cross-linking between SAM molecules. The strong hole-doping is explained by an interfacial charge transfer that during SAM formation. In addition, conductive atomic force microscopy (C-AFM) confirms that conducting paths along the step edges are formed by FTS nucleation at the early stage of FTS growth on rubrene. (2) it is reported that conductivity of solution-deposited thin film of conjugated polymers increases by up to six orders of magnitude, reaching $(1.1 \pm 0.1) \times 10^3 \text{ Scm}^{-1}$ for poly(2,5-bis(3-tetradecylthiophen-2-yl)thieno[3,2-b]thiophene) and $30 \pm 20 \text{ Scm}^{-1}$ for poly(3-hexyl)thiophene upon bulk doping with FTS. Interestingly, SAM-doped polythiophene exhibits an intrinsic sensing effect: drastic and reversible change of the conductivity in response to polar molecules. (3) FTS growth is also performed on other carbon-based materials such as graphite, graphene and CNTs, which resulted in a strong hole-doping. Hall-effect and field-effect confirm that the order of 10^{13} cm^{-2} and 10^{14} cm^{-2} holes are induced on graphene layer and CNT sheets by FTS growth, respectively.

Acknowledgements

My Ph.D. period at Rutgers was pretty eventful years of my life. I had a challenging moment to change my research field and a tough time to adapt myself quickly to new circumstances. It is great pleasure to take the opportunity to thank people who have helped me make progress.

I owe my deepest gratitude to my advisor, Professor Vitaly Podzorov, whose guidance always kept me focused on my research. I also appreciate Professor Sang-Wook Cheong, Michael Gershenson, Eric Garfunkel, Leonard C. Feldman and Robert A. Bartynski for their kind advice. I am sincerely thankful to my Ph.D. committee members: Professor Paul Leath, Haruo Kojima, Eva Halkiadakis and Ahmad Safari for following my work during my research and valuable advice.

I have met lots of great colleagues whom I have worked with and interacted with during my Ph.D. I give my special thanks to my lab members: Dr. Yaunzhen Chen, Dr. Hikmat Najafov, Dr. Heetaek Yi and Danni Fu and Kris Czelen for their warm support and help. I am also thankful to Senia Coh, Dr. Hangdong Lee, Dr. Eric Bersch, Qibin Zhou, Dan Mastrogiovanni, Dr. Alan Wan, Dr. Sylvie Rangan, John Kim, Dr. Ivan Skachko, Dr. Matthew Bell, Joshua Paramanandam, Dr. Seungchul Chae, Dr. Youngjae Choi, Dr. Nara Lee and Dr. Yoonseok Oh for their deep friendship and care.

None of this would have been possible without my beloved family. I would like to express my heartfelt gratitude to my parents, Kwangok Lee and Soonjung Ryu, and my sisters, Dalim Lee, Sooyang Lee for their love and faith in me. I also gratefully acknowledge my parents-in-law and brothers-in-law for their love and continuous support.

My last acknowledgement goes to my wife, Sung Un Kim, for her constant support and encouragement. She has been with me at every moment during my studies, and I am so pleased that I can share my accomplishments with her.

TABLE OF CONTENTS

Abstract of the Dissertation.....	ii
Acknowledgements.....	iv
Table of Contents.....	vi
I. Introduction.....	1
II. Sample Preparation and Device Fabrication.....	3
1. Organic Single Crystals Growth.....	4
2. Deposition of Thin Films of Conjugated Polymers.....	6
3. Self-Assembled Monolayers (SAMs) Deposition.....	7
4. Parylene Insulating Polymer Deposition.....	9
III. Measurements, Data Analyses and Results.....	12
1. Organic Field-effect Transistors (OFETs).....	13
1.1. Organic Field-effect Transistors (OFETs).....	13
1.1.1. Review of OFETs.....	14
1.1.2. OFETs with Parylene Gate Dielectric.....	21
1.1.3. Air-gap PDMS Stamp OFETs.....	23
1.2. Bias-stress Instability in Single crystal OFETs.....	25
2. Functionalization of Organic Semiconductor and Other Carbon-based Materials by Self-Assembled Monolayers (SAMs).....	37
2.1. Growth of Alkyl-silane SAMs on Organic Single Crystals.....	37
2.1.1. Mechanism of SAM Nucleation and Growth Process on Rubrene Organic Single Crystal.....	37
2.1.2. Conductive AFM (C-AFM) Measurements for	

Step-decorated Rubrene by SAMs.....	43
2.1.3. Kelvin Probe Force Microscope (KFM) Investigation for Partially Coated Rubrene by SAMs.....	47
2.1.4. Anisotropy of Charge Transport in Rubrene with SAM-decorated Molecular Steps.....	49
2.2. Growth of Alkyl-silane SAMs on Conjugated Polymers.....	54
2.2.1. Electrical Modification of Conjugated Polymers by FTS SAM Doping.....	54
2.2.2. Optical Modification of P3HT and PBTTT Doped by FTS SAM.....	58
2.2.3. AFM and SEM Investigation into SAM Growth in Polythiophene Films.....	62
2.2.4. Sensing and Dedoping Effects of FTS SAM-doped Polythiophene Films.....	64
2.3. Growth of Alkyl-silane SAMs on Graphite and Graphene.....	68
2.3.1. Electrical Modification of Graphite by the Growth of FTS SAM.....	69
2.3.2. AFM and SEM Investigation for SAM Growth on Graphite.....	72
2.3.3. XPS Investigation on SAM Grown Surface of Graphite.....	74
2.3.4. Hall-effect Measurements on SAM Grown Graphite.....	76
2.3.5. FTS SAM Growth on Graphene.....	79
2.4. Growth of Alkyl-silane SAMs on Carbon Nanotubes (CNTs).....	82

2.4.1. CNTs Field-effect Transistor with Parylene Gate	
Dielectric.....	83
2.4.2. Electrical Modification of CNTs by FTS SAM Growth.....	87
IV. Conclusion.....	90
References.....	94
Appendix I: Nanoscale Conducting Channels at the Surface of Organic Semiconductors Formed by Decoration of Molecular Steps with Self-Assembled Molecules (<i>Adv. Funct. Mater.</i> ,2009).....	100
Appendix II: Modification of Electronic Properties of Graphene with Self-Assembled Monolayers (<i>Nano Letters</i> , 2010).....	105
Appendix III: Origin of Bias Stress Instability in Single-crystal Organic Field-effect Transistors (<i>Phys. Rev. B</i> , 2010).....	111
Appendix IV: Doping of Conjugated Polythiophene with Alkyl Silane (<i>Adv. Funct.</i> <i>Mater.</i> ,2009).....	115
Curriculum Vitae.....	121

Chapter I

Introduction

Organic Field-Effect Transistor (OFET) is a powerful tool to study charge transport in organic semiconductors by means of injecting charge carriers electrostatically by application of a gate electric field. High-performance OFETs with *parylene* or *air-gap* gate dielectrics were used to study the bias-stress instability in organic field-effect transistors¹.

Self-Assembled Monolayers (SAMs) are ultrathin molecular films spontaneously formed at surfaces or interfaces through chemical or physical interactions between molecules and a substrate's surface. For the past few decades, SAMs on metal, oxide or semiconductor surfaces have been studied to significant extent, and now SAMs are widely used in a variety of ways for modification of work function of metals, passivating the surface of oxides, forming electrically insulating film and changing the wettability of substrate surfaces²⁻¹². Recently, it has been demonstrated that organosilane SAMs can grow at the surface of organic semiconductor crystals¹³, carbon-based materials^{14,15} (graphene and carbon nanotubes) and conjugated organic semiconductor polymer films¹⁶. As a result, electronic or local optical properties of these materials are drastically modified at the interface with SAMs. In this thesis, the recent achievements in functionalization of aforementioned materials by the deposition of fluorinated or non-fluorinated alkylsilane SAMs are reported; investigation of the mechanism of SAM nucleation and growth is also described¹⁷.

Chapter II

Sample Preparation and Device Fabrication

1. Organic Single Crystal Growth

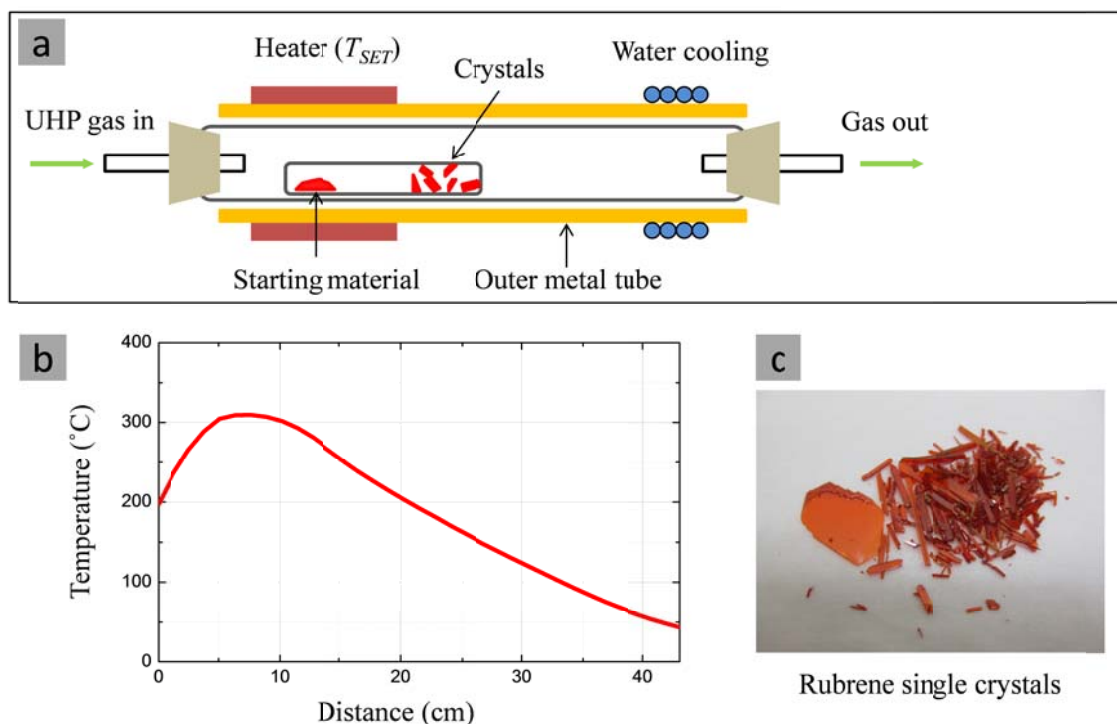


Figure 1. (a) Schematic diagram of organic single crystal growth furnace (physical vapor transport method); (b) actual temperature gradient profile along the axis of quartz tubes inside at $T_{SET} = 320^{\circ}\text{C}$; (c) rubrene crystals produced from the single growth operation.

High quality organic single crystals can be grown by utilizing *Physical Vapor Transport* (PVT) technique. In PVT method, organic molecules sublimed at the source or loading zone are transported by flowing gas and subsequently condensed as solid crystals at the growth region^{18,19}. Depending on the type of material, a growth furnace can be arranged vertically or horizontally. Figure 1(a) shows a horizontal furnace used to grow

freestanding organic single crystals such as rubrene, tetracene, TCNQ (Tetracyanoquinodimethane), etc. The growth system consists of a quartz tube enclosed in an outer metal tube with an external heater and cooler. A high thermal conductivity of the metal tube creates a smooth temperature gradient along the axis of the tube. Figure 1(b) represents an actual temperature profile inside the quartz tube along the growth furnace with two regions of stabilized temperatures: the highest T at the heater and the lowest T at the water cooler. Starting material is loaded at the high-temperature zone, where sublimation takes place at the temperature, T_{SET} , and evaporated molecules are carried by the gas stream into the region of lower temperature where crystallization occurs. Important parameters are a temperature gradient and the gas flow rate inside the growth tube. In our setup, the typical T_{SET} for rubrene, tetracene and TCNQ are around 320, 230, 220 °C, respectively. Ultrahigh purity argon, helium or hydrogen can be used as the transport gases, and the optimal flow rate is generally 50 ~ 100 cc/min. At such conditions, crystal growth usually takes approximately 24 ~ 70 hours for 100 ~ 300 mg of loaded material. The optimal setting parameters in different furnaces should be determined empirically depending on the design of a particular furnace. The lower temperature (just above the sublimation temperature of the material), heavy transporting gas such as argon and the low gas flow rate result in bulky, bar-shape crystals. On the other hand, the higher temperature, the high flow rate and lighter helium gas usually generate thin and wide crystals within reduced growth time. The crystals are usually growing at several centimeters away from the loading zone. Heavy impurities in the starting material are normally retained in the loading zone after the material is evaporated. Light impurities are deposited at the farther position away from the crystallization zone.

The amount of impurities can be further reduced by using previously grown crystals as the starting material. In organic single crystals, impurities are more decisive factor that can hinder charge transport, compared to structural defects such as dislocations and vacancies. Therefore, several cycles of regrowth (purification) improve the quality of the crystals dramatically, which results in an improved charge transport properties of organic crystals. Rubrene crystals grown by PVT method are shown in Figure 1(c).

2. Deposition of Thin Films of Conjugated Polymers

Regioregular poly(3-hexyl)thiophene (P3HT) from Alfa-Aesar and poly (2,5-bis(3-tetradecylthiophen-2-yl)thieno[3,2-b]thiophene) (PBTTT) from Merck were dissolved in chloroform and chlorobenzene, respectively. The concentration of P3HT in chloroform was 1.0 mg mL^{-1} (0.07 wt%) and that of PBTTT in chlorobenzene was 0.5 wt%. In the case of PBTTT solution, heat was applied through a water bath to dissolve it thoroughly. Before spin coating, the polymer solutions were filtered through a syringe filter with a $0.2 \text{ }\mu\text{m}$ pore size. Both solutions were spin-coated on a clean glass or Si/SiO₂ substrate at 2000 rpm for 40 seconds in ambient air. The spin-coated P3HT and PBTTT films were then annealed at 160 - 180 °C for 10 min in ultra-high purity (UHP) argon gas. The annealing process is performed by a gradual heating and cooling with elevating or decreasing the temperature as 10 - 20 °C steps for every 5 minutes. The resulting polymer film thickness was approximately 20 nm, as determined by AFM profile measurements.

3. Self-Assembled Monolayers (SAMs) Deposition

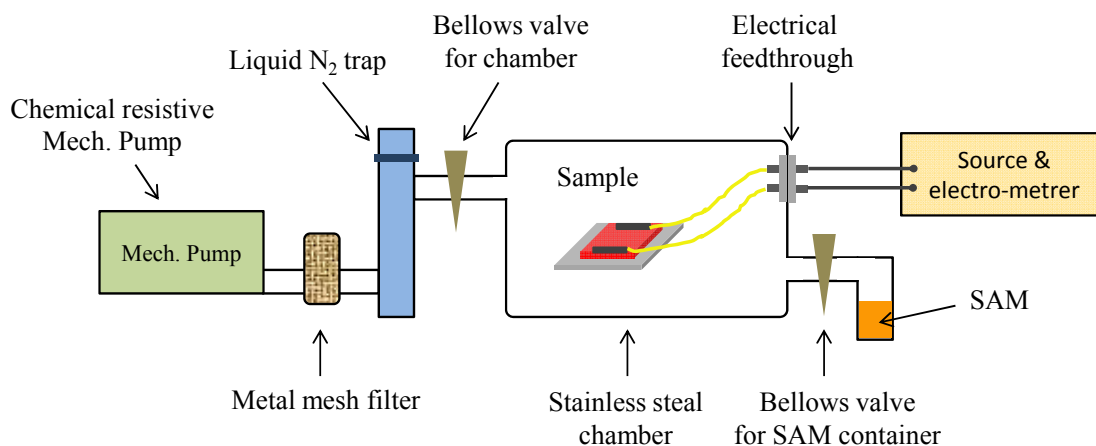


Figure 2. Schematic diagram of a setup for deposition of self-assembled monolayers (SAMs) from a vapor phase; SAM growth setup consists of a pumping system with filters, SAM growth chamber and instruments for electrical measurements.

Self-Assembled Monolayers (SAMs) are widely used in a variety of emerging applications for surface modification of metals and oxides²⁻¹². Among various SAM growth methods, a vapor phase deposition in a vacuum chamber can be used to produce smooth and uniform monolayers of SAM molecules at the substrate surface. As shown in Figure 2, SAM growth setup consists of a pumping system with filters, a SAM growth chamber and instruments for electrical measurements. Chemically resistive mechanical pump with Fomblin[®] (perfluorinated polyether) pumping oil is preferred to use for preventing a degradation of the mechanical pump from corrosive silane molecules. A metal mesh filter is also attached in a pumping line to catch SAM molecules before they

enter into the mechanical pump. A liquid nitrogen trap affixed to the deposition chamber plays two roles. First, it improves a vacuum pressure inside of the growth chamber. Second, it catches (traps) SAM molecules while opening the valve of SAM container during the pumping, which is a necessary step for removing trapped air in SAM container to improve vacuum. In addition, the metal mesh filter and the liquid nitrogen trap prevent pump oil residues from back-flowing into the growth chamber and contaminating the samples. The growth chamber consists of a satellite SAM container and electrical feed-through to *in-situ* monitor conductivity during the SAM growth. Bellows valves are preferred to use for retaining the vacuum inside the growth chamber and SAM container. All parts of the setup exposed to SAM molecules are made of stainless steel, since aluminum is subject to oxidation by byproducts of trichlorosilane chemistry. The procedure of SAM deposition is as follows.

- 1) Place sample with pre-deposited electrical leads in the SAM growth chamber and connect them to source- and electro-meter through an electrical feed-through. A liquid of SAM is filled in SAM container.
- 2) Pump the growth chamber by operating the mechanical pump for 30 minutes without filling the liquid nitrogen trap. SAM container should be blocked from pumping by closing the bellows valve during pumping. The vacuum pressure inside the chamber after 30 minute-pumping reaches approximately 10^{-2} Torr.
- 3) Fill the trap with liquid nitrogen while uninterrupted operation of the mechanical pump is on. This step will improve the vacuum further inside the chamber.

- 4) Gradually and thoroughly open the bellows valve for SAM container and wait one minute with pumping. This will remove trapped air inside the SAM container.
- 5) Close bellows valve for the growth chamber. SAM molecules will start growing at the substrate.

4. Parylene Insulating Polymer Deposition

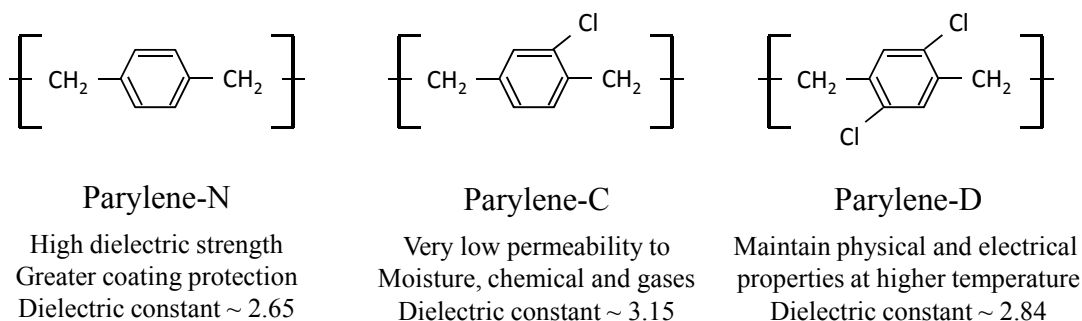


Figure 3. Three different types of parylene (non-conjugated organic polymers); Each type has different physical and electrical properties based on their slightly different molecular structure.

Parylene coating is a well-developed technology traditionally used in electronic packaging applications^{19,20}. A vapor phase deposition of parylene is conformal so that it covers features everywhere such as at sharp edges, defects or exposed internal surfaces with a relatively uniform thickness. The film of parylene provides an excellent dielectric strength. These factors make it a good gate dielectric material for organic field-effect

transistors (OFETs)²¹. Generally, three different types of parylene are used based on their different properties as shown in Figure 3.

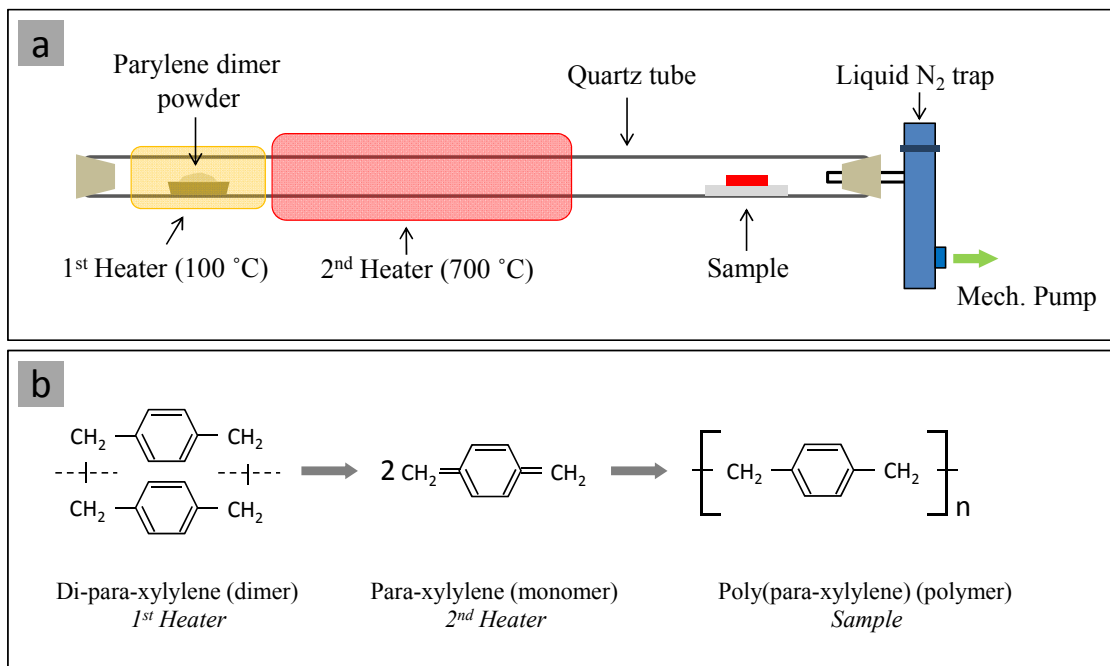


Figure 4. (a) Schematic diagram of two zone furnace of parylene deposition; (b) Reactions involved in the deposition process: sublimation of dimer at ~ 100 °C, splitting into monomers at ~ 700 °C and polymerization at room temperature

A sketch of a setup for parylene deposition is shown in Figure 4(a). Two heaters are assembled back to back along a long quartz tube. One end of the quartz tube is blocked by a silicon stopper and the other end is connected to a liquid nitrogen trap, which is then connected to a mechanical pump. Parylene starting materials are loaded in the first heating zone and the samples with prefabricated contacts and leads are placed in the position of the quartz tube near the liquid nitrogen trap as shown in Figure 4(a).

Pumping by the mechanical pump maintains a pressure inside the tube of approximately 10^{-2} Torr. Filling the trap with liquid nitrogen enhances the vacuum further as well as prevents a contamination of the mechanical pump by parylene. The starting material is parylene dimer sublimed at 100 °C. Therefore, the temperature in the first heating zone is maintained slightly above 100 °C. The evaporated parylene dimers pass through the second heating zone, a *pyrolysis* zone, maintained at 700 °C. At this temperature, each dimer splits into two monomers as described in Figure 4(b). These parylene monomers subsequently travel toward the section of ambient temperature, where the samples are placed, and polymerization occurs to form a transparent insulating film on the surface of the samples. 0.1 to 2 μm thickness of parylene coating can be grown in a single deposition run. During parylene growth, the thickness of the film is monitored by a color change of control samples placed next to the samples. Glass substrates or Si wafers are generally used as the control samples. As the thickness of parylene increases, the color of the control samples turn yellow, pink, violet and pistachio green in sequence (one cycle of deposition). During the film growth, this cycle repeats continuously. 1 μm thickness of parylene corresponds to approximately 6 cycles of color change. A general deposition time of 1 μm thickness of parylene is around 20 minutes. The capacitance of 1 μm parylene-*N* is approximately 2.1 nF/cm². Parylene coating has several advantages as the gate dielectric: 1) samples are maintained at room temperature throughout the entire process; 2) a high vacuum is not required; 3) the electrical and physical properties of parylene are very good: an electrical breakdown strength of up to 10 MV/cm, superior chemical stability, and high optical clarity.

Chapter III

Measurements, Data Analyses and Results

1. Organic Field-effect Transistors (OFETs)

1.1. Organic Field-effect Transistors (OFETs)

Transistor is one of the key elements of integrated circuits. Various types of inorganic transistors (mostly Si FETs) have been developed and the mechanisms of their operation have been rigorously studied and well understood²². However, in the case of *organic field-effect transistors* (OFETs), there are still many open questions related to the fundamental mechanisms of charge transport and physics of these devices. These challenges originate from inherent properties of organic materials: softness, fragileness and vulnerability to environment. Hence, special care and novel methods of device fabrications have been developed in recent decades^{23,24}. These OFETs are suitable not only for fundamental studies but also for developing novel applications²⁵⁻³¹. In this thesis, a few methods of fabrication of high-performance OFETs are described. They provide a tool for controllable modification of charge carrier density at organic surfaces without introducing chemical doping or disorder.

1.1.1. Review of Organic Field-effect Transistors (OFETs)

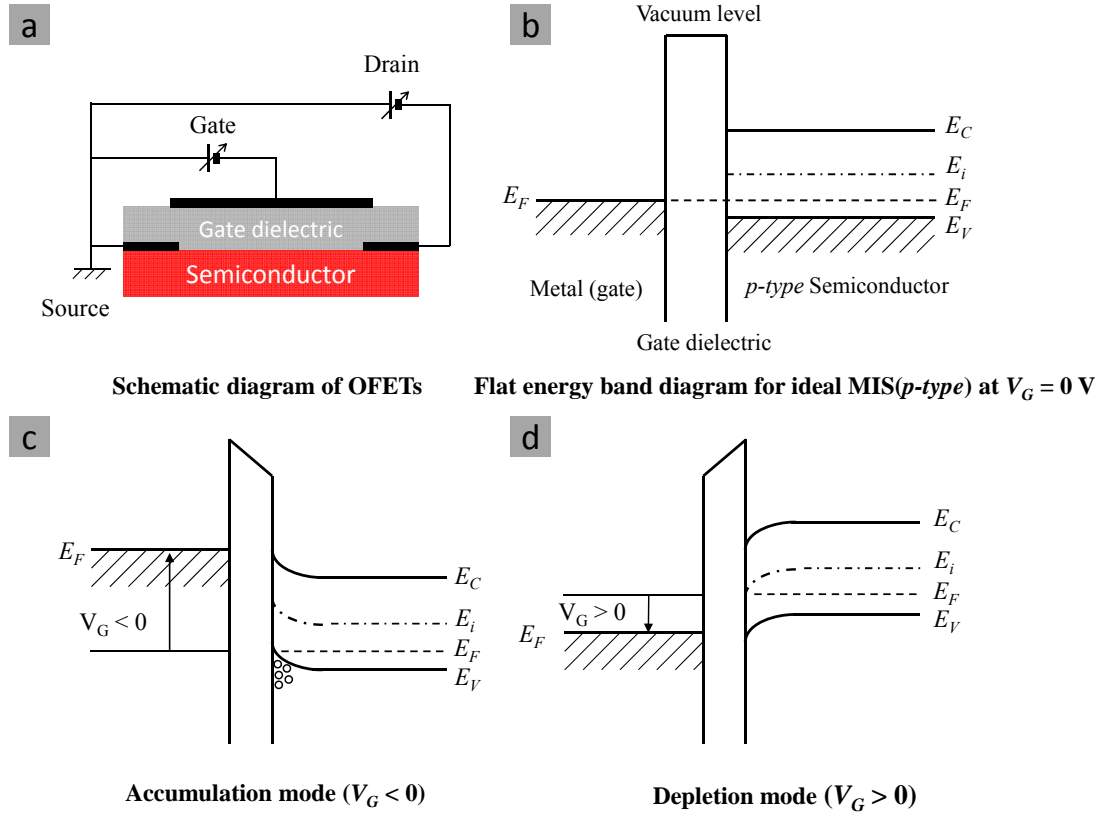


Figure 5. (a) Schematic diagram for OFET with bottom gate and bottom contacts geometry; (b) Flat energy band diagram for ideal Metal-Insulator-Semiconductor (p-type) junction without gate bias; (c), (d) Energy band alignments for negative gate bias in accumulation mode and positive bias in depletion mode of p-type semiconductor OFETs, respectively

OFETs can be understood based on conventional MOSFETs (Metal-Oxide-Semiconductor field-effect transistors); they are comprised of three terminals (source, drain and gate electrodes), a gate dielectric and a semiconductor. Source and drain

electrodes on the semiconductors inject and retrieve charge carriers when a source-drain voltage is applied. The gate electrode and semiconductor channel are separated by the gate dielectric and form a parallel Metal-Insulator-Semiconductor (MIS) capacitor. Figure 5(a) shows a schematic diagram of the OFET in bottom contact geometry, as an example. When the gate electrode is biased with positive or negative voltage, an electric field from the gate electrode penetrates the gate dielectric and causes bending of the energy bands of the semiconductor near the interface. Depending on the direction and magnitude the energy bands shift induced by the gate, three modes of operation can be realized at the surface of semiconductor; *Accumulation*, *Depletion* and *Inversion*. Unlike inorganic Si-MOSFETs utilizing *inversion*, OFETs are operating mostly in *accumulation* or *depletion* modes. Energy band diagrams for both accumulation and depletion modes are illustrated in Figure 5(c) and 5(d), respectively. In the case of *p*-type OFETs, when negative voltage is applied to the gate, the relative magnitude of intrinsic Fermi level and Fermi level, $E_i - E_F$, of semiconductor increases due to upward bending of the energy bands, which gives rise to an enhanced carrier concentration (accumulation of holes in semiconductor near the interface between the dielectric and semiconductor). On the other hand, a positive bias on the gate electrode bends the energy bands downward, and the reduction of $E_i - E_F$ causes a decrease of the carrier concentration (depletion of holes in the semiconductor). By altering the strength of the electric field (gate voltage), the induced carrier concentration is modulated, resulting in a variation of electrostatic doping level in the semiconductor in a controllable and reversible way. These are basic concepts of operation of OFETs. In actual devices, there are several parameters to affect OFET performance, *threshold voltage* (V_T), *on/off ratio*, etc. In many instances, the induced

charges initially populate localized states and no change in the channel conductance is observed until the gate voltage reaches the threshold voltage V_T . The value of the threshold depends upon factors such as the density of localized states in the semiconductor, traps at the interface between the gate dielectric and the semiconductor, and immobile charges or defects in the dielectric. Another parameter of OFET's performance, on/off ratio, is defined as the ratio of the current in the accumulation mode (with the high V_G) to that in the depletion mode. The higher on/off ratio states the better performance of OFETs.

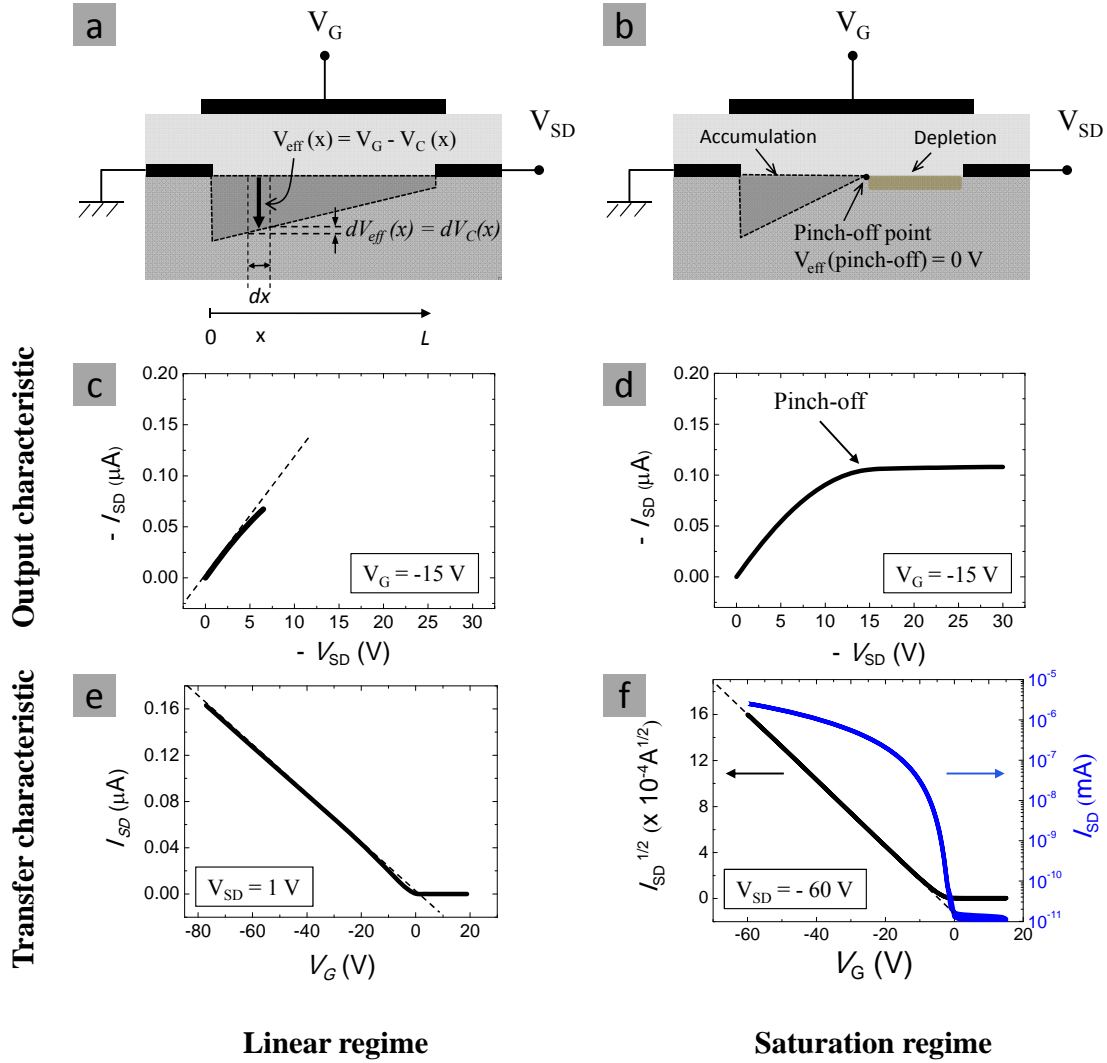


Figure 6. (a), (b) Schematic diagrams for linear and saturation regimes of OFETs: Pinch-off point in (b) appears when $V_D \approx V_G - V_T$ and moves further from the drain contact when V_D increases. (c), (d) output characteristics and (e), (f) transfer characteristics of OFETs in linear and saturation regimes, respectively.

There are two distinct properties that characterize OFETs; *transfer characteristic* and *output characteristic* curves based on operating variables. Figure 6 shows two different characteristic curves. Transfer characteristic curves are obtained by recording

the source-drain current at a fixed source-drain voltage while varying the gate voltage, whereas output characteristics are acquired by recording the source-drain current at a fixed gate voltage while varying the source-drain voltage. Current-voltage characteristics of OFETs can be understood in terms of Shockley's gradual channel model for the conducting channel. When the bias voltage is applied between source and drain electrodes, local channel potential $V_C(x)$ varies as a function of distance from the source electrode ($0 < V_C(x) < V_D$). In the presence of the gate bias, the effective local potential at a point in the channel can be expressed as $V_{eff}(x) = (V_G - V_T) - V_C(x)$ and the charge density induced by the gate at a given point in the channel depends upon this effective local channel potential. Hence, the equation of $\sigma_{2D}(x) = n_{2D}e\mu$ can be expressed as

$$\left(\frac{I_D}{dV_{eff}(x)} \right) \left(\frac{dx}{W} \right) = C_i V_{eff}(x) \mu = C_i [(V_G - V_T) - V_C(x)] \mu, \quad (1)$$

where x is a coordinate along the length of the channel, μ is a carrier mobility, C_i is a capacitance per unit area of the gate insulator, and W is the width of the channel.

Since $dV_{eff}(x) = dV_C(x)$, equation (1) can be rewritten as

$$I_D dx = W \mu C_i [(V_G - V_T) - V_C(x)] dV_C(x) \quad (2)$$

Upon integrating this equation over the length L of the channel, we obtain a final equation for current-voltage characteristics as equation (3).

$$I_D = \frac{W}{L} \mu C_i [(V_G - V_T) V_D - V_D^2 / 2] \quad (3)$$

Depending on the relative potential between the gate and the drain voltages, there are two regimes, *linear* and *saturation*, existing in OFET's operation. When the gate voltage is much larger than the drain voltage ($|V_D| \ll |V_G - V_T|$), the source-drain current, I_D , is

proportional to the drain voltage for the given gate voltage. This is called as a *linear* regime, in which the equation for I_D becomes:

$$I_{D_{lin}} = \frac{W}{L} \mu C_i (V_G - V_T) V_D \quad (4)$$

Note that in this regime, I_D is proportional to both V_G and V_D . Figure 6 shows the measurement of a real OFET (parylene/rubrene) device.

As expected from equation (4), in output characteristic curve of Figure 6(c), I_D increases linearly upon the increase of the drain voltage with a slope of $V_G - V_T$. In transfer characteristic curve of Figure 6(e), I_D also increases linearly when the gate voltage increases for the given drain voltage. Linear field-effect mobilities can be calculated from a channel conductance and transconductance relations based on output and transfer characteristic curves in linear regime, respectively. The channel conductance, g_d , and transconductance, g_m , are defined by

$$g_d = \left. \frac{\partial I_D}{\partial V_D} \right|_{V_G = \text{const}} = \frac{W}{L} \mu C_i (V_G - V_T) \quad (5)$$

$$g_m = \left. \frac{\partial I_D}{\partial V_G} \right|_{V_D = \text{const}} = \frac{W}{L} \mu C_i V_D \quad (6)$$

As $|V_D|$ increases and approaches $|V_G - V_T|$ at the higher drain bias, the electric potential difference between the gate and the drain diminishes to be zero. Hence, the density of charge carrier near the drain electrode becomes zero. This is called a “pinch-off point” indicated in Figure 6(b). When $|V_D|$ becomes higher than $|V_G - V_T|$ upon further increase of $|V_D|$, the pinch-off point shifts toward the source contact, which results in a shorter charge accumulation region and a more extended depletion region as shown in Figure

6(b). Once pinch-off sets in, I_D saturates and remains constant at a further increase of V_D . This is shown in Figure 6(d) (the arrow points to the onset of saturation in I_D at $V_D = -15$ V). It is because that the reduction in the density of induced charge carriers due to shortened accumulation region is exactly compensated by strengthening of a longitudinal electric field owing to the increase of the drain voltage. This is a *saturation* regime. Carrier injection from pinch-off point into depletion region near the drain is very similar to that of electron injection from a forward biased emitter-base junction to the reversed biased depletion region of a p-n-p transistor.

In the saturation regime ($|V_D| \gg |V_G - V_T|$) of OFETs, the drain current is attained by equation (3) with $V_D = V_G - V_T$,

$$I_{D_{sat}} = \frac{W}{L} \mu C_i \left[\frac{(V_G - V_T)^2}{2} \right] \quad (7)$$

Note that in this regime, I_D is proportional to square of V_G (as long as $|V_D| > |V_G - V_T|$).

Hence, the field-effect mobility in the saturation regime can be extracted from the slope of $\sqrt{I_D}$ vs $V_G - V_T$ curve. Such curve is shown in Figure 6(f). Transconductance in

saturation regime is $g_m = \frac{W}{L} \mu C_i (V_G - V_T)$, while channel conductance, g_d , is zero. The

mobility in the saturation regime can be different from that in the linear regime, because the distribution of carrier density along the channel is highly nonuniform on the channel in the saturation regime compared to linear regime Figure 6(b).

1.1.2. OFETs with Parylene Gate Dielectric

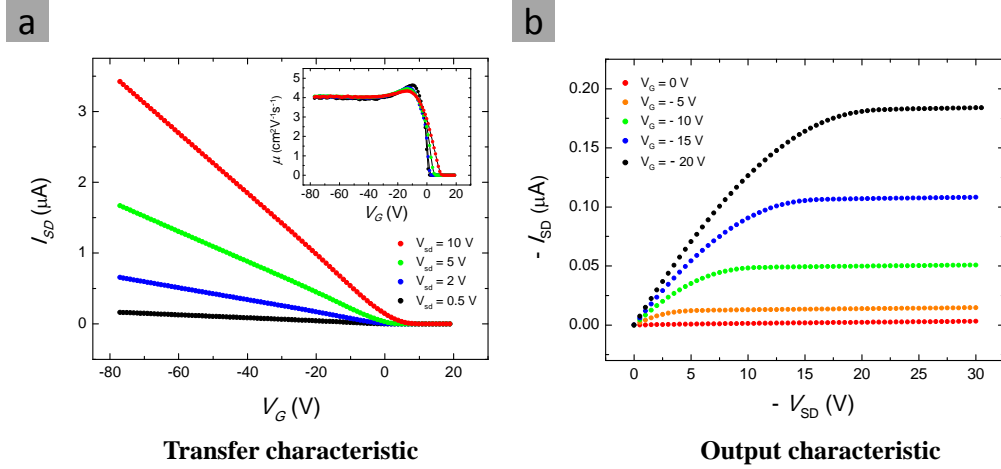


Figure 7. (a), (b) transfer and output characteristics of rubrene OFET with parylene gate dielectric; Inset of Figure 3 (a) shows the mobility curves extracted from transconductance equation (6) based on transfer characteristic curves with varying V_{SD} . The calculated linear mobility, μ_{lin} , is $4 \text{ cm}^2 \text{V}^{-1} \text{s}^{-1}$ in this device. Clear ‘pinch-off’ points and saturation are observed in output characteristic curves in (b).

Conventional inorganic or organic transistors are generally fabricated using silicon oxide (SiO_2) as a gate insulator. Well-developed growth method and a highly clean Si/ SiO_2 interface make SiO_2 the best choice of the gate dielectric²². However, there are some drawbacks of SiO_2 such as a high dielectric constant and random local potential of SiO_2 that affect the charge transport in active semiconductor channels directly^{32,33}. In addition, SiO_2 is not amendable to flexible applications, printing or solution processing. As substitutes for silicon oxide or high- k oxide dielectrics, various insulating polymers

have been used as the gate dielectrics in OFETs. As an example, *parylene*, a polymeric film, has been proven to be a good gate insulator with a high performance²¹. Parylene is a non-conjugated organic polymer and it can be deposited from a vapor phase on the surface of organic crystals at room temperature. Conformal nature of parylene coating is important for fabrication of free-standing single crystal OFETs²¹. In comparison with laminated devices on oxide dielectric, this has several advantages such as reduction of substrate-related strain and defect-free interface between semiconductor and dielectric. Additionally, optical transparency of the film enables us to perform optical measurements of OFET through the gate dielectric and a semi-transparent gate metal^{34,35}. Figure 7(a) and (b) show transfer and output characteristics of a free-standing rubrene OFET with parylene gate dielectric. It has been fabricated in bottom gate and bottom contacts geometry. The source and drain electrodes were deposited by application of colloidal graphite paint resulting in a low contact resistance. Parylene insulator has been deposited as described in the previous chapter. Capacitance of 1 μm -thick parylene-*N* film, C_i , is approximately 2.1 nFcm^{-2} . 1 μm -thick parylene layer can withstand more than 100 V. Both transfer and output characteristics represent a text-book FET behavior. This is only possible when the contact resistance is very low and the interface between semiconductor and the gate dielectric is very clean and defect-free. Drain current increases linearly upon raising the gate voltage in linear regime as shown Figure 7(a). Based on the transfer characteristics, the linear field-effect mobility is extracted using transconductance equation (6). The plateaus shown in the inset of Figure 7(a) are indicative of the linear field-effect conductivity when the gate voltage is much higher than the drain voltage (linear regime). The calculated mobility is $4 \text{ cm}^2\text{V}^{-1}\text{s}^{-1}$, which is consistent with the result

of Ref. 28. In output characteristics in Figure 7(b), the saturation of the drain currents have been observed very clearly above the pinch-off point and all pinch-off points match well the gate voltages applied. On/off ratio of a typical free standing rubrene OFETs with parylene gate dielectric is 10^5 .

1.1.3. Air-gap PDMS Stamp OFETs

Another type of OFET for use with organic single-crystals is the *PDMS air-gap OFET*. This technique has been developed by collaboration between Podzorov group at Rutgers and Rogers group in University of Illinois at Urbana Champaign and used to investigate the charge transport in organic single crystals before³⁶. A transistor circuitry is prefabricated by conventional microfabrication (lithography) methods on a flexible elastomeric (polydimethylsiloxane = PDMS) substrate and organic single crystal is subsequently laminated to it. This technique eliminates the needs for deposition of metal contacts and dielectrics directly onto organic crystals. The cross section view of this device is shown in Figure 8(a). Thin organic crystals can be laminated to the stamp with pre-deposited thin gold electrodes owing to van der Waals attraction force. PDMS Stamps are bendable and enable one to produce solid contacts for microscopically non-flat organic crystals. In these devices, conventional dielectrics are replaced by a micron-size gap between the gate electrode and the surface of the organic semiconductor. In other words, air or injected gases (or liquid) in a recessed structure can play a role of the gate dielectric in OFET devices.

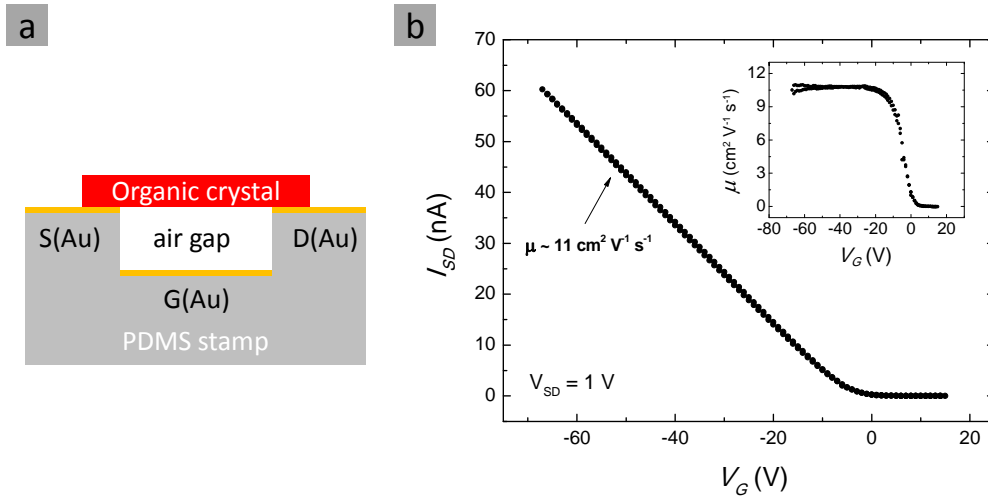


Figure 8. (a) Schematic side view of PDMS air-gap OFET; (b) Transfer characteristic curve for rubrene air-gap OFET: Negligible hysteresis and entirely linear curve is obtained. Inset of (b) shows the linear mobility calculated from transconductance equation (6).

Figure 8(b) shows transfer curve of rubrene PDMS air-gap stamp OFET and the inset shows the linear field-effect mobility calculated from equation (6). Highly linear transconductance, high field-effect mobility and almost negligible hysteresis for sweeping of the gate voltage have been achieved in PDMS air-gap stamp OFETs. Hence, the intrinsic charge transport properties of organic semiconductors can be studied more efficiently by replacing highly reactive oxides or insulating polymers with vacuum, inert gases or air as the gate dielectrics since SiO_2 or high- k dielectric affect the charge transport strongly at the interface of high purity organic single crystals.

1.2. Bias-stress Instability in Single Crystal OFETs

Bias-stress effect is a longstanding problem in organic and inorganic semiconductor field-effect transistors (FETs)³². Investigation of this phenomenon is not only of practical importance, but may also offer insights into the fundamentals of the energetic structure of semiconductor-dielectric interfaces³⁷. The effect presents itself as a continuous decrease of the current in the channel (or a shift of the threshold voltage) observed under accumulation conditions. Although the bias-stress effect has been studied in amorphous Si and lately in organic thin-film FETs, disorder present in these materials (e.g., ubiquitous grain boundaries³⁸) leads to a significant charge scattering, trapping and other non-intrinsic contributions to the transport properties. Several of the proposed mechanisms of the effect are indeed related to extrinsic phenomena, such as, e.g., *a*) trapping of holes in the semiconductor's channel, *b*) injection of electrons from the gate electrode into the dielectric, *c*) ionic conduction in the dielectric, and *d*) modification of contacts under the gate bias³². While all these effects are important for applications, the question still remains whether there is an intrinsic mechanism of the bias stress instability at well-defined semiconductor-dielectric interfaces without any involvement of ambient environmental factors or trapping in the semiconducting channel. Recently developed highly ordered single-crystal OFETs allow us to address this problem³⁹⁻⁴¹. The conclusions drawn from our experiment are not specific only to organic semiconductors and thus they can be applied to any band (semi)conducting material, such as for example Si, carbon nanotubes (CNT) or graphene, interfaced with an amorphous dielectric (SiO₂, high-*k* oxides or non-conjugated polymers).

In this study, the bias stress effect has been investigated in OFETs based on single crystals of several organic semiconductors: rubrene²⁸, tetracene⁴² and 6,13-bis(triisopropylsilylethynyl)pentacene (TIPS-pentacene)⁴³, that have been interfaced with a non-conjugated polymer, parylene, previously used as an insulator in high-performance OFETs³⁹. Investigations of this type of semiconductor-insulator interfaces are critically important, because practical organic electronic devices will ultimately rely on inexpensive plastic insulators rather than expensive oxides. Rubrene and tetracene single crystals have been grown by physical vapor transport described in the chapter of sample preparation. TIPS-pentacene single crystals have been prepared by crystallization from solution and annealed in a stream of forming gas (100 cc/min) at 120 °C for 4 hours before OFET fabrication. Fabrication of optimized devices is described in the previous chapter. Field-effect mobility, μ , was obtained from the linear transconductance curves, $I_{SD}(V_G)$ - the dependence of the source-drain current, I_{SD} , on the gate voltage, V_G , at a fixed source-drain voltage, V_{SD} . We have verified that contact resistance effects in our OFETs were negligible before and after gate stressing.

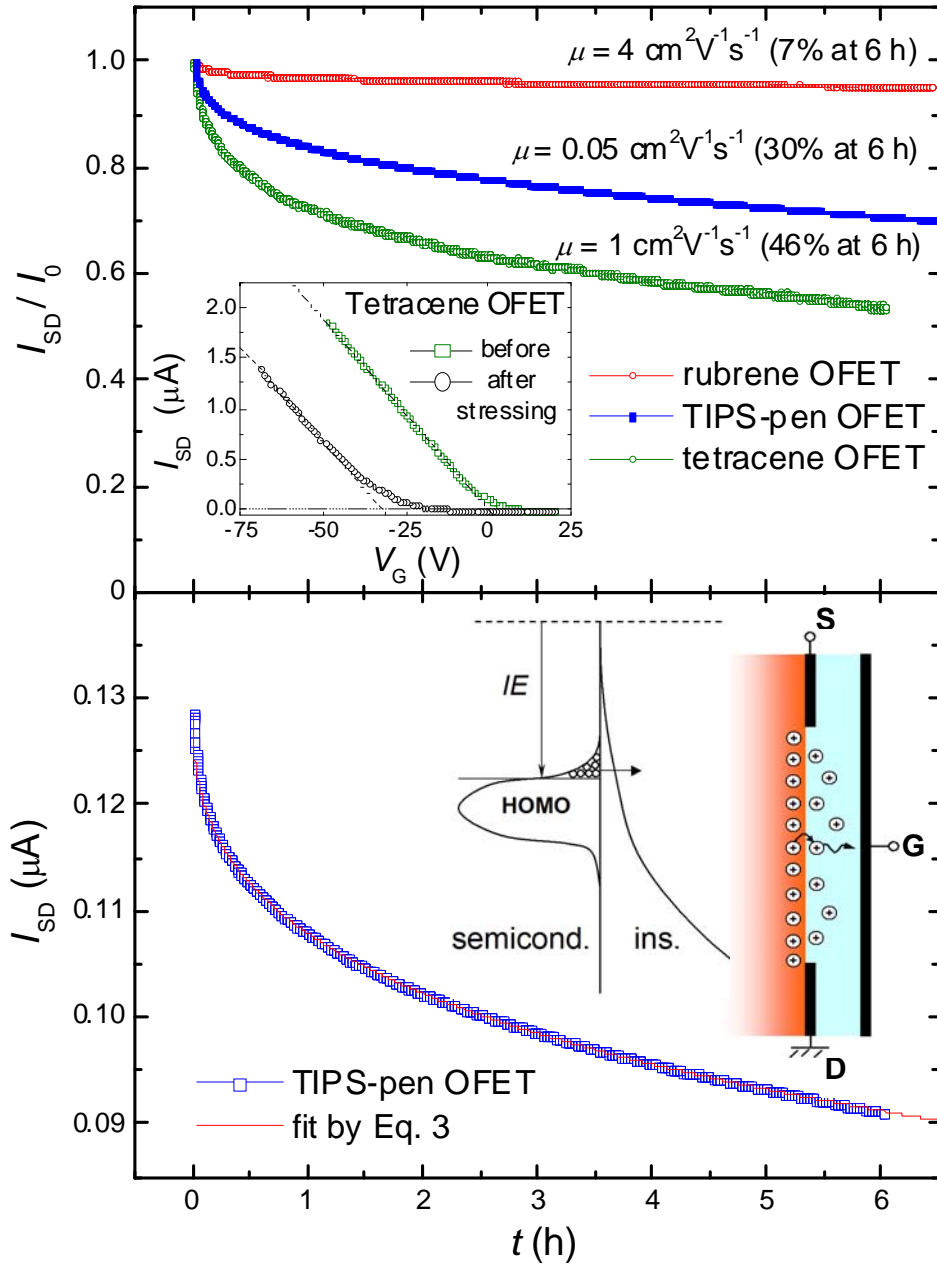


Figure 9. Top: Normalized bias stress curves, $I_{SD}(t)/I_0$, of several single-crystal OFETs ($V_G = -80 \text{ V}$, $V_{SD} = 25 \text{ V}$, $C_i = 2.35 \text{ nF/cm}^2$). The typical linear field-effect mobilities, μ , and the bias stress values at 6 h of continuous stressing are indicated for each system. The inset shows that the slope of $I_{SD}(V_G)$ does not change after stressing for 6 h. Bottom: The bias stress curve of a TIPS-pentacene OFET fitted with a stretched hyperbola (eq.

(10)). Similar fits are obtained for the other systems. The inset shows an energy model of the semiconductor-insulator interface: the hole transfer rate depends on the overlap between the semiconductor's HOMO and the exponential tail of localized states of the insulator. The cartoon schematically depicts the transfer and drift of holes in the insulator.

Figure 9 shows the typical bias stress characteristics of our OFETs, i.e. $I_{SD}(t)$ measured in the dark at fixed V_G and the magnitude of the bias stress as $\Delta I/I_0 = (I_0 - I(t))/I_0$ is defined, where I_0 is the initial source-drain current established right after the transistor is on. In rubrene OFETs, the dark bias stress effect is very small; the current decreases by only 5-7% after a continuous stressing for 6 hours at $V_G = -80V$, while in TIPS-pentacene and tetracene devices it is typically about 30% and 45%, respectively. Transconductance measurements before and after a prolonged stressing indicate that the slope of $I_{SD}(V_G)$ does not change in any of the studied systems, i.e. the bias stress effect is solely due to a shift of the threshold voltage without changes in μ (inset in the top panel of Figure 9), and hence measuring $I_{SD}(t)$ is analogous to measuring the threshold voltage shift. In addition, the preserved linear mobility in these 2-probe OFETs suggests that the contact resistance is not much affected by the stress²⁸. It is also interesting that the threshold voltage shift can be partially recovered by a prolonged application of a positive V_G . However, complete recovery in these p -type OFETs can not be achieved, because at $V_g > 0$ there is no accumulation channel, and hence the electric field at the interface is much weaker than the field at equivalent $V_g < 0$.

Two striking features of the bias stress instability can be seen in Figure 9. First, the rate and the magnitude of the effect strongly depend on the type of organic semiconductor, rather than on the typical charge carrier mobility of each system. For instance, although TIPS-pentacene OFETs have $\mu \sim 0.05 \pm 0.01 \text{ cm}^2\text{V}^{-1}\text{s}^{-1}$, which is not unusual for solution-grown single crystals with rough facets^{43,44}, the bias stress effect in these devices is typically smaller than that in tetracene OFETs with $\mu \approx 1 \text{ cm}^2\text{V}^{-1}\text{s}^{-1}$ (Figure 9). This trend has been verified in multiple devices measured in our laboratory over the course of several years. Second, all devices exhibit the same characteristic type of the bias stress curve independently of the overall magnitude of the effect: an initial fast decay of I_{SD} and a subsequent much slower relaxation that can continue for hours or days, as long as V_{G} is applied. In the prior studies, such distinct shape has been empirically fitted with a stretched exponent, adopted from amorphous Si transistors, where the bias stress is believed to be due to dispersive diffusion of hydrogen in α -Si^{32,45}. It is important to note that although a stretched exponential decay provides a satisfactory fit to most of the OFET data³², a detailed microscopic model explaining such behavior in organic semiconductors is lacking. It is especially difficult to justify such model in the case of highly ordered molecular crystals, where the charge transport can not be described as a dispersive hopping in exponentially distributed trap states, necessary to obtain a stretched exponential dependence³².

We argue that the leading mechanism of the bias stress instability in our OFETs is a ground-state *hole transfer* from the field-induced accumulation channel of the organic semiconductor to localized states of the adjacent insulator (sketch at Figure 9). The transferred holes, located between the accumulation channel and the gate, are screening

the gate electric field, so its effective value in the channel becomes: $E_G \equiv en_{\text{ch}}(t)/(\varepsilon\varepsilon_0) = V_G/d - en(t)/(\varepsilon\varepsilon_0)$, where e is the elementary charge, ε and ε_0 are the dielectric permittivities of the insulator and free space, respectively, $n(t)$ is an areal (i.e., 2D) density of the transferred holes, d is the insulator thickness, $n_{\text{ch}}(t)$ is the density of mobile holes in the OFET's channel that becomes smaller as the result of screening, leading to a decreasing source-drain current: $I_{\text{SD}}(t) = (W/L) \cdot V_{\text{SD}} \cdot \mu e \cdot n_{\text{ch}}(t)$. The density of transferred charge $n(t)$ is related to $n_{\text{ch}}(t)$ as: $n(t) + n_{\text{ch}}(t) = n_0$, where the constant $n_0 \equiv n_{\text{ch}}(t=0) = \varepsilon\varepsilon_0 V_G/(ed)$ is the initial density of holes in the channel. The charge transfer rate, dn/dt , should be proportional to the density of holes available in the accumulation channel, n_{ch} , and a 3D density of states, δ_0 , in the exponentially distributed tail states of the disordered insulator at an energy matching the semiconductor's HOMO edge, where holes are accumulated (Figure 9). The magnitude δ_0 depends on the relative position of ionization energies of the semiconductor and the insulator, as well as on the extent of the tail states of the latter. In addition, since the process of filling δ_0 states by interfacial charge transfer is fast, the rate of the bias stress effect will be mainly limited by the secondary process - a slow *diffusion* or *drift* of the transferred holes away from the interface (toward the gate), as the result of which some of the insulator's states near to the interface become empty and available again for further hole transfer. Therefore, dn/dt will be also proportional to the sum of diffusion and drift fluxes of holes in parylene, $j_{\text{diff}} \approx D_{\text{ins}} \cdot \delta_0 / \lambda_0$, and $j_{\text{drift}} = \delta_0 \cdot v_{\text{drift}} = \delta_0 \cdot \mu_{\text{ins}} \cdot E_G = \delta_0 \cdot \mu_{\text{ins}} \cdot en_{\text{ch}}/(\varepsilon\varepsilon_0)$, where D_{ins} is a diffusivity of holes in the insulator, λ_0 is a characteristic width of the spatial distribution of holes in the insulator near the interface, $v_{\text{drift}} \equiv \mu_{\text{ins}} \cdot E_G$ is a drift velocity of holes with hopping mobility μ_{ins} in the insulator near the interface. μ_{ins} in non-conjugated insulators is extremely small and to the

first approximation does not show a Poole-Frenkel dependence, because of *a*) relatively small E_G used in our study, and *b*) undoped, non-polar nature of parylene without spatial correlations of energetic disorder⁴⁶. Hence, the charge transfer rate can be expressed as $dn/dt \equiv -dn_{ch}/dt = \chi_0 \cdot n_{ch} \cdot (j_{diff} + j_{drift})$, or:

$$dn_{ch}/dt = -\chi_0 n_{ch} (D_{ins} \delta_0 / \lambda_0 + \delta_0 \mu_{ins} E_G), \quad (8)$$

Where χ_0 is a cross-section of the charge transfer process in cm^2 .

Dispersive transport in virtually all disordered systems with an exponential distribution of band tails universally exhibits a power-law time dependence of diffusivity and mobility, $D_{ins} = D_0 \cdot (t/\tau_{ins})^{\beta-1}$ and $\mu_{ins} = \mu_0 \cdot (t/\tau_{ins})^{\beta-1}$, where τ_{ins} is the characteristic trapping time in the insulator ($1/\tau_{ins}$ is the hopping rate) at the transport energy level (not to be confused with HOMO edge), and $\beta \equiv T/T_0 < 1$ is a dispersion exponent related to the characteristic width of the band tail of the insulator^{32,47}. Hence, we can rewrite (8) as:

$$dn_{ch}/dt = -\chi_0 \cdot (t/\tau_{ins})^{\beta-1} \cdot (D_0 (\delta_0 / \lambda_0) \cdot n_{ch} + \delta_0 \mu_0 e / (\epsilon \epsilon_0) \cdot n_{ch}^2) \quad (9)$$

Note that if the charge motion in the insulator is dominated by diffusion ($j_{diff} \gg j_{drift}$), the rate of the bias stress effect will be proportional to n_{ch} or V_G , and the solution of eq. (9) will be a stretched exponent, $n_{ch}(t) = n_0 \cdot \exp[-(t/\tau)^\beta]$, where τ is a renormalized V_G -independent time constant $\tau = \tau_{ins} \cdot [\lambda_0 \beta / (\chi_0 D_0 \delta_0 \tau_{ins})]^{1/\beta}$. However, if the process is dominated by drift ($j_{diff} \ll j_{drift}$), dn/dt will be proportional to n_{ch}^2 or V_G^2 , and the analytical solution of eq. (9) for the source-drain current $I_{SD} = (W/L) V_{SD} \mu e \cdot n_{ch}$ is a stretched hyperbola:

$$I_{SD}(t) = \frac{I_0}{1 + (t/\tau)^\beta}, \quad \tau = \tau_{ins} \cdot \left(\frac{\beta d}{V_G \chi_0 \mu_0 \delta_0 \tau_{ins}} \right)^{1/\beta} \quad (10)$$

where $I_0 \equiv I_{SD}(t = 0)$ is the initial current in the channel, and τ is a renormalized V_G -dependent time constant. In both cases, the time constant τ increases as $(1/\delta_0)^{1/\beta}$ for interfaces with a smaller energetic overlap δ_0 .

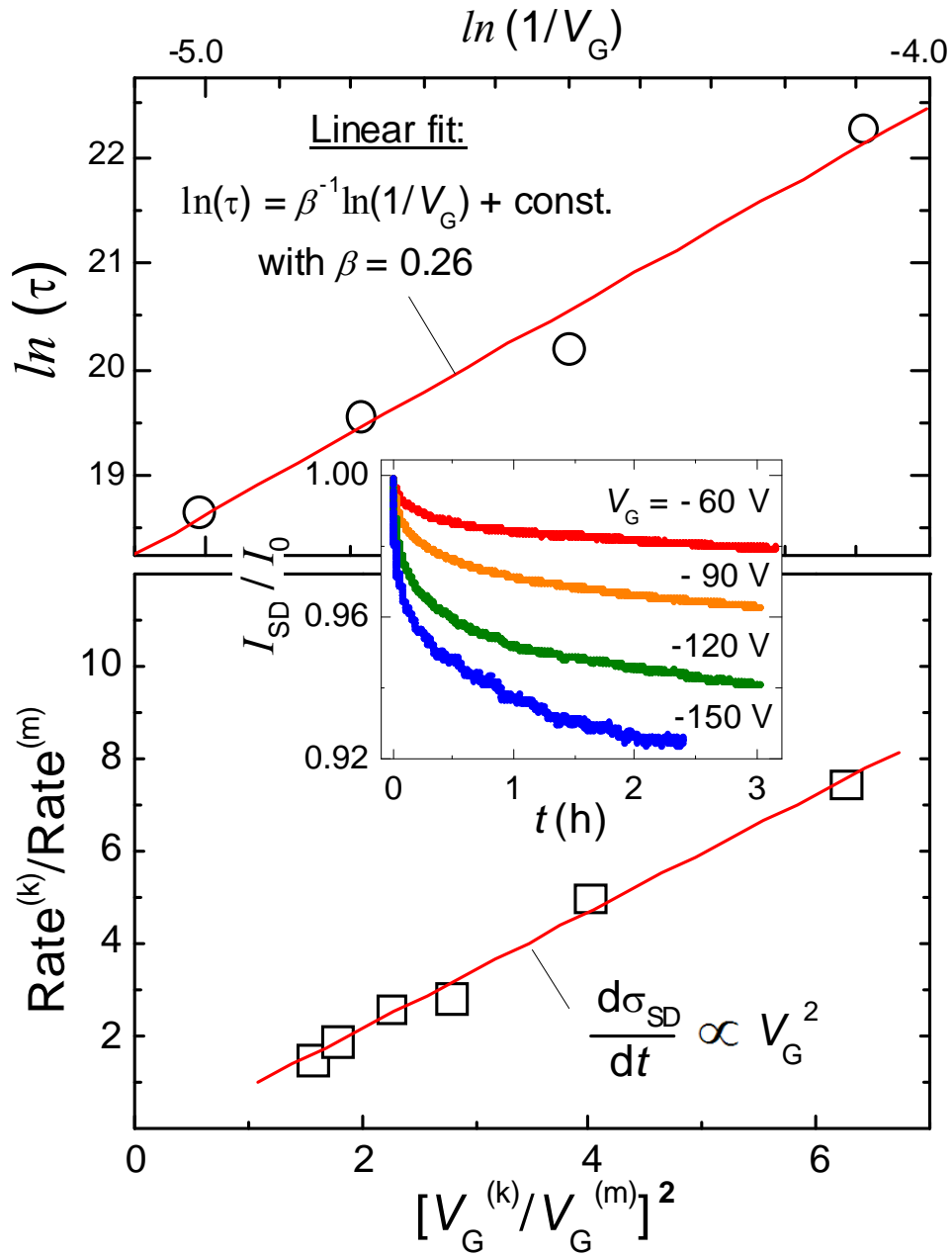


Figure 10. *Bias stress effect in rubrene OFETs measured at different V_G (inset). Top: V_G dependence of the time constant τ , obtained for the four curves by stretched hyperbola fits (eq. (10)). Bottom: Ratio of the bias stress rates measured at different V_G and plotted as a function of V_G ratios squared. Red line is a linear fit.*

In our experimental situation, the hole motion in the insulator is drift-limited. Indeed, we have estimated that the ratio $j_{\text{drift}}/j_{\text{diff}} = (\lambda_0 \mu_0 V_G)/(D_0 d) = (e V_G/k_B T) \cdot (\lambda_0/d) \sim 10\text{-}30 \gg 1$, with $D_0 = k_B T \mu_0/e$ (k_B is the Boltzmann constant), and $\lambda_0 \sim 3\text{-}10$ nm - a reasonable lower limit of the distance at which holes are injected into the parylene. Moreover, we have confirmed the drift-limited regime experimentally by measuring the actual dependence of the bias stress rate, dI_{SD}/dt , on V_G in a number of nominally identical rubrene transistors (Figure 10). The inset in Figure 10 shows that the bias stress effect is indeed greater at a higher V_G , and the rate follows a V_G^2 dependence (the lower panel), as expected from eq. (9) in this regime. In addition, fitting the four curves in the inset with a stretched hyperbola (eq. (10)) yields a V_G -dependent τ and a value of $\beta = 0.3 \pm 0.05$. According to eq. (10), τ should be proportional to $(1/V_G)^{1/\beta}$.

Plotting $\ln(\tau)$ vs. $\ln(1/V_G)$ for this set of devices indeed results in a linear dependence with a slope consistent with $\beta \sim 0.3$ (the upper panel of Figure 10).

A stretched hyperbola (eq. (10)) provides a perfect fit to all of the studied systems (for simplicity, the lower panel of Figure 9 shows only the fit for TIPS-pentacene OFET). It is worth noting that τ and β obtained by fitting these systems are consistent with the underlying physics of the effect. Indeed, τ decreases in the order: rubrene (49.5×10^6 s), TIPS-pentacene (0.177×10^6 s) and tetracene (0.031×10^6 s), consistent with the bias stress

rate increasing in this order and implying that δ_0 is also increasing in the same order (we confirm this trend below by UPS). However, the exponent β is found to be almost constant: $\beta = 0.37 \pm 0.05$.

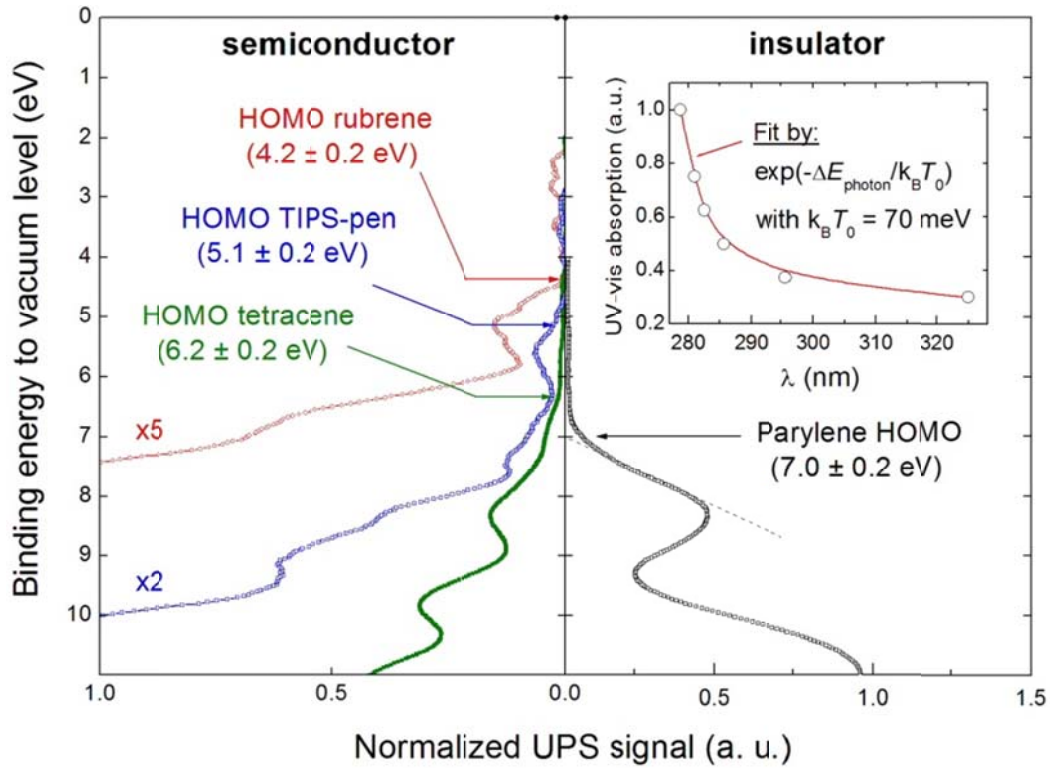


Figure 11. Left: UPS spectra of crystalline rubrene (red), TIPS-pentacene (blue) and tetracene (green). Photoemission onsets (i.e., HOMO edges or IEs) referenced to the vacuum level are shown with the arrows. Right: UPS spectrum of an ultrathin (10 ± 2 nm) parylene-N on gold. The inset is a UV-vis optical absorption spectrum of parylene-N, showing a ~ 1.5 eV-wide tail of states below the 280 nm absorption edge.

According to our model, organic transistors with a greater energetic overlap between HOMO and localized states of the insulator should exhibit a stronger bias stress effect (Figure 9). In order to test this idea, we have performed UPS studies of ionization energies (IE) of the organic crystals and the insulator used in this study (Figure 11) (details of UPS technique can be found elsewhere⁴⁸). IE refers to position of the HOMO edge with respect to the vacuum level (i.e., it is an energetic position of holes in the accumulation channel in *p*-type OFETs). The IEs of rubrene, TIPS-pentacene, tetracene and parylene are 4.2 ± 0.2 , 5.1 ± 0.2 , 6.2 ± 0.2 and 7.0 ± 0.2 eV, respectively. Despite a considerable difference between the HOMOs of the organic semiconductors and parylene, the exponential tail states of the latter (seen above 7 eV in Figure 11) allow for a small charge transfer. A better evidence of the extended in-gap tail states of parylene is provided by the UV-visible absorption of this material (inset in Figure 11). As expected, the absorption edge (280 nm) considerably tails into the band gap. Fitting this tail with an exponential distribution yields $k_B T_0 \approx 70$ meV, in a good agreement with a room-temperature value of $\beta = T/T_0 \sim 0.37$. The relative positions of the semiconductor's and the insulator's HOMOs determined from our UPS are consistent with the observed trend for the rate of the bias stress effect to increase for semiconductors with a “deeper” HOMO.

It is worth noting that vacuum-gap OFETs exhibit a negligible bias stress, provided that there are no polar molecules in the residual gas in the gap. However, these devices do show a bias stress effect of a different kind that occurs as a result of an introduction of polar molecules in a gaseous form in the gap (e.g., acetone or water

vapor), resulting in the effect proportional to the dipole moment of the molecules due to the gate-induced polarization of the vapor.

Most of the extrinsic factors contributing to bias stress can be ruled out in our devices. For example, charge trapping in the accumulation channel cannot be the primary cause, because there are examples of OFETs with a high trap density (low μ) that nevertheless show noticeably smaller bias stress effect than other devices with a much greater μ . The influence of water at the interface or in the dielectric can also be ruled out, because it would not result in a systematic dependence of the effect on the HOMO energy. In addition, *a)* we have tested that *in-situ* annealing of the samples at moderate temperatures in vacuum before parylene deposition does not influence the effect, and *b)* we have used macroscopic grain-boundary free organic crystals encapsulated in a non-hygroscopic parylene deposited in vacuum and capped with a 50 nm-thick Ag gate. Hence, post-fabrication water permeation would be highly unlikely. Finally, an injection of electrons from the metal gate into the insulator in our OFETs is excluded, because of the outstanding insulating properties of parylene revealed in I - V measurements of Ag/parylene/Ag sandwich structures, showing a typical insulating behavior with a very large resistivity, $\rho > 100 \text{ G}\Omega$ for up to $\pm 200 \text{ V}$.

2. Functionalization of Organic Semiconductor and Other Carbon-based Materials by Self-Assembled Monolayers (SAMs)

2.1. Growth of Alkyl-silane SAMs on Organic Single Crystals

2.1.1. Mechanism of SAM Nucleation and Growth Process on Rubrene Single Crystal

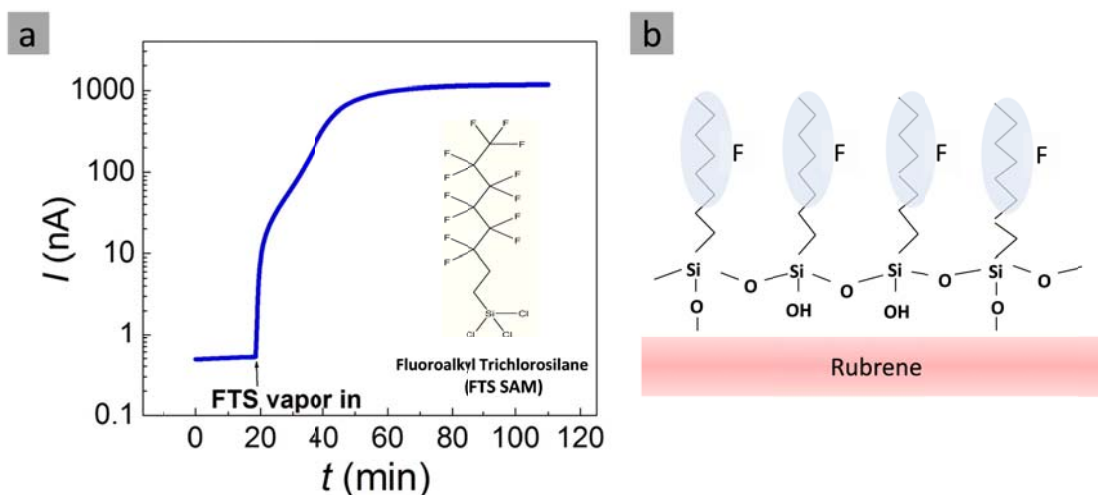


Figure 12. (a) Surface conductivity change during SAM growth on rubrene crystalline semiconductor. The inset shows the molecular structure of fluorinated SAM (FTS SAM) used in our experiments. (b) Schematic diagram of SAM formation on the surface of organic crystals.

To functionalize the surface of organic semiconductors, two different types of self-assembled monolayers (SAMs) are generally used. (tridecafluoro-1,1,2,2-tetrahydrooctyl)trichlorosilane (FTS) and n-octyltrichlorosilane (OTS) are SAM molecules which have commonly trichlorosilane head group and perfluorinated and non-fluorinated alkyl tails, respectively. The molecular structure of FTS SAM is drawn in the inset of Figure 12(a). These molecules are extensively used for passivation of the surface of inorganic oxides (e.g., SiO_2)⁴⁹. In the case of SiO_2 , the mechanism of SAM formation involves three basic steps⁵⁰: (1) hydrolysis, which converts trichlorosilane groups of SAM molecules, SiCl_3 , into silanol groups, $\text{Si}(\text{OH})_3$; (2) covalent bonding of hydrolyzed (fluoro)alkyl-silanes to OH-terminated SiO_2 surface as the result of which Si-O-Si bridges to the substrate are formed; and finally (3) in-plane polymerization of the SAM molecules through covalent bonding of free silanol groups of the adjacent FTS molecules. In this process, a fully cross-linked SAM layer which is covalently bonded to the substrate can be formed stably. This process requires: a) water in the vapor phase or water at the surface to promote hydrolysis of trichlorosilanes and b) availability of surface OH groups on SiO_2 for covalent anchoring of the SAM to the substrate. It is likely that similar requirements must be met for a sustainable growth of a stable SAM on organic surfaces. The surface defect sites especially containing OH-terminated groups play a role of anchoring of SAM molecules to the surface of organic crystals. The most probable schematic diagram of SAM formation on organic single crystal is shown in Figure 12(b).

As a result of SAM growth at the *p*-type organic semiconductor surface, the surface conductivity rapidly increases by several orders of magnitude; the drain current is

monitored at fixed drain voltage during FTS SAM growth (Figure 12(a)). The surface conductivity, σ , of rubrene crystals treated with FTS SAM approaches as high as 10^{-5} S per square, two orders of magnitude greater than the maximum conductivity typically achieved in organic field-effect transistors¹³. It has been suggested recently that SAM-induced conductivity is due to the unbounded free silanol group (Si-OH) available in hydrolyzed partially cross-linked 2D SAMs that result in the acidic protons at the SAM-organic interface and protonic doping of the surface¹⁶.

To begin with, the local nanoscale morphology of SAM nucleation and the early stage of growth process on organic crystals have been studied by atomic force microscope (AFM). It is discovered that SAM nucleation on the organic semiconductors predominantly occurs at molecular step edges on the surface.

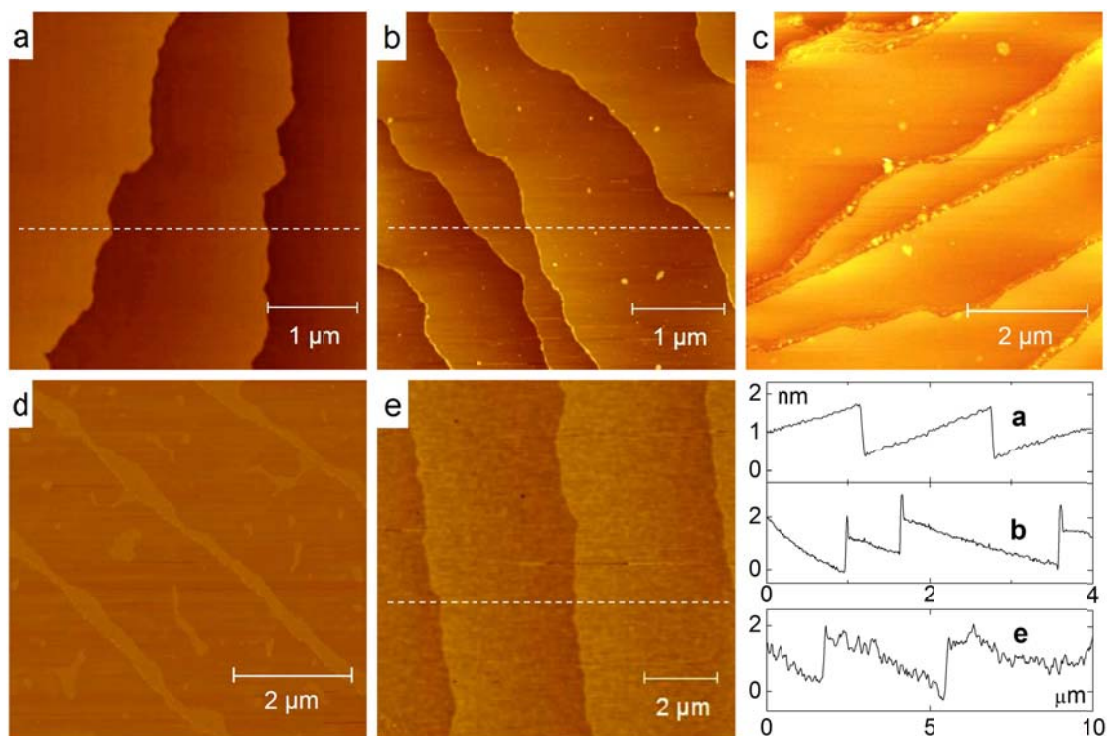


Figure 13. *AFM topography of molecular steps in rubrene decorated by FTS SAM (tapping mode): (a) pristine crystal; (b) crystal treated with FTS vapor for a very short time, $\Delta t = 2$ min; (c) $\Delta t \approx 5$ min; (d) $\Delta t \approx 10 - 15$ min; (e) fully coated rubrene crystal (treated for a few hours); the last panel shows AFM profiles taken along the dotted lines in (a), (b) and (e).*

Figure 13 shows AFM topographies of the surfaces of (a) pristine rubrene crystal, (b) - (d) rubrene crystals exposed to FTS vapor for short periods of time (2 - 10 min), and (e) a rubrene crystal that has been exposed to FTS for a few hours. The bottom right panel in Figure 13 shows AFM profiles taken along the dotted lines in Figure 13 (a), (b), and (e). The AFM images corresponding to the initial stages of FTS growth (b) - (d) show that the appearance of molecular steps has clearly changed compared to the pristine rubrene: they have gained contrast and became reminiscent of “rivers” of finite width. A comparison of AFM profiles (traces (a) and (b)) shows the appearance of “spikes” at the step edges after a short FTS treatment, suggesting that the SAM starts growing at the steps. Detailed analysis of these spikes shows that their width is limited by the lateral resolution of our AFM defined by the tip radius (~ 20 nm), which indicates that the actual width of the SAM-decorated region is $\ll 20$ nm. After longer treatment, the width of these rivers increases (Figure 13(d)), and after a very long treatment, the entire surface becomes coated with a continuous monolayer resulting in a fuzzy AFM image, where the noise is due to the interaction of AFM tip with a soft SAM surface (see Figure 13(e) and the corresponding trace (e)). It is interesting that the underlying molecular step structure of the crystal in this case can still be clearly seen under the completed SAM; this implies

that the layer is indeed a monolayer with a thickness that is not much greater than the height of molecular steps in rubrene (1.5 nm)⁵¹, as originally suggested¹³. These data show that SAM nucleation at the surface of pristine rubrene crystals first occurs at molecular steps. It is worth mentioning that nucleation of SAMs in the middle of terraces can also be observed either after longer FTS exposure, or as the result of crystals having a higher density of surface defects. This can be seen as bright “dots” at the terraces in Figure 13(b) and (c) and “islands” in Figure 13(d).

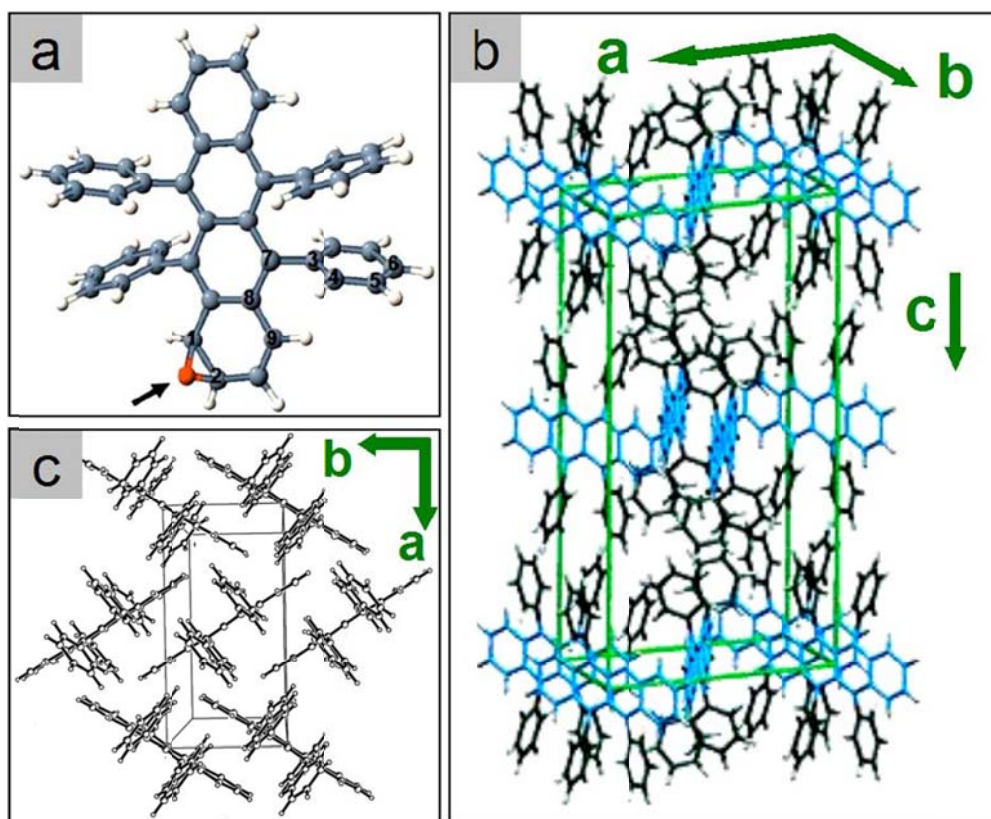


Figure 14. Calculations show that the most easily formed oxidative state of rubrene molecule is an epoxy group on the end ring of the rubrene core (a). According to the bulk crystal structure of rubrene (b) and the slipped-stack packing motif of (a,b) crystal facets

(c), the end benzene rings of rubrene cores are exposed to the ambient air along the molecular steps at this largest natural facet.

The data collected in this work imply that a) molecular steps of pristine p-type organic crystals comprise species responsible for binding FTS SAMs to these materials and b) these species are likely oxygen- containing molecules of the semiconductor (here, a form of rubrene oxide, such as an epoxy or hydroxy group), that preferentially forms along the molecular steps, when freshly grown crystals are exposed to ambient air. This observations are supported by the recent theoretical work by Tsetseris and Pantelides, which shows that formation of oxygen-related species, including epoxy and hydroxy groups, as well as the physisorption of water at the surface of molecular crystals is not only possible, but energetically favorable^{52,53}. Specifically, the effect of molecular step decoration is consistent with theoretical calculations suggesting that the most energetically favorable oxidative state of rubrene is an epoxy group located at the end benzene ring of the rubrene core (Figure 14(a))^{52,53}. Indeed, according to the crystal structure of rubrene shown in Figure 14(b) and (c), this molecular site is exposed to the environment at a molecular step on the *(a,b)* facet, and, therefore, the step edges are likely to be oxidized much more easily. The study by Tsetseris and Pantelides also shows that water can be physisorbed in a stable form at the surface of rubrene⁵³. This helps explain that the observed lateral growth of SAM after nucleation proceeds through hydrolysis and in-plane polymerization of the silanol groups of the adjacent SAM molecules.

2.1.2. Conductive AFM (C-AFM) Measurements for Step-decorated Rubrene by SAMs

So far, it has been observed that under certain conditions, SAM molecules preferentially bind to molecular steps at the surface of crystalline organic semiconductors, inducing a strong local doping effect. This creates macroscopically long conducting paths of nanoscale width (a single crystalline analogue of organic nanowires) that can span distances of up to 1 cm between electrical contacts. To confirm the conducting quasi 1-D paths, conducting-tip AFM (C-AFM) measurements were performed.

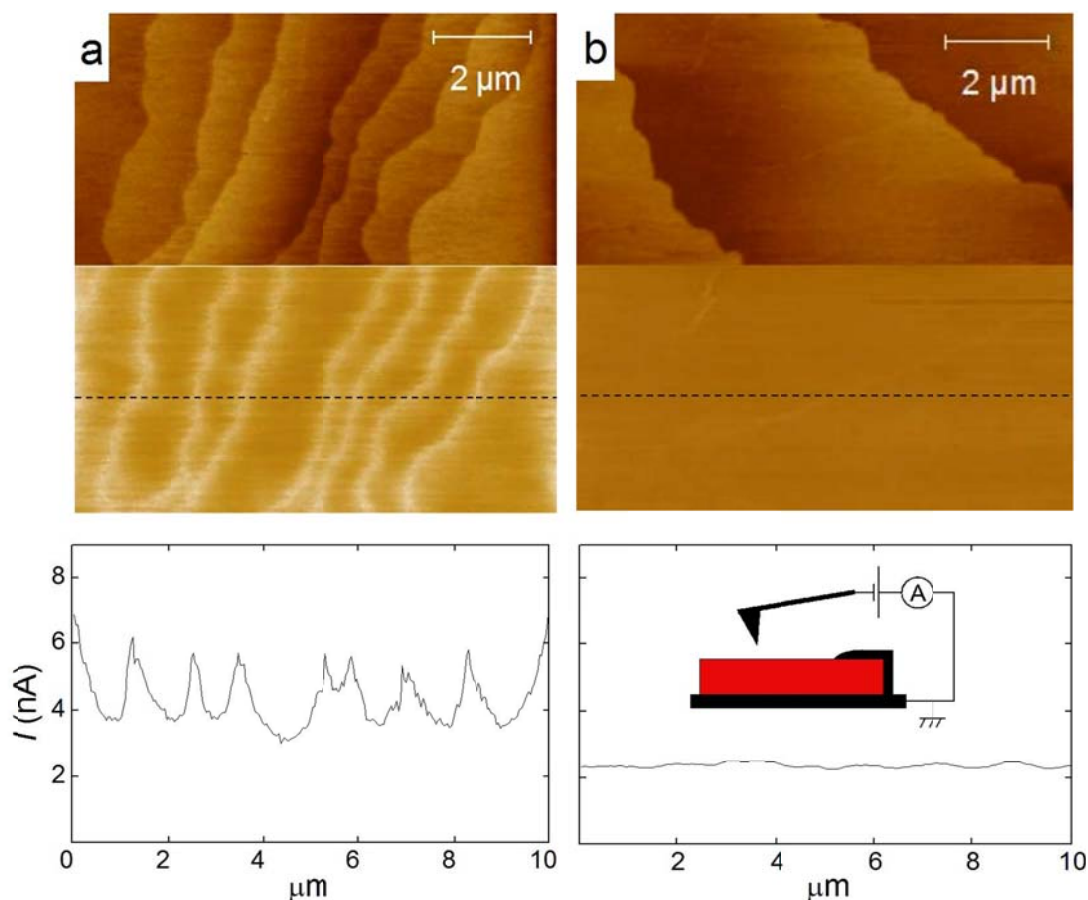


Figure 15. *C-AFM measurements of molecular steps in rubrene (upper: contact-mode topography; lower: local conductivity maps where lighter color corresponding to higher tip-sample current): (a) crystal with molecular steps decorated by SAM using a very short FTS treatment (~ 2 min); (b) pristine untreated crystal. The lower panels show current profiles measured with C-AFM along the dotted line in (a) and (b). These data show that SAM-decorated steps are conducting, while the steps of pristine crystals are not.*

The C-AFM measurements of the samples with SAM-decorated steps reveal that these steps are conducting. In C-AFM technique, a fixed DC voltage is applied to a conducting AFM tip with respect to the grounded sample, and DC tip-sample current is measured while scanning the surface in contact mode (see inset in Figure 15(b)). Lighter color in C-AFM images corresponds to the higher tip-sample current. Figure 15(a) shows contact-mode topography (upper panel) and the corresponding local conductivity map (middle panel) simultaneously acquired at the same area of rubrene crystal with SAM-decorated steps. A one-to-one correspondence between the topography and the local conductivity distribution is observed. The current profile measured along the dotted line shows that the tip-sample current reaches maxima at the step edges: the highest tip-step current was 7 nA at the tip-sample bias of 0.8 V (lower panel in Figure 15(a)). Figure 15(b) shows the same type of measurement performed on a pristine (no FTS treatment) rubrene crystal. In this case, no local conductivity associated with molecular steps was detected, indicating that the steps of pristine crystals are not conducting, even though they might be unintentionally oxidized. This proves that the conducting pattern shown in

Figure 15(a) is due to the decoration of molecular steps with SAMs. It is important to mention that the observed effect of SAM nucleation at molecular steps is not purely morphological in origin: simply the presence of molecular steps at the surface is not sufficient for the SAM decoration to occur. Indeed, we have not been able to observe any FTS nucleation on crystals that have a high ionization potential, such as tetracyanoquinodimethane (TCNQ), even though TCNQ crystals also show well defined molecular steps at the surface. Consistently, electrical conductivity of TCNQ crystals is not affected by FTS vapor. Therefore, specific chemistry of molecular steps of a sample is important for FTS binding. Most of the organic semiconductors with high ionization potentials (i.e., those that usually form *n*-type OFETs in a combination with gold or graphite contacts) cannot be easily oxidized⁵⁴. Hence, the difference we observed between the responses of the crystals with low and high ionization potential to FTS suggests that oxygen-containing species preferentially located at the steps play a crucial role in anchoring SAMs to the organic surface as supported by theoretical studies in the previous subchapter.

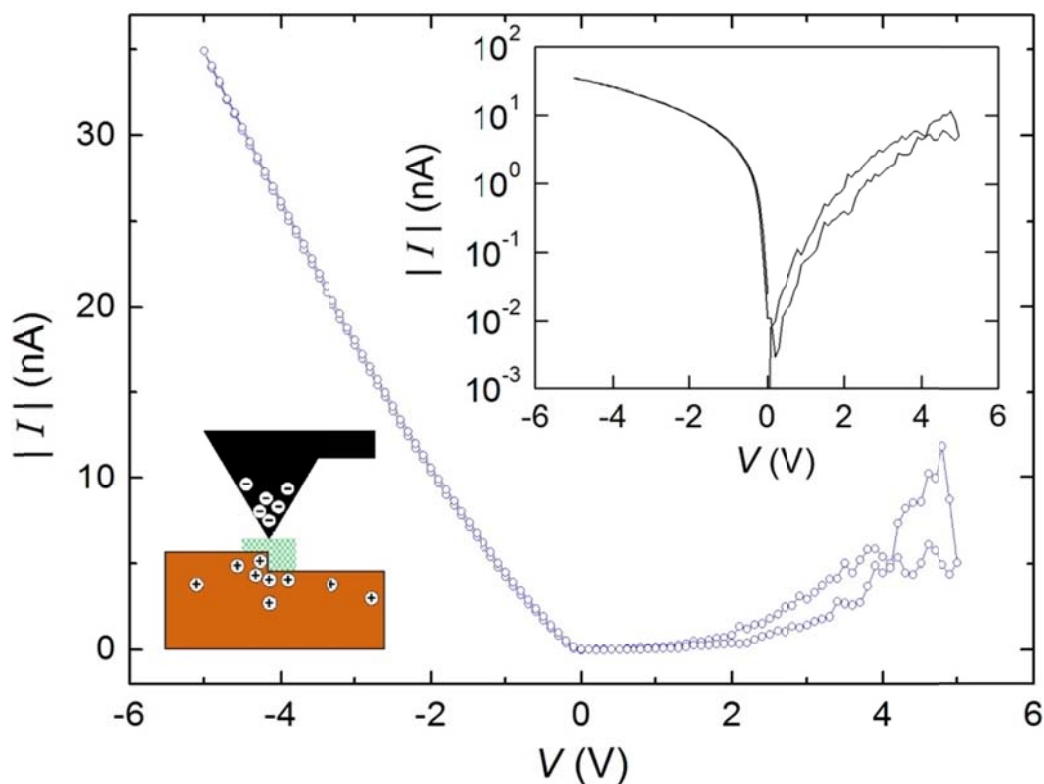


Figure 16. Local I - V curve obtained with C-AFM when the conducting tip is positioned at a SAM-decorated molecular step (the inset shows the same data in a semi-log plot). At negative tip bias, tip-sample current is much larger, which is indicative of the hole conductivity induced by SAM in the crystal. The diagram depicts the model, in which a nanoscale tunneling gap formed between the tip and SAM-induced holes in this biasing regime.

In addition, local current-voltage measurements (I - V) of SAM-decorated molecular steps are performed using a C-AFM tip positioned above a conducting step (Figure 16). These measurements reveal asymmetrical I - V characteristics: at a negative tip bias (relative to the grounded sample), the current is much larger, more linear, and less

noisy than at positive biases. This behavior is consistent with the model of the SAM inducing holes in the crystal. Indeed, when a negative voltage is applied to the tip in contact mode, holes under the SAM are attracted to the SAM-crystal interface, forming a nanoscale “capacitor” with a tunneling barrier consisting of an insulating SAM, as schematically depicted in the inset at Figure 16. At the opposite polarity, no nanoscale tunneling gap can be formed, resulting in a much smaller current.

2.1.3. Kelvin Probe Force Microscope (KFM) Investigation for Partially Coated Rubrene by SAMs

The modification of the surface electronic state from the SAM formation was examined through surface potential measurements by Kelvin probe force microscopy (KFM). Frisbie’s group at University of Minnesota performed KFM measurements of partially SAM-coated rubrene crystals. KFM is known as a superb technique to measure local work function of the surface at the atomic or molecular scales. As a result of KFM measurements, the mechanism of a pronounced increase of the surface conductivity of organic materials by SAM growth is elucidated.

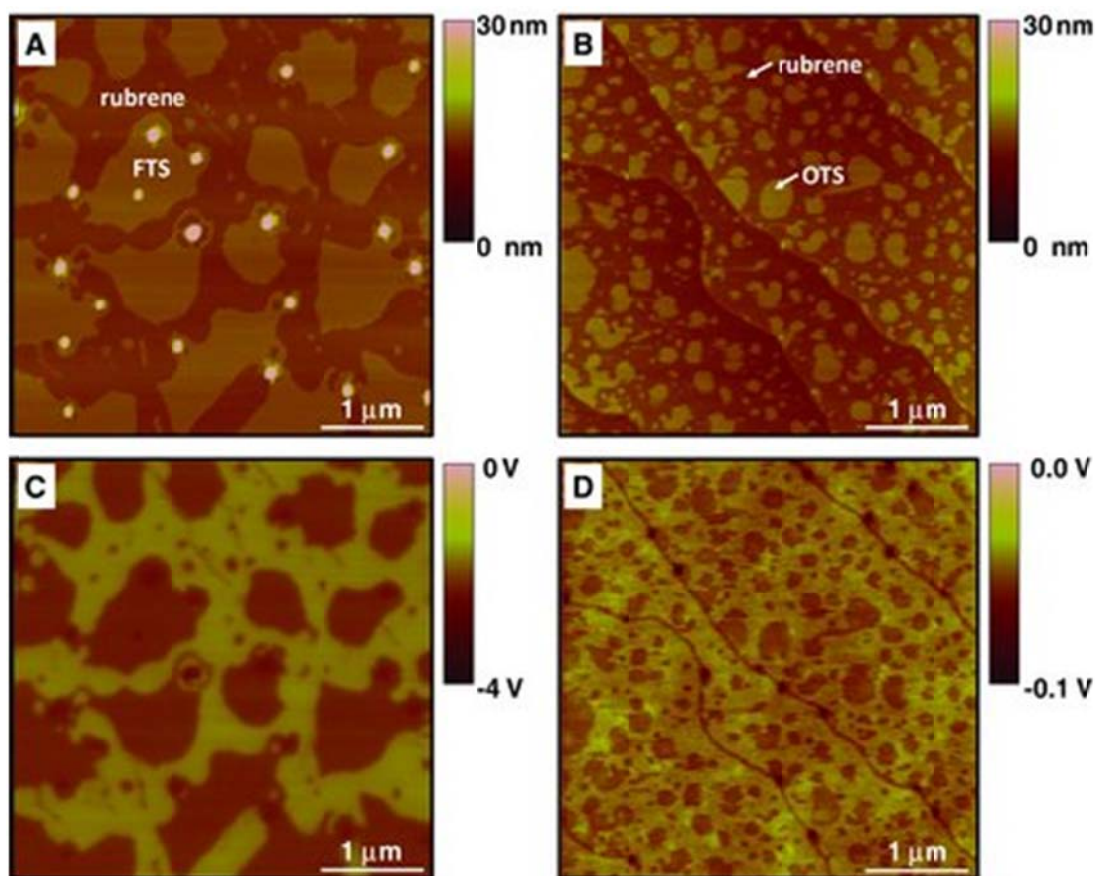


Figure 17. Topography and the corresponding surface potential maps of rubrene partially coated with SAMs. (a) AFM topography of rubrene with 50 % FTS coverage: formation of flat, 1.3 ± 0.2 nm-thick, single-layer islands can be seen as brighter domains. (b) AFM topography of rubrene with 35 % OTS coverage (island thickness is 1.0 ± 0.2 nm). (c) Surface potential image of the FTS-rubrene sample (darker regions correspond to domains with a more negative surface potential). Direct correlation to the SAM morphology in (a) indicates that the electronegative fluoroalkyl tails are pointing away from the substrate. (d) Surface potential image of the OTS-rubrene sample showing similar mapping of more negative surface potential for the SAM islands.

Surface topography images by AFM and the direct mapping of surface potential are shown in Figure (a) – (d). The negative (darker) surface potentials of SAM islands relative to bare rubrene surface are observed in KFM measurements (540 ± 5 mV for FTS and 9 ± 3 mV for OTS). These results solidify the idea of conductivity enhancement manifested by a charge-transfer doping process across the SAM-rubrene interface.

2.1.4. Anisotropy of Charge Transport in Rubrene with SAM-decorated Molecular Steps

Anisotropy of charge transport is known as an intrinsic property of organic molecular crystals due to different molecular packing in the crystal orientation^{36,55,56}. For example, the slipped-stack packing motif of rubrene molecules results in a good π -orbital overlap in b direction of the crystal. Higher strength of intermolecular coupling (transfer integral) along b axis gives rise to a larger π -orbital overlap in this direction, which brings about the higher charge carrier mobility.

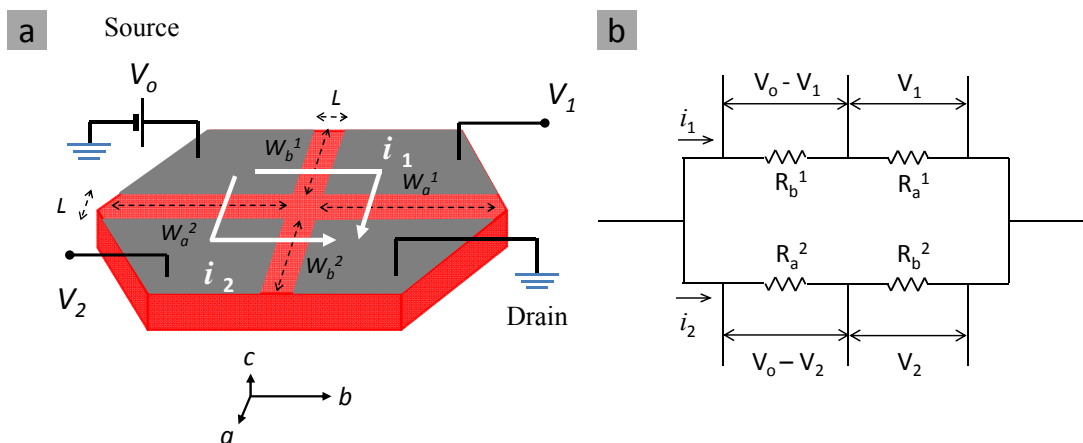


Figure 18. *Anisotropy measurements of charge transport on organic crystalline semiconductor; (a) Schematic diagram of the measurements: Voltage V_o is applied on the source electrode and the potential drop between V_1 or V_2 and the drain electrode grounded are measured. (b) Equivalent diagram of electric circuit to actual devices (left figure 18(a))*

Figure 18 explains the way of anisotropy charge transport measurements on organic crystalline semiconductor. To measure the anisotropy ratio of conductivity along ***b*** and ***a*** crystallographic directions of certain organic crystalline semiconductor ($= \sigma_{\square}^b / \sigma_{\square}^a$), four metal electrodes are deposited through a shadow mask and transport channels are aligned in both ***a*** and ***b*** directions as shown in Figure 18(a). The source bias, V_o , is applied on the source electrode and the drain electrode is grounded. By measuring the potential differences between V_1 or V_2 with respect to the grounded drain electrode, the ratio of the sheet conductivity in ***a*** and ***b*** directions can be calculated based on the following equations. The Figure 18(b) shows an equivalent electric circuit corresponding to the Figure 18(a). There are two dominant current paths, i_1 and i_2 , existing from the source to the drain electrodes. For each current path, ohm's law gives two equations

$$V_o - V_1 = i_1 R_b^1 \text{ and } V_1 = i_1 R_a^1 \quad (11)$$

and

$$V_o - V_2 = i_2 R_a^2 \text{ and } V_2 = i_2 R_b^2 \quad (12)$$

By using the relationship $\sigma_{sqr} = \frac{1}{R_{sqr}} = \frac{1}{R} \left(\frac{L}{W} \right)$, where L and W is resistivity,

channel length and width, respectively, the final anisotropy ratio, $\sigma_{\square}^b / \sigma_{\square}^a (= R_{\square}^a / R_{\square}^b)$, is written as

$$\frac{\sigma_{sqr}^b}{\sigma_{sqr}^a} = \frac{V_1}{V_o - V_1} \left(\frac{W_a^1}{W_b^1} \right) \quad (13)$$

and

$$\frac{\sigma_{sqr}^b}{\sigma_{sqr}^a} = \frac{V_o - V_2}{V_2} \left(\frac{W_a^2}{W_b^2} \right) \quad (14)$$

Note that in this measuring technique, it is sufficient to record only one voltage (V_1 or V_2) at an applied V_o , and the anisotropy ratio can be then calculated using formulas (13) or (14).

By means of this anisotropy measurement technique for FTS step-decorated rubrene samples, we have verified that the early-stage of SAM growth produces quasi 1-D conducting paths along the molecular step edges of rubrene single crystals. Crystallographic properties of high-quality molecular crystals allow molecular steps to extend over great distances on flat facets without intercepting each other. Frequently, molecular steps have similar orientations over the whole area of a large facet (confirmed by AFM). This feature allows us to use macroscopically large structures with contacts prepared by thermal evaporation for measuring in-plane conductivity of an ensemble of decorated molecular steps spanning large area over the crystalline facet, in which the anisotropy in transport of samples varies with decorating the steps by FTS SAM.

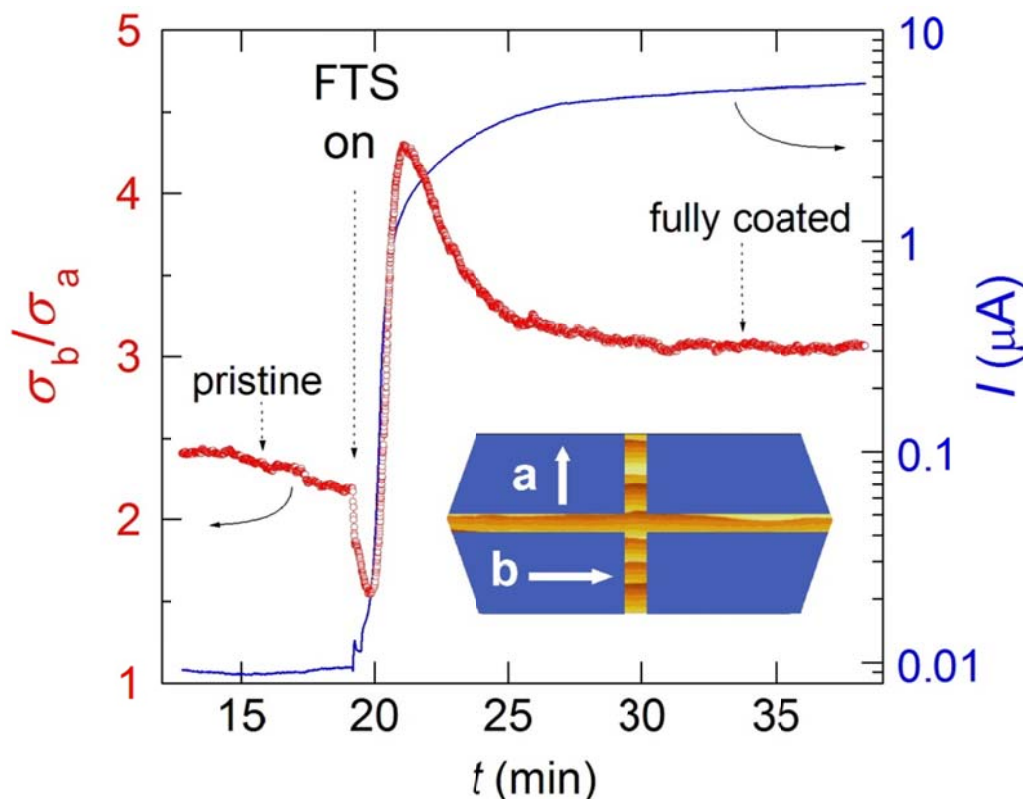


Figure 19. Circles: anisotropy of sheet conductivity, $\sigma_{\square}^b/\sigma_{\square}^a$, measured in-situ at the surface of a macroscopic rubrene single crystal during the growth of the SAM. This is obtained by simultaneously measuring two channels oriented along **a**- and **b**-axes (see inset diagram). Solid line: the corresponding dynamics of the current flowing in the **b**-axis channel at 4 V applied between the contacts. The crystal chosen for these measurements have molecular steps preferentially oriented along the **b** axis, as shown in the inset. The maximum in $\sigma_{\square}^b/\sigma_{\square}^a$ is reached when molecular steps are decorated with SAM.

A number of samples were fabricated with four silver contacts that defined two perpendicular conduction channels. The channel lengths are same as $L = 50$ mm but the

widths are different as $W = 0.5 - 4$ mm, which is determined by the sizes of the crystals. These channels probe charge transport in \mathbf{a} and \mathbf{b} crystallographic directions at the surface of rubrene (Figure 19). By using this structure, we simultaneously measure sheet conductivities in \mathbf{a} and \mathbf{b} directions *in situ*, while the crystal is treated with FTS vapor. Figure 19 shows the dynamics of the current, $I(t)$, flowing in one of the channels (solid line) and the ratio of sheet conductivities, $\sigma_{\square}^b / \sigma_{\square}^a(t)$ (circles), for the sample with molecular steps preferentially oriented along \mathbf{b} -axis. According to our observations, the typical values of $\sigma_{\square}^b / \sigma_{\square}^a$ before FTS SAM treatments were between 2.5 and 3, which is consistent with the results from the transport anisotropy measurements in field-effect transistors^{36,55,56}. During the initial stages of SAM growth, i.e., when a rapid increase of the current was observed, $\sigma_{\square}^b / \sigma_{\square}^a$ showed a maximum at about 1 - 2 min after the beginning of FTS exposure. Comparison with the AFM data (Figure 13) suggests that this maximum corresponds to the formation of SAM-decorated conducting steps running preferentially in \mathbf{b} direction. This measurement provides a timescale, at which SAM decoration of molecular steps occurs ($\sim 1 - 2$ min), as well as an additional confirmation that the SAM-decorated steps are conducting. After a few hours, rubrene surface was fully covered by FTS SAM and the maximum conductivity was reached. The anisotropy post step-decorating period started decreasing and eventually saturated to be 3, the near value of the initial anisotropy. The discrepancy between the initial and final anisotropy ratios can be explained by the modification of the contact resistance due to doping effect from SAM growth.

2.2. Growth of Alkyl-silane SAMs on Conjugated Polymers

Conjugated polymers are complementary solution-processable semiconducting materials with intriguing optoelectronic properties⁵⁷⁻⁵⁹. Since our primary interest stems from the observation of a large increase in conductivity induced by SAM deposition on the surface of organic single crystals, we extended our studies of SAM functionalized organic semiconductors to a class of solution-processable conjugated polythiophenes^{13,17}. It is demonstrated that the interaction of these polymers with hydrolyzed fluoroalkyl trichlorosilane (FTS) results in a drastic modification of the electrical and optical properties of these semiconducting polymers. Spin-coated polymer films on glass substrates were prepared according to optimized procedures written in the previous chapters of sample preparation. FTS SAM doping was done as the similar process used on molecular single crystals.

2.2.1. Electrical Modification of Conjugated Polymers by FTS

SAM Doping

Upon bulk doping with FTS SAM, the electrical conductivity of ultrathin polythiophene films increases by up to six orders of magnitude, reaching $(1.1 \pm 0.1) \times 10^3 \text{ Scm}^{-1}$ for poly (2,5-bis(3-tetradecylthiophen-2-yl)thieno[3,2-b]thiophene) (PBTtT) and $30 \pm 20 \text{ Scm}^{-1}$ for poly(3-hexyl)thiophene (P3HT); the corresponding average sheet conductivities are 2.2 and $0.1 \text{ mS}_{\square}^{-1}$.

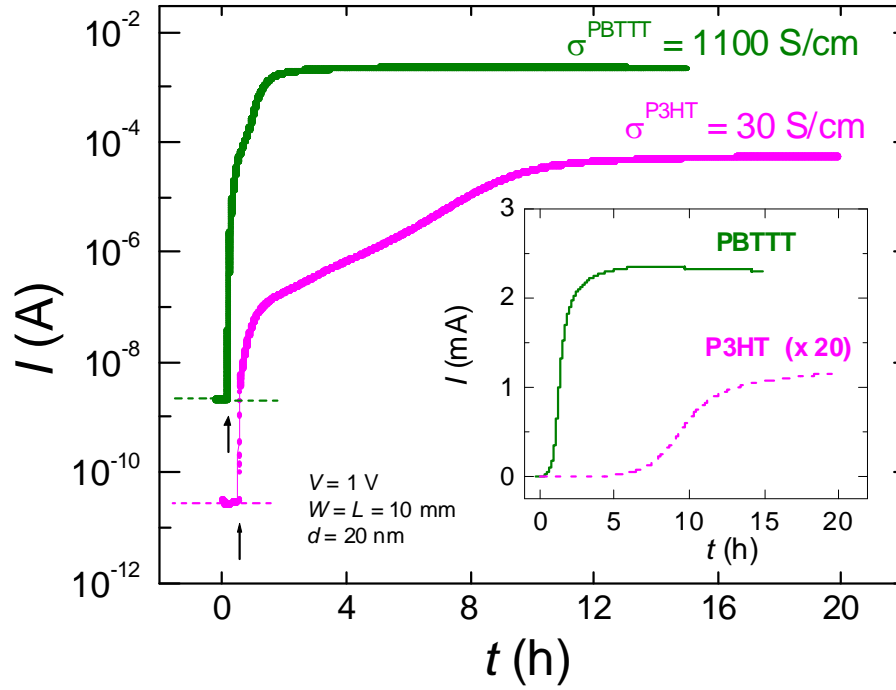


Figure 20. Time evolution of DC current, $I(t)$, through ultra-thin P3HT and PBTTT films as the samples are exposed to the saturated vapor of fluoroalkyl trichlorosilane (FTS) (the arrows indicate the moment when the vapor is introduced in the test chamber). The inset shows the same data on a linear scale. P3HT and PBTTT thin films were spin coated on glass; the film thickness is 20 nm; the contacts are made of colloidal graphite; the width and length of the channel are $W = L = 1 \text{ cm}$; the applied dc bias is 1 V.

Figure 20 shows that the conductivity changes during FTS SAM growth on the polymer films. When P3HT or PBTTT is exposed to FTS vapors, the conductivity rapidly increases and reaches a high saturated doping state. These conductivities that we obtained by doping polythiophenes with FTS SAM are the highest among this class of polymers

using small-size dopants, such as I_2 , PF_6^- , ClO_4^- obtained earlier⁵⁸⁻⁶¹. Typically, polymer samples doped with small ions and molecules display relatively poor stability (especially in vacuum), because of the rapid diffusion of small-size dopants in the polymer matrix. On the contrary, FTS-doped samples exhibit a remarkable stability: the conductivity does not show any decay in high vacuum and only a very minor drift ($\sim 0.5\%$ per hour) in an atmosphere of non-polar gases. It is important to emphasize that doping in our experiment is performed at a solid-vapor interface, using highly-ordered polythiophene films, which allows the use of well-characterized structural, morphological and transport properties of these polymers as a starting point for the analysis of our data. The values of σ above have been calculated using the thickness of undoped films (20 ± 3 nm) confirmed by AFM profile. These estimates are justified, because silane molecules are not conducting even in the cross-linked state and the total number of conjugated chains in the cross-section of the film (the conducting channels) remains roughly the same as before the doping. Although the nature of silane-polythiophene chemical interaction is not clear at this stage of investigation, the stability of the doped state in high vacuum points to a relatively strong interaction. Our X-ray photoelectron spectroscopy (XPS) and Rutherford back scattering (RBS) data showed that there was virtually no chlorine present in the films after vapor phase FTS doping, which suggests that fluoroalkyl trichlorosilane has hydrolyzed *in situ*, either as a result of water trapped in the polymer film or water vapor present in the doping chamber⁶². Such hydrolyzed silanes are known to readily self-condense and polymerize to form partially cross-linked siloxane polymers^{63,64}. On silicon dioxide surfaces these can bind to the free surface hydroxyl groups to form monolayers. In the present case, we believe that FTS is converted into a

partially cross-linked siloxane non-volatile polymer within the film, which accounts for the high stability of our samples observed under vacuum. In addition, low-concentration oxygen defects known to be present in polythiophenes might serve as anchoring sites for hydrolyzed FTS⁶⁵. The mechanism of the doping of the conjugated polymer by FTS is unclear, but may be similar to the mechanism of SAM-induced surface conduction in small-molecule organic crystals, where an electronegative SAM molecule induces an electron transfer across the SAM-crystal interface¹³. To fully understand the mechanism of FTS incorporation and functioning, nanoscale structural details of FTS-polythiophene samples should be investigated. For instance, one of the intriguing questions is whether FTS molecules break apart individual π - π stacked crystalline nanofibrils and domains, known to constitute P3HT and PBTTT films⁶⁶⁻⁶⁸, or do they merely bind to the surface of these crystallites. The monolayer character of FTS on molecular crystals and very high (nearly metallic) conductivity of FTS-doped polythiophenes point to the latter scenario, in which the π - π stacking required for a good charge transport is preserved. Understanding the detailed chemical structure and composition of these functionalized electronic materials is very important. Ion scattering spectroscopy and XPS have been used to study the elemental composition of FTS-doped polythiophene films. Our preliminary data indicate that fully doped samples contain approximately one FTS molecule per thiophene ring, with an areal density of fluorine atoms $117 \times 10^{15} \text{ cm}^{-2}$, which corresponds to a three dimensional density of FTS molecules, $n_{\text{SAM}} = 4.5 \times 10^{21} \text{ cm}^{-3}$ associated with the 13 F atoms per FTS molecule. Using simple conductivity arguments ($\sigma = en_h\mu$), in which $\sigma = 30 \text{ S}\cdot\text{cm}^{-1}$ is the three dimensional saturated conductivity of doped P3HT, e is elementary charge, and $\mu \sim 0.1 \text{ cm}^2\text{V}^{-1}\text{s}^{-1}$ is a typical

hole mobility in P3HT^{67,69}, one can estimate the density of FTS-induced holes: $n_h = 1.9 \times 10^{21} \text{ cm}^{-3}$, which is comparable to the very high carrier density induced in P3HT by electrolyte gating⁷⁰. Quantitative agreement between the densities of FTS molecules and charge carriers doped into the system obtained by the two independent techniques (ion scattering and conductivity) suggests that one hole is doped into the polymer per FTS molecule on average. The very large doping level (approximately one hole per thiophene ring), a very good stability of the conducting state in high vacuum and the lack of chlorine in XPS and RBS spectra indicate that the doping effect is due to hydrolyzed FTS.

2.2.2. Optical Modification of P3HT and PBTTT Doped by FTS

SAM

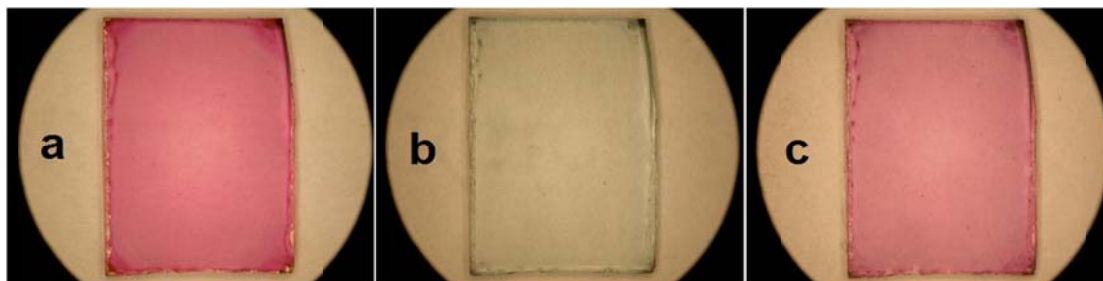


Figure21. Photographs of a 20 nm-thick PBTTT film spin coated on $1 \times 1.5 \text{ cm}^2$ glass slide: (a) as spun insulating film, (b) doped with FTS to saturation (highly conductive), and (c) restored (dedoped) in air under ambient illumination for 16 h (insulating).

Contrary to densely packed molecular crystals, where the SAM growth is restricted to the surface, FTS molecules penetrate deep into the nano-porous polymeric

materials, interact with the surface of individual nano-crystalline domains and dope the entire film. This behavior could be detected using different methods and was most strikingly observed by a strong suppression of interband optical absorption of the polymer that makes the samples almost completely transparent (Figure 21).

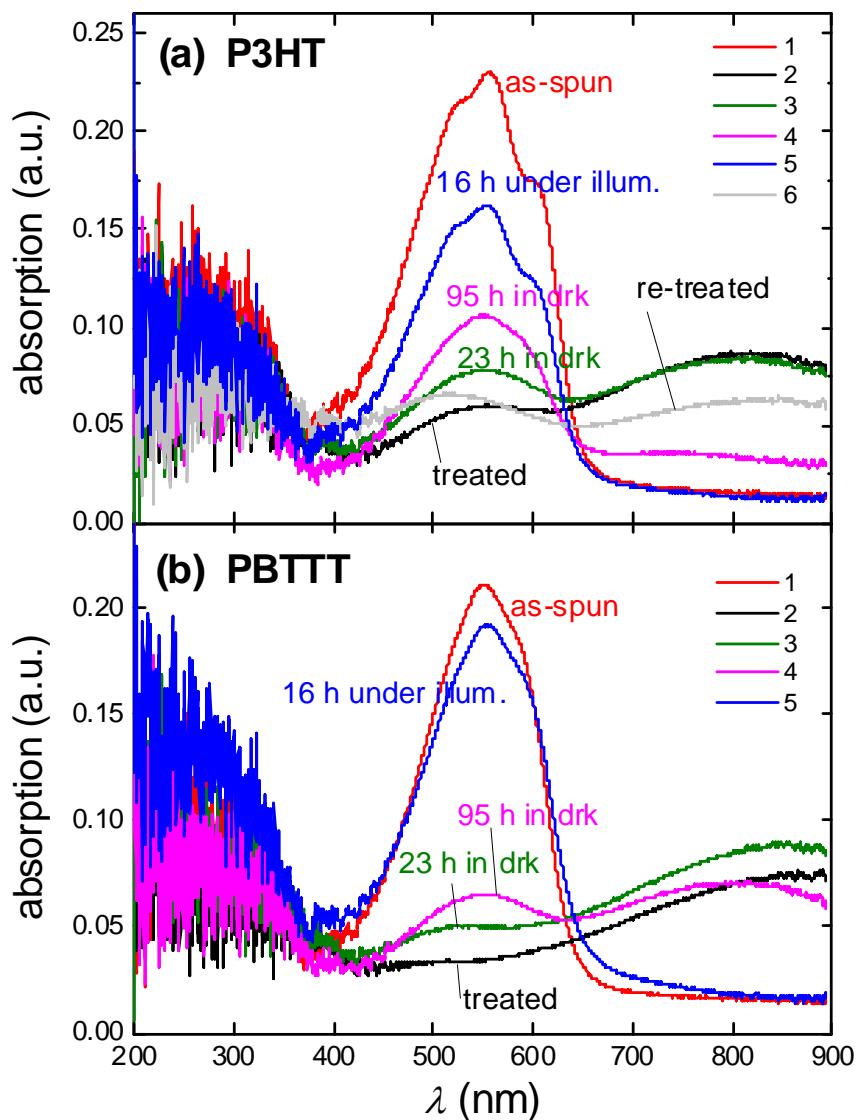


Figure 22. *UV-vis absorption spectra of ultrathin films of (a) P3HT and (b) PBTTT. A drastic reduction of absorption by FTS doping is evident. The curves are numbered as follows: 1 (red) – as spun annealed films; 2 (black) – treated with FTS to saturation; 3 (green) – dedoped in air in the dark for 23 h; 4 (pink) – dedoped in air in the dark for 95 h; 5 (blue) – dedoped in air under illumination with a white light for 16 h; 6 (grey) – doped again with FTS after dedoping.*

In order to characterize this “bleaching” effect, we have measured optical absorption of FTS-doped samples (Figure 22). The pristine samples exhibited a broad interband absorption peaked at ~ 560 nm (2.21 eV), as expected (curve 1). Both P3HT and PBTTT exhibited vibronic bands indicating high structural order in the samples. The vibronic bands are more obvious in P3HT, where they are separated by 0.16 ± 0.02 eV, in agreement with the 1450 cm^{-1} Raman stretching mode of the C=C bond. Once doped with FTS to the maximum conductivity, the interband optical absorption of the samples was almost completely suppressed (curve 2), while another broad long-wavelength band appeared simultaneously at $\lambda \geq 800$ nm. Interestingly, if the samples were exposed to ambient air, their absorption spectra and the original purple color, as well as the initial high electrical resistivity, recovered within days in the dark or within hours under ambient illumination (curves 3, 4, and 5). At the end of this recovery process, the samples reached the initial insulating state with σ and λ_{max} similar to the pristine polymers, suggesting that doping/dedoping cycle did not damage the conjugated backbone of the polymer. As it will be shown in the below subchapter, this dedoping effect is not due to the evaporation of FTS molecules from the sample, but rather it is an electronic effect.

It has been shown that due to the non-degenerate ground state of polythiophenes, the lowest-energy excitation in these polymers is a bipolaron (two solitons on a conjugated chain attracted to each other and creating a weakly localized pair⁶¹). Prior studies of optical absorption of P3HT have shown that the interband transition of pristine (undoped) polymer centered at 2.2 eV (560 nm) decreases upon dilute doping with LiClO₄ and NOPF₆ with a simultaneous appearance of two new broad absorption bands at 0.4 eV ($\sim 3 \mu\text{m}$) and 1.6 eV ($\sim 800 \text{ nm}$) indicative of the formation of bipolarons^{61,71}. The two new bands correspond to optical transitions from the HOMO to the new gap states associated with bipolarons. An increase of doping to the highest concentration (saturation doping) leads to a complete “bleaching” (suppression) of the interband transition and transformation of the bipolaronic bands into a very broad low-energy shoulder in the absorption spectrum that corresponds to delocalized polarons in highly conducting samples. The absorption spectrum approaches that of a metal with free carriers^{61,72,73}. Similar effects have also been observed in doped polyaniline. In our UV-Vis measurements, the spectral range of our apparatus did not allow the observation of the full evolution of bipolaronic bands. Nevertheless, the drastic suppression of the interband absorption at 560 nm ($\sim 2.2 \text{ eV}$) and the appearance of the broad long-wavelength peak at $\lambda > 650 \text{ nm}$ ($< 1.9 \text{ eV}$) shown in Figure 22 are both consistent with prior studies and indicate that doping of P3HT and PBTTT with FTS results in a metallic-like state with a high density of mobile polarons. Interestingly, calculations predict that wavefunctions of polarons and bipolarons should significantly overlap at these high carrier densities that might lead to the formation of “polaron or bipolaron lattices”⁷⁴.

2.2.3. AFM and SEM Investigation into SAM Growth in Polythiophene Films

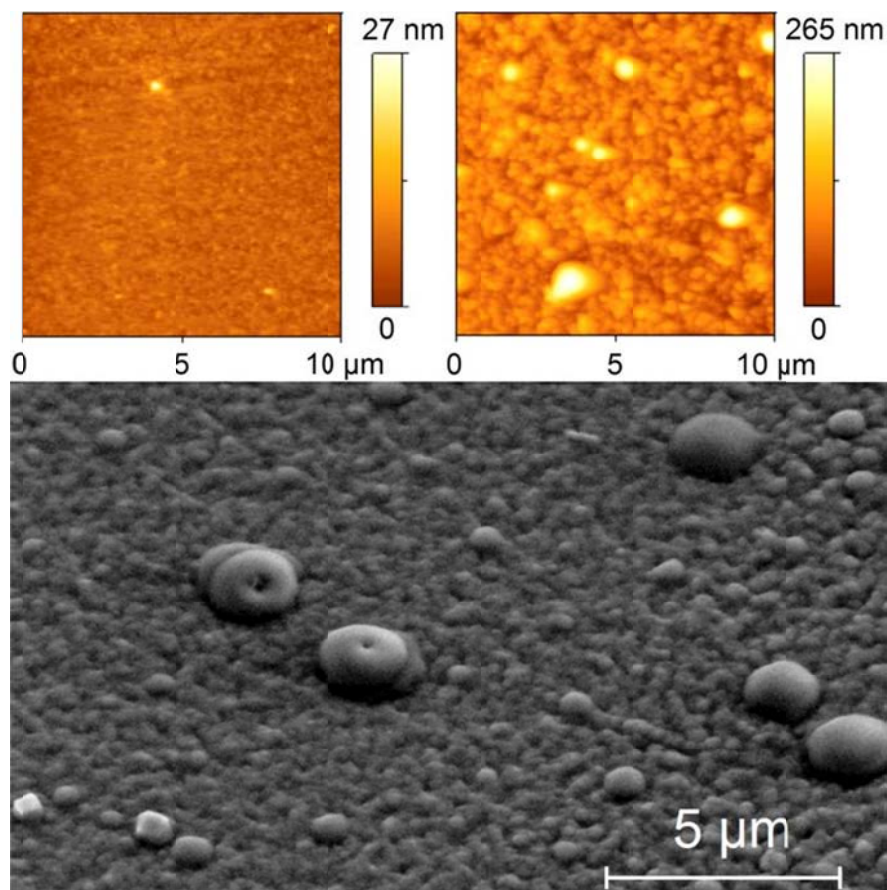


Figure 23. *AFM image of pristine P3HT (top left), AFM image of FTS-doped P3HT (top right), and SEM image of FTS-doped P3HT (bottom). SEM of pristine P3HT could not be reliably obtained because of the severe charging issues with non-conducting samples. Both AFM and SEM show swelling of the polymer after doping with FTS. The dedoped (recovered) samples exhibit the same swelled morphology, identical to the freshly doped films, suggesting that FTS molecules are not removed from dedoped films.*

AFM and SEM images showed that when FTS molecules were incorporated into the sample, there was an increase in roughness resulting in a bumpy surface morphology of the doped films (swelling) due to the possible self-polymerization of FTS in the polymer matrix (Figure 23). This is consistent with the permeable nano-porous structure of the polymers, confirming the bulk character of the doping in this case. Interestingly, AFM images of freshly doped and dedoped samples are very similar (SEM of pristine and dedoped insulating samples could not be obtained due to the sample charging). This indicates that FTS molecules are likely not removed from the samples physically during dedoping, and the primary role of dedoping is to “switch off” the conducting state. Another indication that FTS molecules do not “escape” from the polymer film is provided by the high stability of the conducting state on a long-term storage under high vacuum. SEM images of pristine and dedoped insulating samples could not be obtained due to sample charging.

2.2.4. Sensing and Dedoping Effects of FTS SAM-doped Polythiophene Films

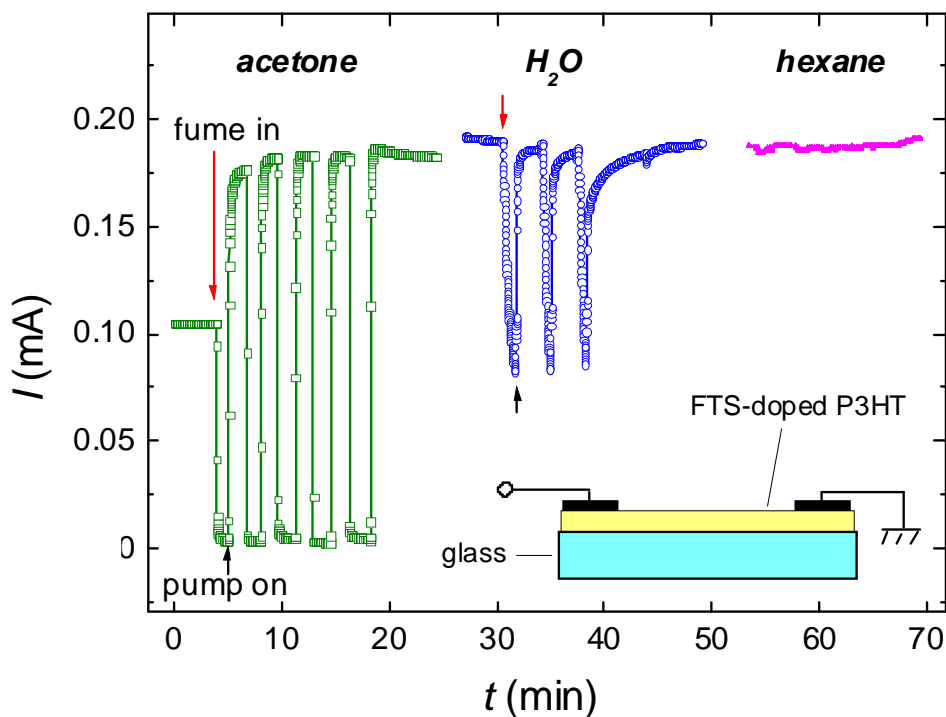


Figure 24. Response of conductivity of FTS-doped P3HT to polar analytes (sample geometry is shown schematically). When the sample is exposed to saturated vapors of polar solvents, the conductivity rapidly decreases; it fully recovers on vapor removal by pumping. The greatest and fastest response is observed for highly polar vapors (e.g., acetone). There is no sensitivity to non-polar molecules (e.g., hexane). Measurements were carried out at an applied voltage of 1 V in the dark.

Highly conductive FTS-doped polythiophenes exhibits interesting sensing properties. Figure 24 shows a dark conductivity response of FTS-doped P3HT to vapors of acetone, water and hexane. An immediate and large (~100%) decrease of conductivity was observed on exposure to saturated vapor of acetone. The conductivity recovered readily on vapor removal by pumping. A similar, but smaller in magnitude response was observed with H₂O vapor. Hexane, which is a nonpolar molecule, did not have any effect on the conductivity. Interestingly, this behavior is similar to the sensing effect observed in FTS-coated rubrene, which suggests that sensing in these two systems has a common origin likely related to dipolar interaction of analytes with FTS SAM¹³. In the case of conjugated polymers, however, solution processability, availability of large-area samples and mechanical flexibility of these materials make SAM-functionalized polymers especially attractive for applications.

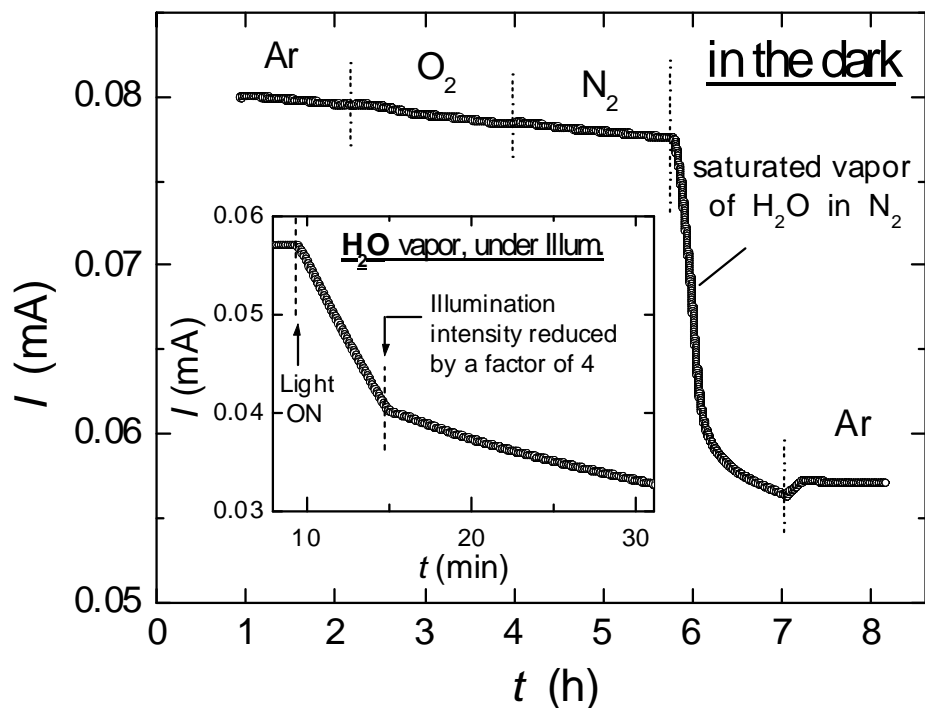


Figure 25. Effect of exposure to various gases on the conductivity of FTS-doped P3HT film measured in the dark (main panel) and under illumination with white light (inset). H_2O vapor is the main cause of the conductivity decrease in air. The decay rate increases under the illumination.

In order to understand the dedoping effect (i.e., the recovery of optical and electrical properties, when FTS-doped polythiophenes are exposed to air), highly conducting FTS-doped P3HT samples were exposed to various UHP gases in the dark and under illumination while the conductivity was monitored (Figure 25). White light with a smooth spectrum in the visible range (a 20 W quartz-tungsten-halogen lamp) was

used for an illumination. Intensities were kept sufficiently low to avoid radiative heating of the sample. As a result, inert gases (e.g., Ar and He) and the nonpolar gases present in air (O_2 and N_2) had no effect on the conductivity of FTS-doped polymers: there was only a very slow, gas-independent drift of σ at the very small rate of ~ 0.5 % per hour (the initial portion of the curve in Figure 25). However, when a saturated vapor of H_2O was introduced into the test chamber, an obvious decay of σ occurred. Under illumination, this decay proceeded much faster, with the rate proportional to the illumination intensity (inset in Figure 25). Instantaneous changes in light intensity resulted in almost instantaneous changes in the decay rate (the inset in Figure 28 shows that reducing the illumination intensity by a factor of 4 causes the decay rate to decrease by a factor of ~ 4 , which produces a “knee” in the time dependent current). This indicates that dedoping under illumination is a photo-induced electronic effect, rather than an artifact of the sample heating under illumination. Our experiment clearly shows that the dedoping of SAM-polythiophene samples in air is caused by water vapor. More generally, dedoping can be deliberately induced by exposing the samples to vapors of polar analytes, such as ketones, alcohols or water. In the dark, the dedoping is fully reversible, which is beneficial for the development of electrical chemo-sensors. One explanation for this effect is that it is caused by conformational changes of the polymer backbone induced by a dipolar interaction of (fluoro)alkyl SAM molecules with polar analytes. Such conformational changes are known to effectively reduce the conjugation length of polymers and affect their physical properties^{58,75}. Alternatively, one would expect polar analytes to interact strongly with the free silanol groups within siloxane backbone formed

in situ, which might reverse the protonic doping effect and switch off the conducting state. Understanding the actual mechanism of this effect requires further studies.

Overall, this experiment shows that the analyte responsible for the de-doping of these samples in air is H₂O, in agreement with the humidity related degradation of *p*-type conductivity observed in polythiophene FETs. The sensing effect shown in Figure 24 can be more generally interpreted as reversible dedoping caused by polar molecules. Full reversibility of this effect indicates that volatile analyte molecules are easily removed from the sample by pumping, while FTS molecules remain in the film. This suggests that the molecules of polar solvents are more weakly absorbed in the sample, while FTS molecules are bound to the polymer much more strongly.

2.3. Growth of Alkyl-silane SAMs on Graphite and Graphene

Other than small-molecule and conjugated polymer organic semiconductors, the effect of a self-assembled monolayer of fluoroalkyl trichlorosilane (FTS SAM) on the electronic properties of *highly-ordered pyrolytic graphite* (HOPG) and *graphene* is reported. The latter system has attracted considerable attention due to the massless character of quasiparticles and the related novel mesoscopic transport properties⁷⁶. The studies using atomic-force microscopy (AFM), scanning electron microscopy (SEM), x-ray photoelectron spectroscopy (XPS), and Hall effect measurements reveal that a dense, uniform and stable FTS SAM can be grown at the surface of graphene, inducing an excess of holes with a density of up to $n \sim 1.5 \times 10^{13} \text{ cm}^{-2}$. Such level of doping is unattainable in conventional field-effect transistor (FET) devices. In addition, the SAM-

graphene system is found to be very stable (even at elevated temperatures) in high-vacuum or ambient environment. Such robustness and the large electronic effect suggest that integration of SAM with graphene provides a new and reliable method of achieving ultra-high doping levels in graphene.

2.3.1. Electrical Modification of Graphite by the Growth of FTS SAM

The samples used in this study were rectangular pieces of multilayer HOPG. The HOPG samples had length and width, $L \sim W = 2 - 5$ mm, and thickness $d = 3 - 20$ μm , comprising $1-6 \times 10^4$ individual layers (Figure 26). The electrical contacts to HOPG were prepared by applying colloidal graphite paint to the sides of the samples, thus forming electrical contacts to all the layers. Before SAM growth, devices were annealed in a flow of ultrahigh purity (UHP) argon at 120 $^{\circ}\text{C}$ for 90 min and transferred under argon to FTS growth chamber (this step is necessary for achieving a high quality SAM on graphene). The chamber was evacuated and then the samples were exposed to saturated vapors of FTS. Electrical characteristics of the samples were measured *in-situ* during SAM growth. Control experiments were also performed to verify that no intercalation of SAM molecules or any by-products of their growth occurred in the bulk of the HOPG samples, confirming that the changes of the electrical conductivity observed were indeed due to a very strong doping of the top (exposed) graphite layer.

As the result of an FTS treatment, the resistance of HOPG samples typically decreased by 5 - 20%, observed both in 2-probe and 4-probe configurations (Figure 26(a),

top panel). The magnitude of the decrease depends on the thickness and the initial resistance, R_0 , of these macroscopically thick samples: $R(t) = \alpha(t) \cdot R_0$, where $\alpha = 0.8 - 0.95$ in the saturated state. Such a considerable decrease of R in samples with a typical number of layers $N = 1 - 6 \times 10^4$ suggests that SAM modification of the top graphite layer is very strong. Indeed, since the screening length in graphite is only $\sim 0.5 \text{ nm}^{77}$, only resistance of the top layer should be affected, and the sample can be represented by $N-1$ undoped layers and one (top) doped layer connected in parallel. Hence, the resistivity of the top layer can be expressed as:

$$\rho = \left(\frac{W}{L} \right) \cdot \frac{\alpha N}{N(1 - \alpha) + \alpha} \cdot R_0, \quad (15)$$

where the coefficient $\alpha(t) \equiv R(t)/R_0$ is determined experimentally from $R(t)$ measurements (upper panel of Figure 26(a)). Hence, for a $3.5 \text{ }\mu\text{m}$ -thick sample with $N \approx 1.16 \times 10^4$ and $\alpha(t \geq 30 \text{ min}) = 0.92$ (the 8% blue curve in the upper panel of Figure 26(a), eq. (15) gives the resistance of the top layer, $\rho_{\square}(t)$, decreasing from $\sim 70 \text{ k}\Omega/\square$ to $\sim 65 \text{ }\Omega/\square$ (i.e., by $\sim 10^3$ times), as the result of the SAM doping (lower panel of Figure 26(a)).

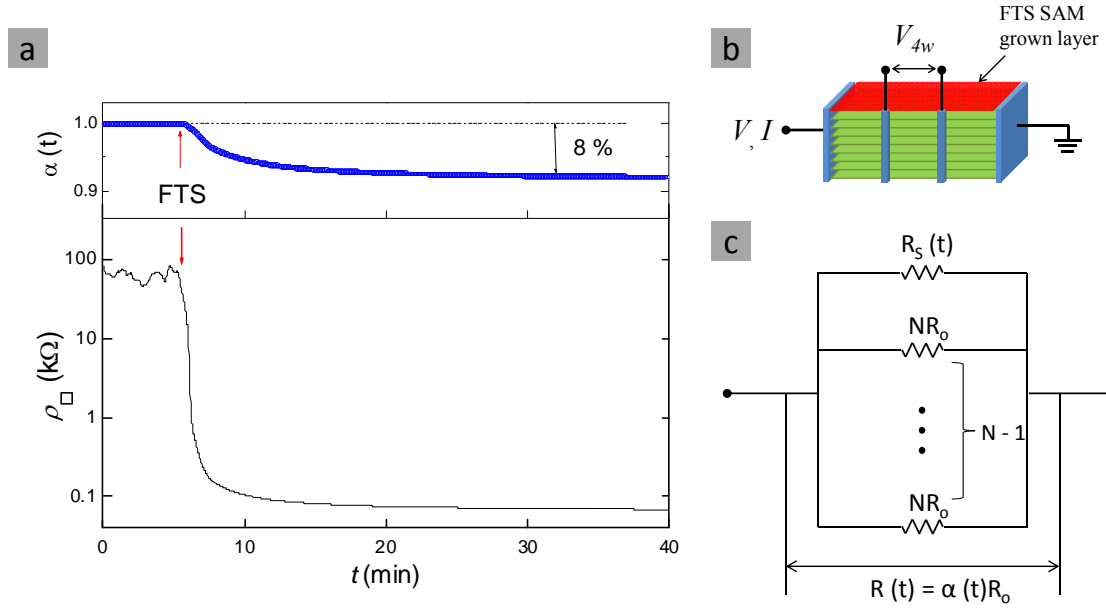


Figure 26. The effect of an FTS self-assembled monolayer on the resistivity of HOPG. (a) (Top): normalized resistivity $\alpha(t) \equiv R(t)/R_0$ of multilayer ($> 10^4$ layers) HOPG measured as a function of FTS treatment time (initial values of R vary from sample to sample by as much as 100%). The red arrows indicate the onset of FTS exposure. (Bottom): the corresponding effect on the resistivity of an individual graphite layer calculated using Eq. (15). (b) The sketch shows 4-probe sample geometry used in this study. (c) An equivalent electrical circuit of multilayered HOPG is depicted. The modification of resistance of top layer by FTS SAM doping can be extracted from the bulk contribution through Eq. (15).

2.3.2. AFM and SEM Investigation for SAM Growth on Graphite

In order to understand nanoscale morphology of the SAM-graphene system, AFM and SEM studies of partially and fully coated samples were performed. Figure 27(a) shows an AFM of a pristine HOPG (~ 0.1 nm rms roughness): faint thin lines are ~ 0.3 nm-high graphene steps. AFM of a partially coated surface is shown in Figure 27(b) and (c). Three types of morphology were observed: round islands sparsely distributed on the surface (Figure 27(b)), ribbon-like regions corresponding to the SAM growing along the graphene steps (Figure. 27(b)), and smaller, irregular-shape islands with a higher nucleation density (Figure 27(c)). The topography shows that all these islands are flat regions with the thickness 1.0 ± 0.2 nm, which is consistent with the length of FTS molecule (the last panel at Figure 27). The variations in the morphology likely originate from different types and densities of defects on graphene surfaces that form SAM nucleation sites. AFM of a fully coated surface has a flat, but “fuzzy” morphology with a ~ 0.37 nm rms roughness (Figure 27(d)), which is consistent with the interaction of an AFM tip with a soft SAM. Figure 27(e) shows a $200 \times 200 \mu\text{m}^2$ SEM image of HOPG partially coated with FTS. A surprisingly high (for a monolayer) electronic contrast in this SEM image is likely due to the electron-rich fluoroalkyl groups of the SAM, which allows for a clear identification of the monolayer growth pattern on a large scale. In this sample, it appears that the SAM nucleation had occurred along the cracks, followed by a lateral spreading of the monolayer along the surface. These images, taken at various stages of the SAM formation, confirm that FTS forms a monolayer at graphite surface.

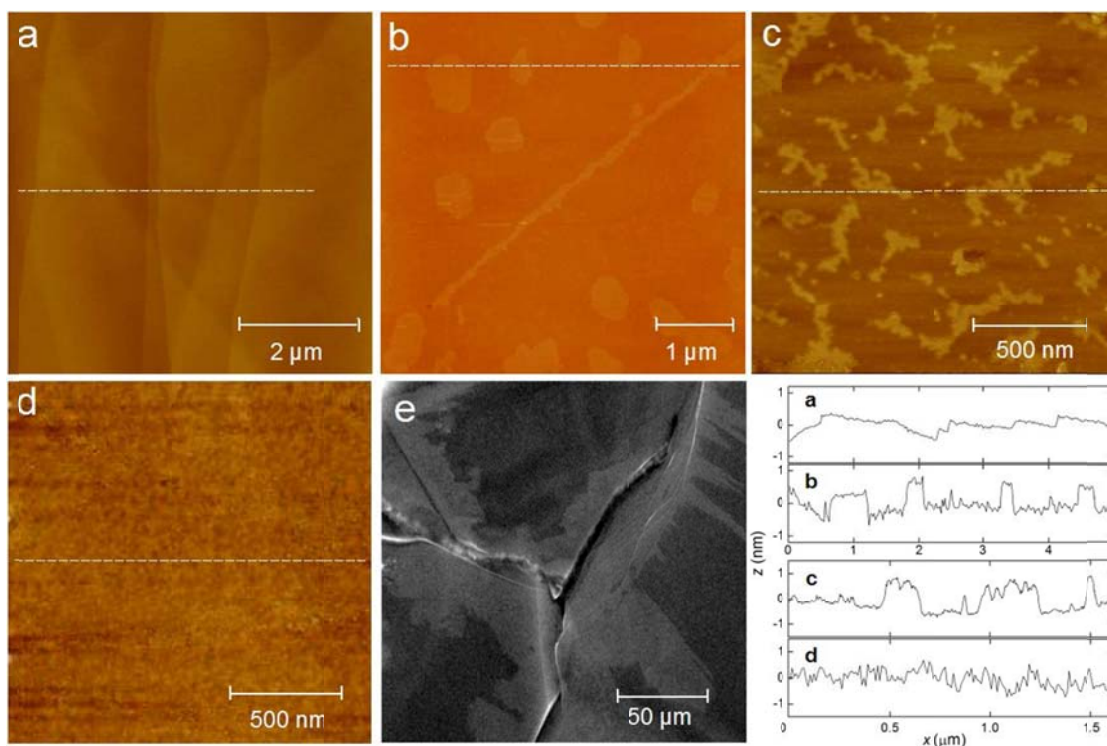


Figure 27. AFM (a, b, c, d) and SEM (e) of graphite surface functionalized with FTS SAM. (a) AFM of pristine HOPG surface (0.1 nm rms roughness); (b and c) AFM of partially coated samples (1-2 min FTS exposure), showing different morphologies of SAM islands, including SAM-decorated graphene edge in b; (d) AFM of a fully coated sample (1 hour exposure) showing a “fuzzy” surface morphology with 0.37 nm rms roughness; (e) a large-area SEM image of a HOPG sample partially coated with the SAM (10 min exposure), with lighter shade corresponding to SAM-coated regions. The last panel shows AFM profiles taken along the dotted lines in a, b, c and d, indicating that the layer is 1 nm-thick.

2.3.3. XPS Investigation on SAM Grown Surface of Graphite

Elemental composition of SAM on graphite has been investigated by XPS (Figure 28). By obtaining statistics on many FTS-HOPG samples, a clean graphite surface is very important for successful SAM growth. Graphite samples were exfoliated freshly and annealed in a flow of UHP Ar at 120 °C for ~ 90 min with a subsequent transfer them into the FTS chamber without exposure to air. Comparing the areas of F 1s and Si 2p peaks of the FTS-HOPG sample (the upper spectrum) gives F/Si ratio of 12.7 ± 0.5 , which is in a good agreement with the actual molecular stoichiometric ratio of 13.

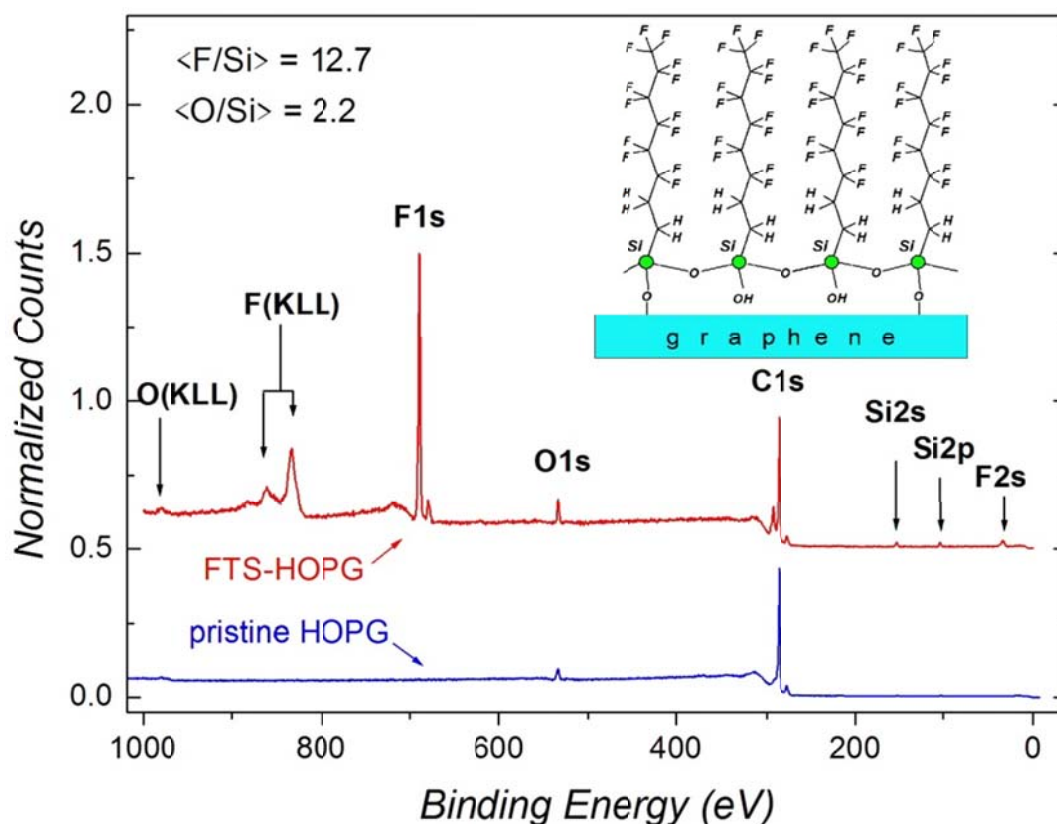


Figure 28. XPS of pristine (upper spectrum) and FTS-coated (lower spectrum) HOPG. Quantitative analysis based on the comparison of peak areas gives the following elemental ratios: $F/Si = 12.7 \pm 0.5$ and $O/Si = 2.2 \pm 0.2$ (compare with the theoretical values $F/Si = 13$ and $O/Si = 2$ for the model in the sketch). A small oxygen signal clearly present in pristine samples is consistent with oxidized graphene steps that likely play an important role in SAM nucleation. Absence of Cl in the spectra indicates that the monolayer is fully hydrolyzed. The sketch shows the suggested chemical structure of the SAM-graphene system.

XPS data also helps to understand the growth mechanism of FTS SAM on HOPG. XPS data shows no chlorine related signal (the Cl peak would have appeared at ~ 200 eV), indicating that all FTS molecules also undergo a complete hydrolysis. A small O 1s signal, clearly observed in all freshly exfoliated HOPG samples (the lower spectrum), is consistent with graphene steps unintentionally functionalized with O-containing groups. Oxygenated species at these steps may play a key role in the SAM nucleation. During the initial phase of growth, some FTS molecules are covalently bonded (Si-O-C) to these defects. Once such “anchoring” sites are formed, other FTS molecules can covalently attach to them (Si-O-Si) without forming bonds to the sample surface (see the inset of Figure 28). As a result, most FTS molecules in a SAM layer are only bonded to two neighboring FTS molecules, with the other OH group left dangling. In such a case, the O/Si ratio should be slightly higher than 2, as confirmed by our experimental value 2.2. The fact that no chlorine signal detected in XPS measurements also provides a solid proof for that the observed doping effect is not induced by Cl byproducts of the SAM formation.

2.3.4. Hall-effect Measurement on SAM Grown Graphite

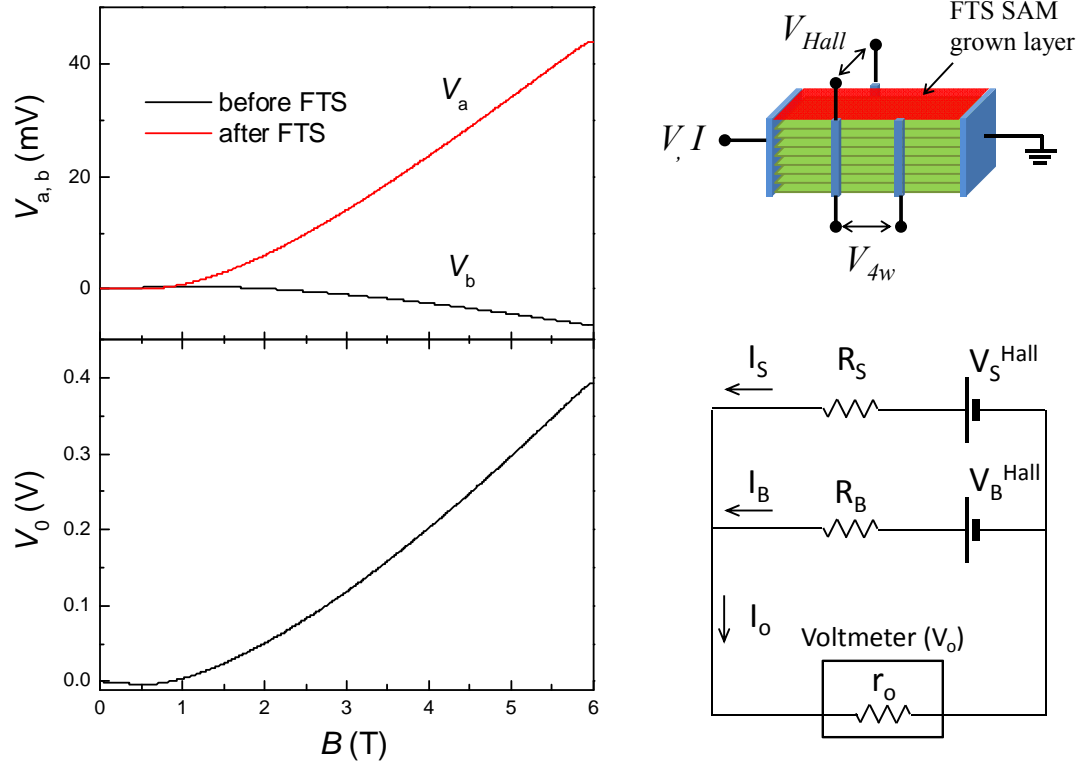


Figure 29. Hall effect measurements of graphite functionalized with an FTS SAM. (a) Hall voltage of a HOPG sample measured before (black) and after (red) FTS treatment. A clear change of sign at $B \sim 1$ T is observed. (b) Hall voltage of a SAM-doped single-layer graphite extracted from the panel (a) using Eq. (19). (c), (d) The sketch of Hall probe sample geometry and the corresponding circuit model are depicted, respectively.

To further investigate the effect of the SAM on the electronic properties of graphite, Hall effect measurements of HOPG before and after the FTS growth were carried out. Although the change in the resistance of HOPG samples is only a few percent

because of a large number of unaffected layers (Figure 26), the situation is drastically different in the Hall measurements. Figure 29(a) shows the Hall voltage measured in a typical HOPG sample. The most prominent feature was a different sign of the Hall voltage at $B > 1$ T. In addition, the magnitude of the Hall voltage became much larger after FTS treatment. A SAM-coated HOPG sample can be represented by two parts connected in parallel: a highly conductive hole-doped top layer and a bulk. As a semi-metal, pristine HOPG has a gapless multi-electronic-band structure. The sign of the Hall voltage measured in HOPG samples is determined by the relative amount of electrons and holes. At high magnetic fields, the electron and hole bands become separated by a gap of ~ 20 meV⁷⁸. As a result, transport in HOPG becomes dominated by one type of carriers that defines the sign of the Hall voltage. The sample in Figure 29(a) showed a negative Hall voltage before FTS treatment, which in our experimental setup corresponds to predominantly electron conduction. After FTS treatment, the Hall voltage became positive, indicating the addition of holes to the sample. Figure 29(c) shows a model of the Hall effect in FTS-coated HOPG: the transverse (i.e., Hall) voltages and longitudinal resistances are shown with an excitation current perpendicular to the page. The top layer, dominated by the SAM-induced holes, has a longitudinal resistance $R_S(B)$ and generates a Hall e.m.f. V_S^{Hall} , when the magnetic field is applied. The HOPG bulk has a longitudinal resistance $R_B(B)$ and a Hall e.m.f. V_B^{Hall} . The total Hall voltage after FTS coating, V_o , is a function of these four parameters. By combining the measured Hall voltages and magnetoresistance values $R_S(B)$ and $R_B(B)$ (not shown here for simplicity) before and after FTS growth, the contribution of the top (doped) layer to the Hall effect can be extracted as described as the equation (20). Based on the electric circuit corresponding to

SAM doped system shown in Figure 29(d), Kirchoff's circuit laws produce following equations.

$$I_S R_S - V_S^{Hall} - I_B R_B + V_B^{Hall} = 0 \quad (16)$$

$$I_B R_B + I_o r_o - V_B^{Hall} = 0 \quad (17)$$

$$I_o = I_S + I_B \quad (18)$$

By solving these simultaneous equations, we get

$$I_o = I_S + I_B = \frac{V_S^{Hall} - V_o}{R_S} + \frac{V_B^{Hall} - V_o}{R_B} \cong 0 \quad (19)$$

Since I_o is approximately zero due to an infinite impedance r_o in a voltmeter, the final relation for Hall voltage of the top surface layer from the bulk contribution is

$$V_S^{Hall} = V_o + (V_o - V_B^{Hall}) \cdot R_S(B) / R_B(B) \quad (20)$$

The extracted V_S^{Hall} is plotted in Figure 29(b). As expected, V_S^{Hall} had a positive sign at high magnetic fields, corresponding to hole doping. As a first approximation, the equation was applied for a conventional band-semiconductor Hall effect to the nearly linear section of $V_S^{Hall}(B)$ in Figure 29(b), $\Delta V_S^{Hall} = \Delta B \cdot I_S / (en)$, where the longitudinal current was $I_S = (W/L) \cdot \sigma_{\square} \cdot V_{SD}$ and $\sigma_{\square} = en\mu$. As a result, the hole density $n = 1.4 \times 10^{13} \text{ cm}^{-2}$ and hole mobility $\mu = 3700 \text{ cm}^2/\text{Vs}$ were obtained. Such remarkable carrier density is difficult to be achieved electrostatically in FETs.

2.3.5. FTS SAM Growth on Graphene

FTS growth and electrical measurements were also performed on single-layer graphene FETs. Graphene FETs were prepared on SiO₂/n-Si wafers using mechanical exfoliation techniques and *e*-beam lithography (the details can be found elsewhere⁷⁹). Several samples were studied and showed similar results. The transconductance of graphene FETs, $\sigma(V_g)$, was monitored *in situ*, as FTS SAM was growing on the surface of the sample (Figure 30). There are several important observations: (1) the initial Dirac point of pristine graphene is at $V_g = 15$ V, but shifts to more positive V_g as the SAM is growing and eventually goes beyond the experimentally accessible range of gate voltages; (2) away from the Dirac point, the conductivity shows a sublinear increase with V_g both for pristine and briefly treated samples (≤ 15 min), but becomes linear for a saturated monolayer SAM coverage (longer treatments); and (3) the conductivity of graphene increases with FTS growth, while the field-effect mobility decreases.

A non-zero V_g of the Dirac point in as-prepared graphene is usually understood in terms of unintentional doping by species absorbed from the ambient^{80,81}. As the FTS SAM is grown on graphene, the Dirac point was shifted toward more positive V_g , indicating that the holes were induced in the sample at a density $\Delta n = \gamma \cdot \Delta V_g^{\text{Dirac}}$, with $\gamma = 7.2 \times 10^{10} \text{ cm}^{-2} \text{ V}^{-1}$. For a complete SAM (red curve in Figure 30), the position of the Dirac point was estimated by extrapolating the experimentally accessible linear portion of the curve to a minimum conductivity of $\sim 7 e^2/h$, leading to a density of SAM-induced holes, $\Delta n \approx 1.2 \times 10^{13} \text{ cm}^{-2}$, close to the value obtained from our Hall effect measurements.

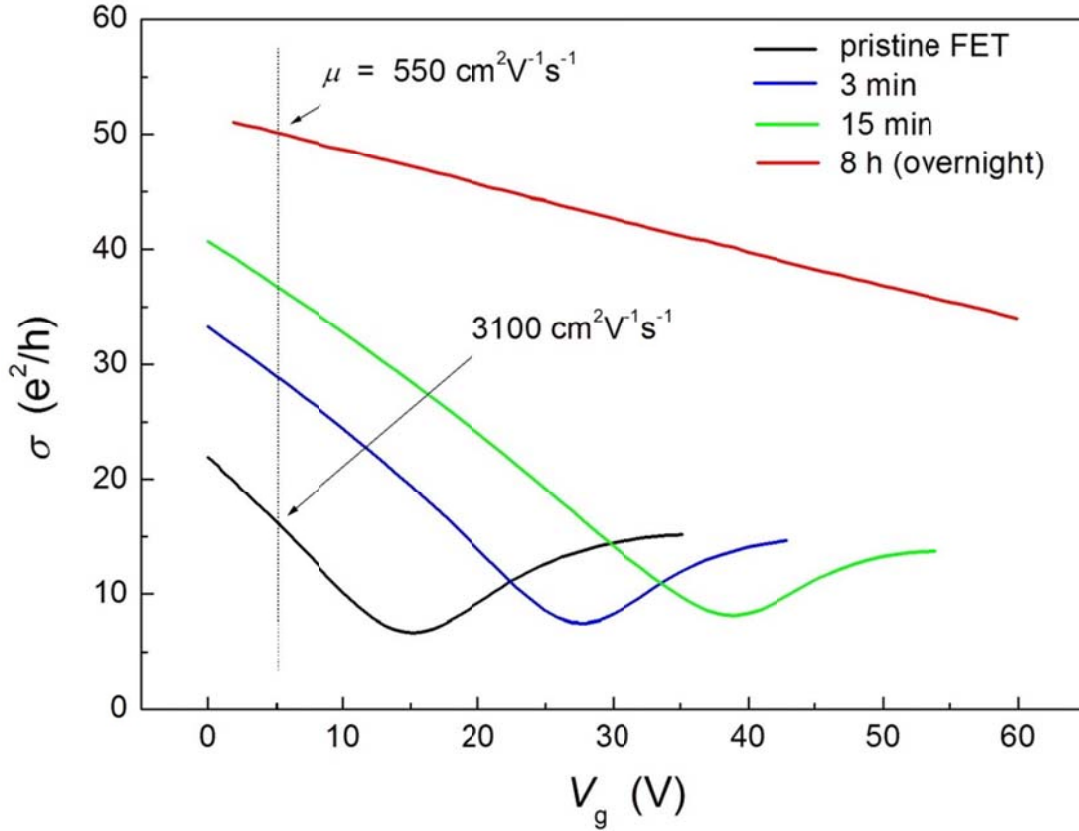


Figure 30. Evolution of transconductance characteristics, $\sigma(V_g)$, of a graphene FET measured in-situ as an FTS SAM grows on a graphene surface. The data have been collected at different growth times: 0 (pristine graphene), 3 min, 15 min and 8 h. Mobility of the pristine graphene FET and the same device treated overnight are $3100 \text{ cm}^2 \text{V}^{-1} \text{s}^{-1}$ and $550 \text{ cm}^2 \text{V}^{-1} \text{s}^{-1}$, respectively (calculated at $V_g = 5 \text{ V}$).

Observations (2) and (3) above can be explained by the model of long-range Coulomb scattering due to charged impurities, in which long-range scattering leads to a linear dependence of σ on carrier density, whereas short-range scattering results in a sublinear dependence⁸²⁻⁸⁴. FTS extracts electrons from graphene, which converts SAM

molecules into negatively charged static centers interacting with mobile holes through a long-range Coulomb interaction. Correspondingly, in Figure 30, the $\sigma(n)$ dependence changes from sublinear to linear with μ decreasing, as more and more SAM molecules are introduced onto the surface, and the dominant scattering mechanism becomes long-range Coulomb interactions with charged impurities. The theory of long-range scattering in graphene also shows that mobility is inversely proportional to the density of scattering centers: $\mu = 1.1 \times 10^{15} \cdot \epsilon / n_{\text{imp}}$, where ϵ is the dielectric constant of the material that contains scattering centers⁸³ (ϵ of an FTS monolayer is estimated to be ~ 3.5 ⁸⁵). Combining these results, the density of SAM-related scattering centers for a complete monolayer on graphene can be estimated: $n_{\text{imp}} = 0.67 \times 10^{13} \text{ cm}^{-2}$, i.e., about 50% of the density of SAM-induced holes. This result is not unexpected, since the FTS SAM is a dense cross-linked layer, and FTS molecules may not necessarily be treated as independent scattering objects.

After initial measurements, the graphene-FTS samples were left in atmosphere for more than one week and measured again. The FTS-induced conductivity only decreased by less than 10% compared to the result obtained on freshly coated samples while still in vacuum. Another test was annealing graphene-FTS samples in forming gas at 120 °C. The FTS-induced conductivity survived such heating, indicating the SAM layer is very stable even at elevated temperatures.

There is a qualitative agreement between our results on HOPG and graphene-FETs: in both cases a strong *p*-type doping with a large carrier density has been observed. The quantitative differences in the SAM-induced single-layer σ in these cases might arise from: (a) different band structures of an isolated graphene and multilayered graphite, (b)

different relative weights of various scattering mechanisms, and (c) an extra scattering in graphene FETs caused by the underlying SiO₂.

It's worth noting that our observation of SAM decoration of graphene edges (Figure 27(b)) confirms the hypothesis of edge termination with oxygen species⁸⁶. Indeed, according to the trichlorosilane chemistry on SiO₂, such groups as hydroxyl (OH) or carboxyl (COOH) are necessary for the SAM molecules to covalently bond to the surface⁸⁷. Our observation suggests that the mechanism of SAM formation on graphene is based on a defect-mediated nucleation, followed by a lateral 2D polymerization that eventually leads complete monolayer coverage by a cross-linked and robust 2D siloxane network (model in Figure 28). As opposed to doping by electropositive atoms such as alkali ions⁸³, SAM doping of graphene exhibits an excellent stability in ambient and high-vacuum environments. The distinct morphology of SAM nucleation suggests that it can be used as a simple technique for visualization or electronic passivation of graphene edges and defects, as well as for complete SAM coverage.

2.4. Growth of Alkyl-silane SAMs on Carbon Nanotubes (CNTs)

Devices based on carbon nanotubes have been proposed for many potential applications, such as chemical and optical sensors⁸⁸⁻⁹⁰, transparent conductive electrodes for photovoltaic devices⁹¹, as well as CNT field effect transistors⁹²⁻⁹⁶. A method recently developed by Zhang *et al*⁹⁷. provides a way of fabricating macroscopic, free-standing, transparent and partially aligned CNT sheets, which might open new technological possibilities in low-cost flexible electronics. In spite of the progress in the development

of CNT conductors, the conductivity of these systems is still not sufficient to compete with transparent conducting oxides for applications in transparent electronics. This is mainly due to two factors: the relatively large fraction of semiconducting nanotubes in CNT sheets and a high resistance associated with interconnects between the individual tubes in a random CNT network. Strategies to improve the conductivity include an enrichment of CNT sheets with longer and more oriented individual nanotubes (thus reducing the problem of interconnecting junctions), as well as increasing the fraction of metallic tubes in the CNT samples. Here, an alternative approach for improving electrical conductivity of CNT layers is proposed. In this thesis, the growth of FTS SAM on carbon nanotubes and their effect on the electronic properties of CNT sheets is reported.

2.4.1. CNTs Field-effect Transistor with Parylene Gate Dielectric

Partially aligned and densified multi-walled carbon nanotube (MWNT) sheets have been prepared on glass substrates. These nanotubes were fabricated at The University of Texas at Dallas in a CVD process as described in Ref... Orientation of the MWNT bundles is defined by the fabrication process, in which quasi two dimensional networks with a preferential MWNT alignment is formed over macroscopically large area. These strong MWNT sheets are semi-transparent (transmission in the visible range of spectrum $\sim 75\%$) and mainly consist of multi-walled metallic nanotube bundles, which makes the sheet resistivity of the pristine (undoped) samples around $\square = 900 \square/\square$. Electrical contacts have been prepared by depositing an aqueous suspension of colloidal graphite (Aquadag® E Colloidal Graphite, Ted Pella, Inc., product #16051) on these

MWCNT sheets, defining the channel length, $L = 7$ mm, and width, $W = 5$ mm, with the channel orientation along the MWNT alignment.

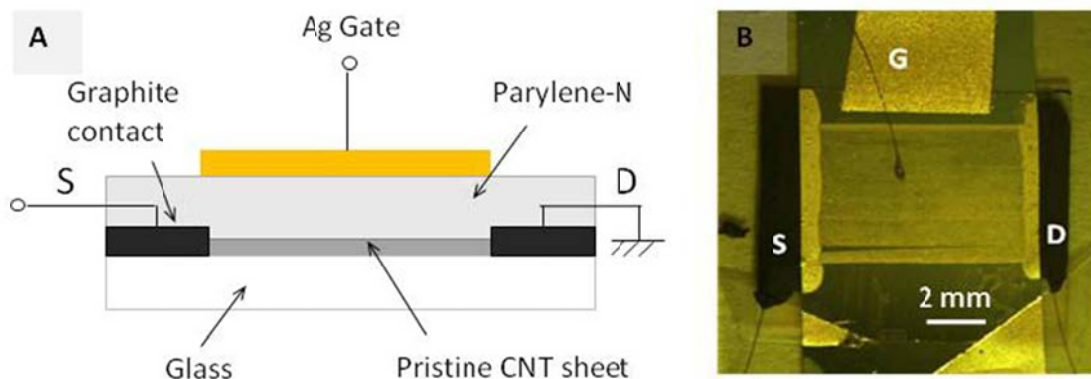


Figure 31. (a) Schematic of CNT-FET. Colloidal graphite paint was used as source-drain contacts. 2 μm -thick parylene-*N* dielectric layer ($\epsilon = 2.6$) and a 30 nm-thick silver film were deposited on the CNT sheet. (b) The “top-view” photograph of an actual large-area CNT-FET device. The partially aligned CNT array is clearly visible through the gate.

Top gated field-effect transistors (CNT-FETs) have been fabricated by depositing 2 μm thick parylene-*N* insulating film onto these MWNT samples with contacts, topped with a thermally evaporated 30 nm-thick silver gate (Figure 31(a)). Figure 31(b) shows a photograph of one of the devices. It is very exciting that the parylene technique also works very well for fabrication of FETs on large-area CNT sheets, even though these samples possess very rough nanoscale morphology due to a network of nanotube bundles.

This has been demonstrated in this work by fabrication of top-gate CNT-FETs with a negligible gate leakage.

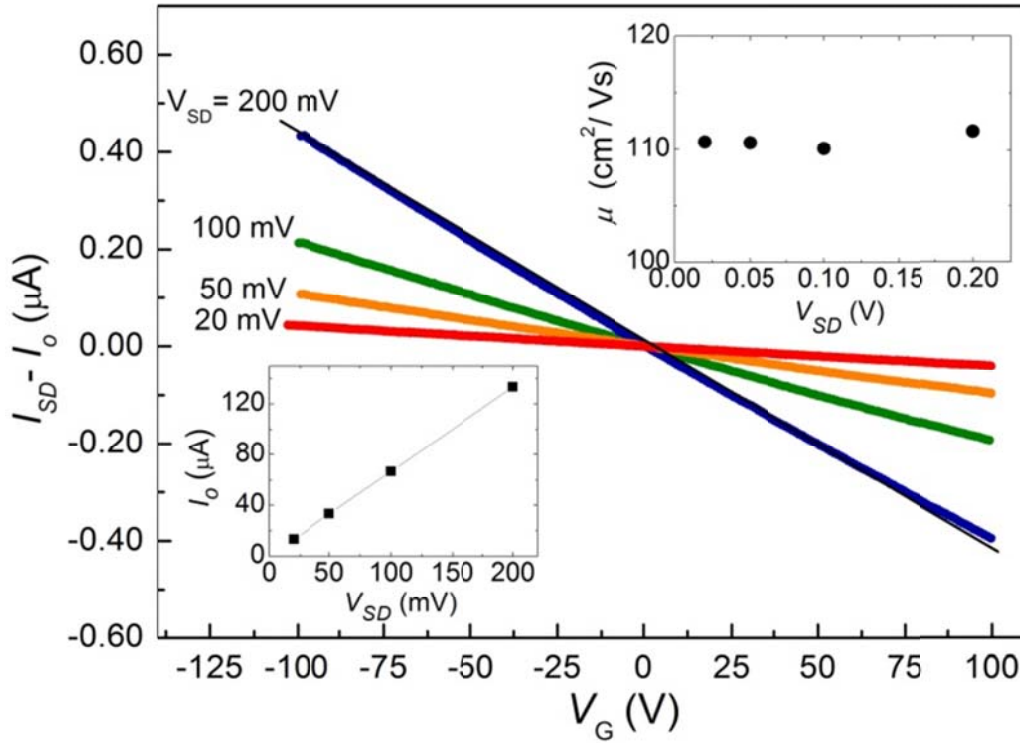


Figure 32. Transfer characteristics of CNT-FET: I_{SD} (V_G). For clarity, the source-drain current at $V_G = 0$, I_0 , has been subtracted from the corresponding curves. Lower inset: I_0 as a function of V_{SD} that shows an ohmic relation and corresponds to a resistivity of 1000 \square/\square . Upper inset: extracted field-effect mobility \square as a function of V_{SD} .

The characteristics of a typical CNT-FET at room temperature are shown in Figure 32. The source-drain current, I_{SD} , was measured as a function of the gate voltage, V_G , at different values of the source-drain voltage, V_{SD} . Since the current at zero V_G , I_0 , can have very different values (as shown in the lower inset of Figure 32) for the different

V_{SD} , $I_0(V_{SD})$ were subtracted from the corresponding $I_{SD}(V_G)$ curves for clarity. The transfer curves in the main panel show a typical p -type behavior with a large depletion gate voltage, which is expected for such a highly conductive material. The field-effect mobility, μ , can be estimated from the slope of $I_{SD}(V_G)$ dependence using the trans-conductance equation:

$$\mu = L \cdot |\partial I_{SD} / \partial V_G| / (C_i \cdot V_{SD} \cdot W), \quad (21)$$

where $C_i = 1.1 \text{ nF/cm}^2$ is the gate-channel capacitance per unit area. The determination of a correct channel width W represents a more complicated problem. One can use as-measured macroscopic sample dimensions for W and L . However, this is equivalent to treating the sample as a homogeneous two dimensional conductor, completely ignoring the sparse network morphology of these samples. A better approximation is to consider the sample as an inhomogeneous 2D conductor consisting of an ensemble of equally spaced 1D bundles connecting the source and drain contacts. In that case, the width W needs to be replaced by some effective width W_{eff} to account for the empty spaces between the bundles. For that purpose, an optical transmission measurement of the CNT sheets was performed, in which our samples were $\sim 75\%$ transparent, suggesting that only $\sim 25\%$ of the whole area of the sample is actually covered by the CNT bundles. Therefore, W_{eff} was taken to be 25% of the as-measured macroscopic channel width W . With such a correction, the mobility using the data in the main panel of Figure 32 is extracted, as plotted in the upper inset. Throughout the whole V_{SD} range tested, the mobility was almost a constant around $110 \text{ cm}^2 \cdot \text{V}^{-1} \cdot \text{s}^{-1}$. Another interesting fact is that there is no hysteresis observed in our CNT-FETs, which is rarely the case for individual CNT samples⁹⁸⁻¹⁰⁰.

2.4.2. Electrical Modification of CNTs by FTS SAM Growth

Next, the effect of FTS treatment on the electrical properties of the MWNT sheets is studied. Samples were loaded into a chamber and their two probe resistance was monitored *in situ* during the FTS growth process. Samples were then exposed to a saturated FTS vapor. Typical results are shown in Figure 33(a). Conductivity of this sample increased by 60% percent during a course of 5 hours, and exhibited the saturation after an overnight treatment. Qualitatively, the increase in conductivity of MWNT sheets upon FTS treatment is similar to the results obtained on other carbon based materials, such as rubrene, graphene, and certain types of polymers. In all cases, the protonic doping by silanol groups of hydrolyzed FTS molecules is believed to introduce mobile carriers into the material under test, leading to a conductivity increase. Quantitatively, however, the effect of FTS treatment is less prominent for these MWNT sheets as compared with other systems which usually have a change from one to a few orders of magnitude. This is not surprising, because the pristine MWNT sheets used in our study are already highly conductive. In particular, the FTS doping effect on metallic nanotubes should be negligible given their high carrier density, while the effect on pure semiconducting tubes should be very large. Indeed, using single walled carbon nanotube (SWNT) sheets, in which statistically there must be 1/3 metallic and 2/3 semiconducting tubes, a factor of 4 increase in conductivity was observed with FTS treatment.

Carrier concentration of the MWNT sheets can be estimated using the relation $\sigma = ne\mu$. Before FTS treatment, with the extracted mobility of $110 \text{ cm}^2 \cdot \text{V}^{-1} \cdot \text{s}^{-1}$, n is $2.6 \times 10^{14} \text{ cm}^{-2}$. Assuming that mobility does not change with FTS treatment, the FTS-induced

carrier concentration was estimated to be $\Delta n = 1.6 \times 10^{14} \text{ cm}^{-2}$, since the conductivity increased by 60%. Such doping level is higher than that obtained in other carbon based system (usually around $\sim 10^{13} \text{ cm}^{-2}$)^{13,14,16}. This difference might have a few origins. Due to its quasi 2D network nature, neither the estimation of the mobility as discussed earlier, nor the applicability of the relation $\sigma = ne\mu$ is as unambiguous as in a standard 2D system. In addition, due to the unique geometry of nanotubes, the mechanism of FTS growth on CNT surface and the interface morphology may be different from those in a standard 2D system, particularly when one considers the significantly greater surface area available to SAM growth and therefore doping. It is also noted that CNT layers used in this experiment had a finite thickness (usually larger than one bundle diameter), and hence obtained sheet conductivities were projected values. These issues remain open for future exploration.

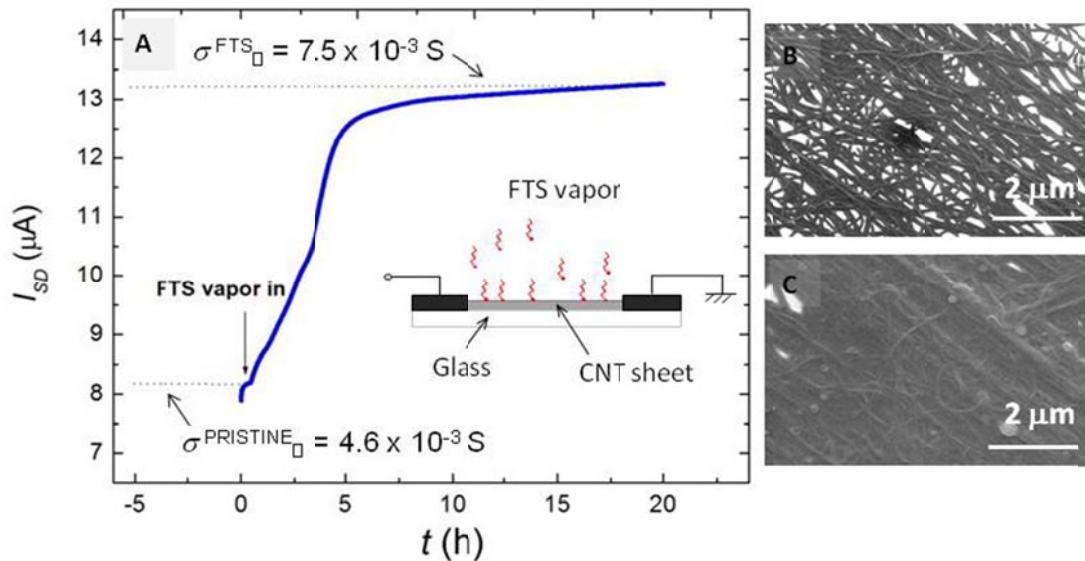


Figure 33. (a) The source-drain current flowing through a CNT sheet (not a transistor device) as a function of time during FTS treatment ($V_{SD} = 10$ mV). The vertical arrow indicates the moment when FTS vapor was introduced into the deposition chamber. Both $\sigma^{PRISTINE}_{\square}$ and σ^{FTS}_{\square} are adjusted values using the effective width W_{eff} as discussed in the text. The inset depicts the deposition of FTS molecules onto a CNT sample. (b) and (c) are scanning electron microscope images of a CNT sample before and after the deposition of FTS: clear changes in the contrast can be seen.

Figure 33(b) and (c) are scanning electron microscope images of pristine and FTS-coated MWNT sheets, respectively. The bright areas in Figure 33(b) are the voids, through which an insulating glass substrate is seen. MWNT bundles are clearly visible due to a significant difference between the conductivity of the bundles and that of the glass. After FTS treatment, however, the contrast became much lower, since now both the glass and the surface of the nanotubes were covered with the insulating layer of FTS SAM. These images offer an independent evidence of the effective coating of the nanotubes by FTS molecules. It is also noted that there was no noticeable change in color or transparency of the nanotube sheets with FTS treatment.

Finally, the FTS doping effect is stable in vacuum or in non-polar gases. In prolonged measurements after the FTS deposition, no significant changes in conductivity have been observed. Some of the FTS doped samples have been stored in a sealed vacuum plastic package for about one year, after which repeated measurements indicated that conductivity has dropped only by 15%.

Chapter IV

Conclusion

As the first part of this thesis, high performance organic field-effect transistors (OFETs) are fabricated. Two types of OFETs, *parylene* insulating polymer dielectric OFET and *air-gap* PDMS stamp OFET are employed to study the charge transport for organic single crystals. Strain- and defect-free interface between parylene dielectric film and the organic semiconductor channel in OFETs enables us to investigate bias-stress instability in OFETs based on rubrene, tetracene, and TIPS-pentacene single crystals interfaced with the amorphous polymer insulator. A combination of the charge transport and UPS measurements suggests that the effect is due to the transfer of holes from the accumulation channel of the semiconductor to the localized states of the insulator. The effect is smaller in systems with the greater energetic mismatch between the HOMO edges of the semiconductor and the insulator. The model only relies on the concepts of semiconductor's ionization energy and exponential band tails of disordered insulators, and hence it could be used to understand instabilities in a wider range of semiconductor devices, including organic, inorganic, CNT and graphene FETs.

In addition, field-effect transistors (bottom-gate and bottom-contacts geometry) on multi-walled carbon nanotube (MWNT) sheets using parylene gate dielectric are successfully fabricated. Based on the transconductance characteristics in the field-effect, the mobility and the density of charge carriers of pristine MWNT sheets are estimated to be $110 \text{ cm}^2 \cdot \text{V}^{-1} \cdot \text{s}^{-1}$ and $2.6 \times 10^{14} \text{ cm}^{-2}$, respectively.

As the second part, it is reported that various organic and other carbon-based materials can be functionalized by the growth of alkyl-silane SAMs. AFM, SEM and C-AFM techniques are employed to reveal the microscopic mechanism of SAM nucleation

and growth process on the organic crystals surface. In the early growth stage, SAM nucleation occurs mostly at the molecular step edges or defect sites on the surface of substrates. A consecutive growth proceeds laterally by cross-linking between SAM molecules and in-plane polymerization eventually forms monolayer on the surface of the substrates. By coating the surface of *p*-type organic semiconductors by SAMs, a strong enhancement of surface conductivity is observed. This hole-doping effect is explained by interfacial charge transfer (chemical doping) occurred during the SAM formation. Conducting AFM (C-AFM) measurements show that in the very early stage of SAM growth, the molecular steps at the surface of organic crystals can be readily functionalized with silane SAMs, in which the conducting paths are formed along the molecular step edges of rubrene surface with nanoscale channel width. This phenomenon is interesting from several perspectives: a) visualization of molecular steps and oxygen-containing defects at the surface of organic semiconductors; b) studies of charge transport in individual crystalline organic quasi-1D conducting channels; and c) passivation and selective doping of scattering sites and traps associated with molecular steps, grain boundaries and oxygen defects for an enhanced charge transport in OFETs: The impact of these extrinsic scattering and trapping processes can be reduced or eliminated by selectively doping on the aforementioned defects with a SAM, which can result in a better understanding of charge transport in organic semiconductors.

The interaction of ultrathin films of polythiophenes (P3HT, PBTTT) conjugated organic polymers with the vapors of hydrolyzed FTS SAM is demonstrated, which results in a drastic increase of the electrical conductivity and a strong suppression of interband optical absorption of these polymers. Upon doping with FTS SAM, the electrical

conductivity increases by up to six orders of magnitude, reaching $(1.1 \pm 0.1) \times 10^3 \Omega^{-1}\text{cm}^{-1}$ in PBTTT and $50 \pm 20 \Omega^{-1}\text{cm}^{-1}$ in P3HT known as a record high conductivity in doped polymers. The effect is tentatively attributed to protonic doping of the polymer chains by silanol groups of hydrolyzed trichlorosilanes available within the partially polymerized siloxane network. The doped polymer films exhibit a very good stability in high vacuum and nonpolar gases. However, when they are exposed to polar vapors, they show an interesting electrical switching effect; Sensing and dedoping effect. These effects lead to an attractive new route of doping of conjugated polymers that may be interesting for applications in molecular sensors, transparent conductors and organic electronics.

The stable self-assembled monolayers of fluoroalkyl silanes at the surface of carbon-based materials such as graphite, graphene and carbon nanotubes (CNTs) are also synthesized. A strong surface doping effect of graphene and CNTs with the carrier densities in excess of the order of 10^{13} cm^{-2} and 10^{14} cm^{-2} is observed, respectively. Interestingly, Hall measurements demonstrate that FTS SAM growth only on the top layer of graphite changes Hall voltage from negative to positive, which is indicative of a strong hole-doping on the graphite surface. AFM and SEM studies confirm that SAM nucleation and growth process on graphite are very similar as those on organic single crystals: SAM nucleation occurs on defect sites or graphene steps and the consecutive lateral growth proceeds to the entire surface by cross-linking of SAM molecules. X-ray photoelectron spectroscopy (XPS) confirmed the simple monolayer structure with the predicted stoichiometry of FTS growth on graphite. The novel doping approach described here offers the potential application for the chemical modification of graphene or CNT electronic properties using methods of molecular engineering and self assembly.

References

- 1 Najafov, H., Lee, B., Zhou, Q., Feldman, L. C. & Podzorov, V. Observation of long-range exciton diffusion in highly ordered organic semiconductors. *Nat Mater* **9**, 938-943, doi:Doi 10.1038/Nmat2872 (2010).
- 2 Love, J. C., Estroff, L. A., Kriebel, J. K., Nuzzo, R. G. & Whitesides, G. M. Self-assembled monolayers of thiolates on metals as a form of nanotechnology. *Chem. Rev.* **105**, 1103-1170 (2005).
- 3 Campbell, I. H. Controlling charge injection in organic electronic devices using self-assembled monolayers. *Appl. Phys. Lett.* **71**, 3528-3530 (1997).
- 4 Gundlach, D. J., Jia, L. & Jackson, T. N. Pentacene TFT with improved linear region characteristics using chemically modified source and drain electrodes. *IEEE Electron. Dev. Lett.* **22**, 571-573 (2001).
- 5 Akkerman, H. B., Blom, P. W. M., de Leeuw, D. M. & de Boer, B. Towards molecular electronics with large-area molecular junctions. *Nature* **441**, 69-72 (2006).
- 6 Heimel, G., Romaner, L., Bredas, J. L. & Zojer, E. Interface energetics and level alignment at covalent metal-molecule junctions: [pi]-conjugated thiols on gold. *Phys. Rev. Lett.* **96**, 196806 (2006).
- 7 Briseno, A. L. Patterning organic single-crystal transistor arrays. *Nature* **444**, 913-917 (2006).
- 8 Kobayashi, S. Control of carrier density by self-assembled monolayers in organic field-effect transistors. *Nature Mater.* **3**, 317-322 (2004).
- 9 Takeya, J. Effect of polarized organosilane self-assembled monolayers on organic single-crystal field-effect transistors. *Appl. Phys. Lett.* **85**, 5078-5080 (2004).
- 10 Pernstich, K. P. Threshold voltage shift in organic field effect transistors by dipole monolayers on the gate insulator. *J. Appl. Phys.* **96**, 6431-6438 (2004).
- 11 Facchetti, A., Yoon, M. H. & Marks, T. J. Gate dielectrics for organic field-effect transistors: new opportunities for organic electronics. *Adv. Mater.* **17**, 1705-1725 (2005).
- 12 Chua, L. L. General observation of n-type field-effect behaviour in organic semiconductors. *Nature* **434**, 194-199 (2005).
- 13 Calhoun, M. F., Sanchez, J., Olaya, D., Gershenson, M. E. & Podzorov, V. Electronic functionalization of the surface of organic semiconductors with self-assembled monolayers. *Nat Mater* **7**, 84-89, doi:Doi 10.1038/Nmat2059 (2008).
- 14 Khatib, O. *et al.* Infrared signatures of high carrier densities induced in semiconducting poly(3-hexylthiophene) by fluorinated organosilane molecules (vol 107, 123702, 2010). *J Appl Phys* **108**, doi:Artn 039903 Doi 10.1063/1.3467784 (2010).
- 15 Lee, B. C., A. Zakhidov, A. Podzorov, V. Stable doping of carbon nanotubes with fluoroalkyl silane self-assembled molecules.
- 16 Kao, C. Y. *et al.* Doping of Conjugated Polythiophenes with Alky Silanes. *Adv Funct Mater* **19**, 1906-1911, doi:DOI 10.1002/adfm.200900120 (2009).
- 17 Lee, B., Choi, T., Cheong, S. W. & Podzorov, V. Nanoscale Conducting Channels at the Surface of Organic Semiconductors Formed by Decoration of Molecular

- Steps with Self-Assembled Molecules. *Adv Funct Mater* **19**, 3726-3730, doi:DOI 10.1002/adfm.200901525 (2009).
- 18 Laudise, R. A., Kloc, C., Simpkins, P. G. & Siegrist, T. Physical vapor growth of organic semiconductors. *J Cryst Growth* **187**, 449-454 (1998).
 - 19 Bao, Z. & Locklin, J. J. *Organic field-effect transistors*. Vol. 128 (CRC, 2007).
 - 20 <http://en.wikipedia.org/wiki/Parylene>.
 - 21 Podzorov, V., Pudalov, V. M. & Gershenson, M. E. Field-effect transistors on rubrene single crystals with parylene gate insulator. *Appl. Phys. Lett.* **82**, 1739-1741 (2003).
 - 22 Sze, S. M. *Semiconductor devices: physics and technology*. (John Wiley & Sons, 2008).
 - 23 Braga, D. & Horowitz, G. High-Performance Organic Field-Effect Transistors. *Adv Mater* **21**, 1473-1486, doi:DOI 10.1002/adma.200802733 (2009).
 - 24 Singh, T. B. & Sariciftci, N. S. Progress in plastic electronics devices. *Annu Rev Mater Res* **36**, 199-230, doi:DOI 10.1146/annurev.matsci.36.022805.094757 (2006).
 - 25 Horowitz, G. Organic field-effect transistors. *Adv Mater* **10**, 365-377 (1998).
 - 26 Ahn, C. H. *et al.* Electrostatic modification of novel materials. *Rev Mod Phys* **78**, 1185-1212, doi:DOI 10.1103/RevModPhys.78.1185 (2006).
 - 27 Menard, E. *et al.* High-performance n- and p-type single-crystal organic transistors with free-space gate dielectrics. *Adv Mater* **16**, 2097-+, doi:DOI 10.1002/adma.200401017 (2004).
 - 28 Podzorov, V., Sysoev, S. E., Loginova, E., Pudalov, V. M. & Gershenson, M. E. Single-crystal organic field effect transistors with the hole mobility similar to 8 cm²/V s. *Appl Phys Lett* **83**, 3504-3506, doi:Doi 10.1063/1.1622799 (2003).
 - 29 Sirringhaus, H. Device physics of Solution-processed organic field-effect transistors. *Adv Mater* **17**, 2411-2425, doi:DOI 10.1002/adma.200501152 (2005).
 - 30 Podzorov, V., Menard, E., Rogers, J. A. & Gershenson, M. E. Hall effect in the accumulation layers on the surface of organic semiconductors. *Phys Rev Lett* **95**, doi:Artn 226601 Doi 10.1103/Physrevlett.95.226601 (2005).
 - 31 Podzorov, V. *et al.* Intrinsic charge transport on the surface of organic semiconductors. *Phys Rev Lett* **93**, doi:Artn 086602, Doi 10.1103/Physrevlett.93.086602 (2004).
 - 32 Sirringhaus, H. Reliability of Organic Field-Effect Transistors. *Adv Mater* **21**, 3859-3873, doi:DOI 10.1002/adma.200901136 (2009).
 - 33 Hulea, I. N. *et al.* Tunable Frohlich polarons in organic single-crystal transistors. *Nat Mater* **5**, 982-986, doi:Doi 10.1038/Nmat1774 (2006).
 - 34 Podzorov, V., Pudalov, V. M. & Gershenson, M. E. Light-induced switching in back-gated organic transistors with built-in conduction channel. *Appl Phys Lett* **85**, 6039-6041, doi:Doi 10.1063/1.1836877 (2004).
 - 35 Li, Z. Q. *et al.* Light quasiparticles dominate electronic transport in molecular crystal field-effect transistors. *Phys Rev Lett* **99**, doi:Artn 016403, Doi 10.1103/Physrevlett.99.016403 (2007).
 - 36 Sundar, V. C. *et al.* Elastomeric transistor stamps: Reversible probing of charge transport in organic crystals. *Science* **303**, 1644-1646 (2004).

- 37 Cahen, D. & Kahn, A. Electron energetics at surfaces and interfaces: Concepts and experiments. *Adv Mater* **15**, 271-277 (2003).
- 38 Puntambekar, K., Dong, J. P., Haugstad, G. & Frisbie, C. D. Structural and electrostatic complexity at a pentacene/insulator interface. *Adv Funct Mater* **16**, 879-884, doi:DOI 10.1002/adfm.200500816 (2006).
- 39 de Boer, R. W. I., Gershenson, M. E., Morpurgo, A. F. & Podzorov, V. Organic single-crystal field-effect transistors. *Phys. Status Solidi* **201**, 1302-1331 (2004).
- 40 Takeya, J. *et al.* Effects of polarized organosilane self-assembled monolayers on organic single-crystal field-effect transistors. *Appl Phys Lett* **85**, 5078-5080, doi:Doi 10.1063/1.1826239 (2004).
- 41 Briseno, A. L. *et al.* High-performance organic single-crystal transistors on flexible substrates. *Adv Mater* **18**, 2320+, doi:DOI 10.1002/adma.200600634 (2006).
- 42 Calhoun, M. F., Hsieh, C. & Podzorov, V. Effect of interfacial shallow traps on polaron transport at the surface of organic semiconductors. *Phys Rev Lett* **98**, doi:Artn 096402, Doi 10.1103/Physrevlett.98.096402 (2007).
- 43 Park, J. G., Vasic, R., Brooks, J. S. & Anthony, J. E. Characterization of functionalized pentacene field-effect transistors and its logic gate application. *J Appl Phys* **100**, doi:Artn 044511, Doi 10.1063/1.2335378 (2006).
- 44 Subramanian, S. *et al.* Chromophore fluorination enhances crystallization and stability of soluble anthradithiophene semiconductors. *J Am Chem Soc* **130**, 2706+, doi:Doi 10.1021/Ja073235k (2008).
- 45 Jackson, W. B., Marshall, J. M. & Moyer, M. D. Role of Hydrogen in the Formation of Metastable Defects in Hydrogenated Amorphous-Silicon. *Phys Rev B* **39**, 1164-1179 (1989).
- 46 Gartstein, Y. N. & Conwell, E. M. High-Field Hopping Mobility in Molecular-Systems with Spatially Correlated Energetic Disorder. *Chem Phys Lett* **245**, 351-358 (1995).
- 47 Monroe, D. Hopping in Exponential Band Tails. *Phys Rev Lett* **54**, 146-149 (1985).
- 48 Kahn, A., Koch, N. & Gao, W. Electronic structure and electrical properties of interfaces between metals and π -conjugated molecular films. *Journal of Polymer Science Part B: Polymer Physics* **41**, 2529-2548, doi:10.1002/polb.10642 (2003).
- 49 Gelest brochure : "Hydrophobicity, h. a. s. s. m., www.gelest.com.
- 50 Sagiv, J. Monolayer Chemistry with Self-Assembling Monolayers. *Abstr Pap Am Chem S* **188**, 83-Coll (1984).
- 51 Menard, E. *et al.* Nanoscale surface morphology and rectifying behavior of a bulk single-crystal organic semiconductor. *Adv Mater* **18**, 1552+, doi:DOI 10.1002/adma.200502569 (2006).
- 52 Tsetseris, L. & Pantelides, S. T. Large impurity effects in rubrene crystals: First-principles calculations. *Phys Rev B* **78**, doi:Artn 115205, Doi 10.1103/Physrevb.78.115205 (2008).
- 53 Tsetseris, L. & Pantelides, S. T. Modification of the electronic properties of rubrene crystals by water and oxygen-related species. *Org Electron* **10**, 333-340, doi:DOI 10.1016/j.orgel.2008.12.009 (2009).

- 54 Hwang, J., Wan, A. & Kahn, A. Energetics of metal-organic interfaces: New experiments and assessment of the field. *Mat Sci Eng R* **64**, 1-31, doi:DOI 10.1016/j.mser.2008.12.001 (2009).
- 55 Reese, C. & Bao, Z. High-resolution measurement of the anisotropy of charge transport in single crystals. *Adv Mater* **19**, 4535-+, doi:DOI 10.1002/adma.200701139 (2007).
- 56 Zeis, R. *et al.* Field effect studies on rubrene and impurities of rubrene. *Chem Mater* **18**, 244-248, doi:Doi 10.1021/Cm0502626 (2006).
- 57 Heeger, A. J. Semiconducting and metallic polymers: the fourth generation of polymeric materials. *Synthetic Met* **125**, 23-42 (2001).
- 58 McCullough, R. D. The chemistry of conducting polythiophenes. *Adv Mater* **10**, 93-+ (1998).
- 59 Epstein, A. J. & Yang, Y. Polymeric and organic electronic materials: From scientific curiosity to applications. *Mrs Bull* **22**, 13-14 (1997).
- 60 Heeger, A. J. Semiconducting and metallic polymers: The fourth generation of polymeric materials (Nobel lecture). *Angew Chem Int Edit* **40**, 2591-2611 (2001).
- 61 Chung, T. C., Kaufman, J. H., Heeger, A. J. & Wudl, F. Charge Storage in Doped Poly(Thiophene) - Optical and Electrochemical Studies. *Phys Rev B* **30**, 702-710 (1984).
- 62 Wang, Y. L. & Lieberman, M. Growth of ultrasmooth octadecyltrichlorosilane self-assembled monolayers on SiO₂. *Langmuir* **19**, 1159-1167, doi:Doi 10.1021/La020697x (2003).
- 63 Wasserman, S. R., Tao, Y. T. & Whitesides, G. M. Structure and Reactivity of Alkylsiloxane Monolayers Formed by Reaction of Alkyltrichlorosilanes on Silicon Substrates. *Langmuir* **5**, 1074-1087 (1989).
- 64 Tripp, C. P. & Hair, M. L. An Infrared Study of the Reaction of Octadecyltrichlorosilane with Silica. *Langmuir* **8**, 1120-1126 (1992).
- 65 Chabiny, M. L., Street, R. A. & Northrup, J. E. Effects of molecular oxygen and ozone on polythiophene-based thin-film transistors. *Appl Phys Lett* **90**, doi:Artn 123508, Doi 10.1063/1.2715445 (2007).
- 66 McCulloch, I. Liquid-crystalline semiconducting polymers with high charge-carrier mobility. *Nature Mater.* **5**, 328-333 (2006).
- 67 Salleo, A. Charge transport in polymeric transistors. *Mater Today* **10**, 38-45 (2007).
- 68 Zhang, R. *et al.* Nanostructure dependence of field-effect mobility in regioregular poly(3-hexylthiophene) thin film field effect transistors. *J Am Chem Soc* **128**, 3480-3481, doi:Doi 10.1021/Ja055192i (2006).
- 69 Sirringhaus, H. *et al.* Two-dimensional charge transport in self-organized, high-mobility conjugated polymers. *Nature* **401**, 685-688 (1999).
- 70 Panzer, M. J. & Frisbie, C. D. High carrier density and metallic conductivity in poly(3-hexylthiophene) achieved by electrostatic charge injection. *Adv Funct Mater* **16**, 1051-1056, doi:DOI 10.1002/adfm.200600111 (2006).
- 71 Kim, Y. H., Spiegel, D., Hotta, S. & Heeger, A. J. Photoexcitation and Doping Studies of Poly(3-Hexylthienylene). *Phys Rev B* **38**, 5490-5495 (1988).
- 72 Macdiarmid, A. G. & Epstein, A. J. Secondary Doping in Polyaniline. *Synthetic Met* **69**, 85-92 (1995).

- 73 Yoo, J. E. *et al.* Improving the electrical conductivity of polymer acid-doped polyaniline by controlling the template molecular weight. *J Mater Chem* **17**, 1268-1275, doi:Doi 10.1039/B618521e (2007).
- 74 Logdlund, M., Lazzaroni, R., Stafstrom, S., Salaneck, W. R. & Bredas, J. L. Direct Observation of Charge-Induced Pi-Electronic Structural-Changes in a Conjugated Polymer. *Phys Rev Lett* **63**, 1841-1844 (1989).
- 75 Kim, J. & Swager, T. M. Control of conformational and interpolymer effects in conjugated polymers. *Nature* **411**, 1030-1034 (2001).
- 76 Castro Neto, A. H., Guinea, F., Peres, N. M. R., Novoselov, K. S. & Geim, A. K. *Rev. Mod. Phys.* **81**, 109 (2009).
- 77 Visscher, P. B. & Falicov, L. M. *Phys. Rev. B* **3**, 2541 (1971).
- 78 Sercheli, M. S., Kopelevich, Y., da Silva, R., Torres, J. H. S. & Rettori, C. *Solid State Commun.* **121**, 579 (2002).
- 79 Du, X., Skachko, I., Barker, A. & Andrei, E. Y. *Nat. Nanotechnol.* **3**, 491 (2008).
- 80 Tam, Y. W. *Phys. Rev. Lett.* **99**, 246803 (2007).
- 81 Novoselov, K. S. *Nature* **438**, 197 (2005).
- 82 Hwang, E. H. *Phys. Rev. Lett.* **98**, 186806 (2007).
- 83 Chen, J. H. *Nat. Phys.* **4**, 377 (2008).
- 84 Adam, S., Hwang, E. H., Galitski, V. M. & Das Sarma, S. *Proc. Natl Acad. Sci. U.S.A.* **104**, 18392 (2007).
- 85 Ellison, D. J., Lee, B., Podzorov, V. & Frisbie, C. D. Surface Potential Mapping of SAM-Functionalized Organic Semiconductors by Kelvin Probe Force Microscopy. *Adv Mater* **23**, 502-+, doi:DOI 10.1002/adma.201003122 (2011).
- 86 Wang, X., Tabakman, S. M. & Dai, H. *J. Am. Chem. Soc.* **130**, 8152 (2008).
- 87 Sagiv, J. *J. Am. Chem. Soc.* **102**, 92 (1980).
- 88 An, K. H., Jeong, S. Y., Hwang, H. R. & Lee, Y. H. Enhanced sensitivity of a gas sensor incorporating single-walled carbon nanotube-polypyrrole nanocomposites. *Adv Mater* **16**, 1005-+, doi:DOI 10.1002/adma.200306176 (2004).
- 89 Bekyarova, E. *et al.* Chemically functionalized single-walled carbon nanotubes as ammonia sensors. *J Phys Chem B* **108**, 19717-19720 (2004).
- 90 Hecht, D. S. *et al.* Bioinspired detection of light using a porphyrin-sensitized single-wall nanotube field effect transistor. *Nano Lett* **6**, 2031-2036, doi:Doi 10.1021/NI061231s (2006).
- 91 Ulbricht, R. *et al.* Transparent carbon nanotube sheets as 3-D charge collectors in organic solar cells. *Sol Energ Mat Sol C* **91**, 416-419, doi:DOI 10.1016/j.solmat.2006.10.002 (2007).
- 92 Snow, E. S., Novak, J. P., Campbell, P. M. & Park, D. Random networks of carbon nanotubes as an electronic material. *Appl Phys Lett* **82**, 2145-2147, doi:Doi 10.1063/1.1564291 (2003).
- 93 Artukovic, E., Kaempgen, M., Hecht, D. S., Roth, S. & Gruner, G. Transparent and flexible carbon nanotube transistors. *Nano Lett* **5**, 757-760, doi:Doi 10.1021/NI0505254o (2005).
- 94 Unalan, H. E., Fanchini, G., Kanwal, A., Du Pasquier, A. & Chhowalla, M. Design criteria for transparent single-wall carbon nanotube thin-film transistors. *Nano Lett* **6**, 677-682, doi:Doi 10.1021/NI052406l (2006).

- 95 Kocabas, C. *et al.* Experimental and theoretical studies of transport through large scale, partially aligned arrays of single-walled carbon nanotubes in thin film type transistors. *Nano Lett* **7**, 1195-1202, doi:Doi 10.1021/Nl062907m (2007).
- 96 Kang, S. J. *et al.* High-performance electronics using dense, perfectly aligned arrays of single-walled carbon nanotubes. *Nat Nanotechnol* **2**, 230-236, doi:DOI 10.1038/nnano.2007.77 (2007).
- 97 Zhang, M. *et al.* Strong, transparent, multifunctional, carbon nanotube sheets. *Science* **309**, 1215-1219, doi:DOI 10.1126/science.1115311 (2005).
- 98 Fuhrer, M. S., Kim, B. M., Durkop, T. & Brintlinger, T. High-mobility nanotube transistor memory. *Nano Lett* **2**, 755-759, doi:Doi 10.1021/Nl025577o (2002).
- 99 Radosavljevic, M., Freitag, M., Thadani, K. V. & Johnson, A. T. Nonvolatile molecular memory elements based on ambipolar nanotube field effect transistors. *Nano Lett* **2**, 761-764, doi:Doi 10.1021/Nl025584c (2002).
- 100 Cui, J. B., Sordan, R., Burghard, M. & Kern, K. Carbon nanotube memory devices of high charge storage stability. *Appl Phys Lett* **81**, 3260-3262, doi:Doi 10.1063/1.1516633 (2002).

Appendix I.

Nanoscale Conducting Channels at the Surface of Organic Semiconductors Formed by Decoration of Molecular Steps with Self-Assembled Molecules

By Bumsu Lee, Taekjib Choi, Sang-Wook Cheong, and Vitaly Podzorov*

Under certain conditions, self-assembling molecules preferentially bind to molecular steps at the surface of crystalline organic semiconductors, inducing a strong local doping effect. This creates macroscopically long conducting paths of nanoscale width (a single crystalline analogue of organic nanowires) that can span distances of up to 1 cm between electrical contacts. The observed effect of molecular step decoration opens intriguing possibilities for visualization, passivation, and selective doping of surface and interfacial defects in organic electronic devices and provides a novel system for research on nanoscale charge transport in organic semiconductors. In addition, this effect sheds light on the microscopic origin of nucleation and growth of self-assembled monolayers at organic surfaces. It can also have implications in electronic patterning, nanoscale chemical sensors, integrated interconnects and charge-transfer interfaces in organic transistors and solar cells.

inducing much higher carrier densities and surface conductivities, previously inaccessible in OFETs, leading to several advantageous properties and new possibilities for fundamental and applied research.^[4] This fascinating system introduces a concept of a highly conducting charge-transfer interface formed between two nominally insulating organic materials (here, an organic single crystal and a SAM), which is reminiscent of the high-conductivity accumulation layer formed at the interface between certain inorganic oxides, e.g., SrTiO_3 and LaAlO_3 .^[5] A similar concept has been recently used to achieve a high conductivity at the interface between two insulating organic crystals with sufficiently large band offset.^[6] It is estimated that the hole density at an SAM-organic interface is in excess of $3\text{--}5 \times 10^{14} \text{ cm}^{-2}$, corresponding to half a polaron per unit cell, which could lead to a strong polaron-polaron repulsion and a appearance of novel interaction-driven electronic phenomena, such as a metal-insulator transition, superconductivity, and formation of a polaron lattice.^[4,7] In addition, SAM-organic systems show a remarkably fast and reversible electrical response to polar molecules that can be exploited in chemical sensor research.^[8]

Recent studies show that SAM-induced conduction is a general phenomenon that occurs in small-molecule and polymer organic semiconductors. For example, record-high electrical conductivities have been reported in SAM-doped conjugated polythiophenes.^[9] Such generality suggests a fundamental importance of SAM-induced conduction as a phenomenon and its versatility as a doping method for a strong modification of electronic properties of different organic materials. This set of properties makes the SAM-organic system very promising for applications in chemical sensors, transparent electrodes, integrated interconnects, and charge-transfer interfaces for organic electronic devices. Understanding the basic mechanisms of this effect is, therefore, very important for fundamentals and future applications.

Remarkably, the microscopic origin of SAM-induced conduction, as well as the mechanism of SAM growth at organic surfaces, still remains a mystery. It has been suggested only recently that SAM-induced conductivity is due to the unbonded free silanol groups (Si-OH) available in hydrolyzed partially crosslinked 2D SAMs that result in the acidic protons at the SAM-organic interface and protonic doping of the surface.^[6] The mechanism of SAM nucleation and growth at the surface of molecular crystals is

1. Introduction

Charge carrier transport in organic semiconductors is a topic of active ongoing research aimed at obtaining a better understanding of organic field-effect transistors (OFETs) and photo-voltaic cells (OPVs), important building blocks of organic optoelectronics.^[1] Specifically, organic molecular crystals have emerged as a platform for studies of intrinsic charge transport and optical properties of small-molecule organic semiconductors and related devices.^[2,3] In OFETs, conduction is due to mobile charge carriers electrostatically induced at the semiconductor-dielectric interface by the application of a gate electric field. The recently reported effect of self-assembled monolayers (SAMs) of silanes grown at the surface of organic crystals provides an exciting complementary method of

[*] Prof. V. Podzorov, B. Lee, Dr. T. Choi, Prof. S.-W. Cheong
Physics Department, Rutgers University
Piscataway, NJ 08854 (USA)

E-mail: podzorov@physics.rutgers.edu

Prof. V. Podzorov, Prof. S.-W. Cheong
Institute for Advanced Materials and Devices for Nanotechnology
Rutgers University
Piscataway, NJ 08854 (USA)

Dr. T. Choi, Prof. S.-W. Cheong
Rutgers Center for Emergent Materials
Physics Department, Rutgers University
Piscataway, NJ 08854 (USA)

DOI: 10.1002/adfm.200901525

also puzzling: chemistry dictates that the SAM molecules used in these studies should not covalently bond to pure organic semiconductors, including oligoacenes, rubrene, or polythiophenes.^[6]

In this work, we studied the local nanoscale morphology of SAM nucleation and early stages of growth on organic crystals by atomic force microscopy (AFM), conducting tip AFM (C-AFM), and charge transport measurements. We discovered that SAM nucleation on organic semiconductors predominantly occurs at molecular steps. Subsequent growth leads to SAM-decorated crystalline paths of nanoscale width possessing high conductivity. This effect suggests that an oxygen-containing defect preferentially located at the steps plays an important role in SAM anchoring and nucleation at these surfaces.

This effect allows for the controllable formation of a conceptually new type of nanoscale conducting channels at organic surfaces: a crystalline analogue of conducting nanowires imbedded in the surface of an insulating organic crystal. Indeed, when only molecular steps are coated with SAMs, conduction occurs along the crystalline steps under the SAMs. The steps have the same molecular packing as the entire single crystal and span over macroscopic distances of up to a centimeter at the crystal facet without interrupting each other, thus creating very long conduction paths in the crystal bridging the electrical contacts. In recent years, organic nanowires and nanofibers attracted much attention for their potential use in organic nanoelectronics.^[10–12] Conventional nanowires consist of columnar molecular π -stacks grown or deposited from a vapor phase or a solution, which provides an important advantage of processability for integration into devices. However, it is difficult to simultaneously obtain very long and molecularly thin nanowires. Typically, growing nanowires longer than a few micrometer results in rather thick “ropes” with a diameter greater than a few 100 nm (the so-called “1D crystals”).^[10] Although the conducting nanochannels reported here lack the advantage of processability, they are important for fundamental research on charge transport because the nanochannel width and length are defined by the molecular step size (~ 1 nm) and macroscopic dimensions of the single crystal samples, respectively. The effect of self-assembly along the molecular steps allows us to achieve this remarkable geometry by simply performing a very short exposure of organic crystals to SAM vapor.

2. Results and Discussion

One of the important basic questions pertinent to the observed growth of silanes on molecular crystals is the mechanism behind SAM nucleation occurring at organic surfaces. The SAM molecule used in this study (tridecafluoro-1,1,2,2-tetrahydrooctyltrichlorosilane ($\text{C}_{18}\text{H}_{33}\text{F}_{11}\text{SiCl}_3$), or simply fluoroalkyl trichlorosilane (FTS), is a member of a large family of silanes that have been extensively used for passivation of surfaces of inorganic oxides (e.g., SiO_2).^[13] In the case of SiO_2 , the mechanism of SAM formation involves three basic steps:^[14]

1) hydrolysis, which converts trichlorosilane groups of SAM molecules, SiCl_3 , into silanol groups, $\text{Si}(\text{OH})_3$; 2) covalent bonding of hydrolyzed (fluoro)alkyl silanes to OH-terminated SiO_2 surface, as the result of which Si–O–Si bridges to the substrate are formed; and finally 3) in-plane polymerization of SAM molecules via covalent bonding of free silanol side groups of the adjacent SAM molecules. In this process, a stable, fully crosslinked SAM layer covalently bonded to SiO_2 substrate can be formed. This process requires a) water in the vapor phase or water at the surface to promote hydrolysis of trichlorosilanes and b) availability of surface OH groups on SiO_2 for covalent anchoring of the SAM to the substrate. It is likely that similar requirements must be met for sustainable growth of a stable SAM on organic surfaces.

In this study, we used the so-called “pristine” rubrene crystals, i.e., high-purity crystals produced using an optimized crystal growth technique (see, e.g., references 1–3), stored in air and in the dark, implying that these crystals are not intentionally oxidized. Electrical contacts have been prepared using graphite ink or silver evaporated through a shadow mask. The metal evaporation procedure developed to prevent damaging organic crystals has been followed.^[15,16] The high-vacuum gauge was turned off during the deposition to avoid the detrimental “gauge effect”.^[17] Keithley source-meters K2400 and electrometers 8514 have been used for electrical measurements. Imaging studies were performed with Digital Instruments multi mode AFM.

Figure 1 shows AFM topographies of the surfaces of a) pristine rubrene crystal, b–d) rubrene crystals exposed to FTS vapor for short periods of time (2–10 min), and e) a rubrene crystal that has been exposed to FTS for a few hours. The bottom right panel in Figure 1 shows AFM profiles taken along the dotted lines in Figure 1a, b, and e. The AFM images corresponding to the initial stages of FTS growth (b–d) show that the appearance of molecular steps has clearly changed compared to the pristine rubrene: they have gained contrast and become reminiscent of “rivers” of finite

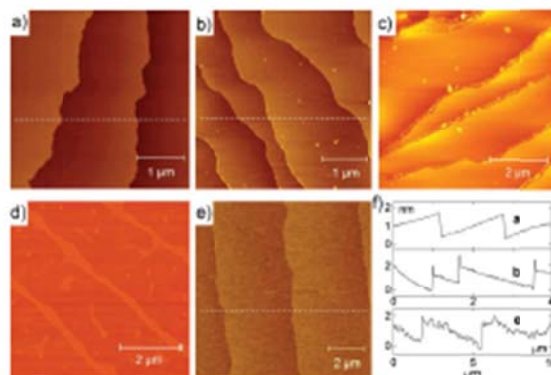


Figure 1. AFM topography of molecular steps in rubrene decorated by SAMs (bopping mode): a) pristine crystal; b) crystal treated with FTS vapor for a very short time, $\Delta t = 2$ min; c) $\Delta t = 3$ min; d) $\Delta t = 10$ min; and e) fully coated rubrene crystal (treated for a few hours). The bottom right panel shows AFM profiles taken along the dotted lines in a, b, and e.

width. A comparison of AFM profiles (traces a and b) shows the appearance of "spikes" at the step edges after a short FTS treatment, suggesting that the SAM starts growing at the steps. Detailed analysis of these spikes shows that their width is limited by the lateral resolution of our AFM defined by the tip radius (~ 20 nm), which indicates that the actual width of the SAM-decorated region is < 20 nm. After longer treatment, the width of these rivers increases (Fig. 1d), and after a very long treatment, the entire surface becomes coated with a continuous monolayer resulting in a fuzzy AFM image, where the noise is due to the interaction of AFM tip with a soft SAM surface (see Fig. 1e and the corresponding trace e). It is interesting that the underlying molecular steps structure of the crystal in this case can still be clearly seen under the completed SAM, this implies that the layer is indeed a monolayer with a thickness that is not much greater than the height of molecular steps in rubrene (1.5 nm),¹⁶ as originally suggested.¹⁶ These data show that SAM nucleation at the surface of pristine rubrene crystals first occurs at molecular steps. It is worth mentioning that nucleation of SAMs in the middle of terraces can also be observed either after longer FTS exposure, or as the result of crystals having a higher density of surface defects. This can be seen as bright "dots" at the terraces in Figure 1b and c and "islands" in Figure 1d.

The C-AFM measurements of these samples with SAM-decorated steps reveal that these steps are conducting. In C-AFM technique, a fixed dc voltage is applied to a conducting AFM tip with respect to the grounded sample, and a dc tip-sample current is measured while scanning the surface in contact mode (see inset in Fig. 2). Lighter color in C-AFM images corresponds to a higher tip-sample current. Figure 2a shows contact-mode topography (upper panel) and the corresponding local conductivity map (middle panel) simultaneously acquired at the same area of rubrene crystal with SAM-decorated steps. A one-to-one correspondence between the topography and the local conductivity distribution is observed. The current profile measured along the dotted line shows that the tip-sample current reaches maxima at the step edges: the highest tip-step current was 7 nA at the tip-sample bias of 0.8 V (lower panel in Fig. 2a). Figure 2b shows the same type of measurement performed on a pristine (no FTS treatment) rubrene crystal. In this case, no local conductivity associated with molecular steps was detected, indicating that the steps of pristine crystals are not conducting, even though they might be unintentionally oxidized. This proves that the conducting pattern shown in Figure 2a is due to the decoration of molecular steps with SAMs.

It is important to mention that the observed effect of SAM nucleation at molecular steps is not purely morphological in origin: simply the presence of molecular steps at the surface is not sufficient for the SAM decoration to occur. Indeed, we have not been able to observe any FTS nucleation on crystals that have a high ionization potential, such as tetracyanoquinodimethane (TCNQ), even though TCNQ crystals also show well-defined molecular steps at the surface.¹⁶ Consistently, electrical conductivity of TCNQ crystals is not affected by FTS vapor. Therefore, specific chemistry of molecular steps of a sample is important for FTS binding. Most of the organic semiconductors with high ionization potentials (i.e., those that usually form n-type OFETs in a combination with gold or graphite contacts) can not be easily oxidized.¹⁷ Hence, the difference we observed between the responses of the crystals with low and high ionization potential to FTS suggests that oxygen-containing species preferentially located at the steps play a crucial role in anchoring SAMs to the organic surface.

We performed local current-voltage, I - V , measurements of SAM-decorated molecular steps using a C-AFM tip positioned above a conducting step (Fig. 3). These measurements reveal asymmetrical I - V characteristics: at a negative tip bias (relative to the grounded sample), the current is much larger, more linear, and less noisy than at positive biases. This behavior is consistent with the model of the SAM inducing holes in the crystal. Indeed, when a negative voltage is applied to the tip in contact mode, holes under the SAM are attracted to the SAM-crystal interface, forming a nanoscale "capacitor" with a tunneling barrier consisting of an insulating SAM, as schematically depicted in the inset at Figure 3. At the opposite polarity, no nanoscale tunneling gap can be formed, resulting in a much smaller current.

It is worth mentioning that an in-plane conductivity of an ensemble of decorated molecular steps spanning a macroscopically

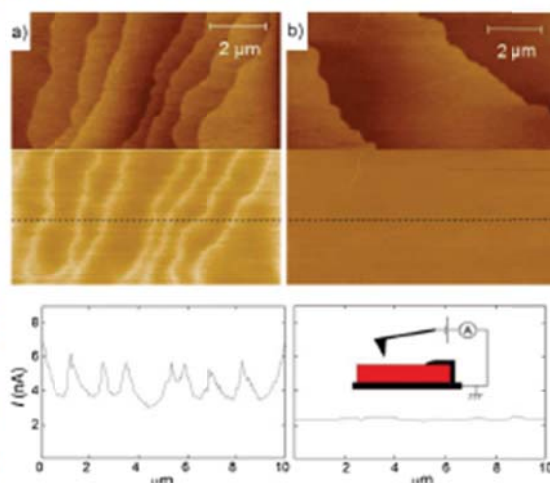


Figure 2. C-AFM measurements of molecular steps in rubrene (upper: contact-mode topography; lower: local conductivity maps, where lighter color corresponds to higher tip-sample current): a) crystal with molecular steps decorated by a SAM using a very short FTS treatment (~ 2 min); b) pristine untreated crystal. The lower panels show current profiles measured with C-AFM along the dotted lines in a and b. These data show that SAM-decorated steps are conducting, while the steps of pristine crystals are not.

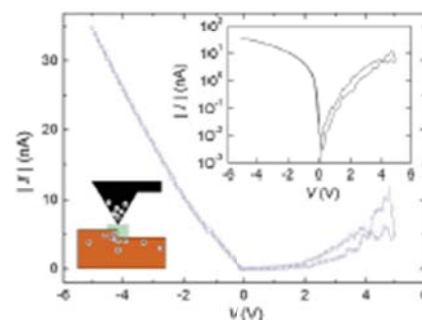


Figure 3. Local I-V curve obtained with C-AFM, when the conducting tip is positioned at a SAM-decorated molecular step (the inset shows the same data in a semilog plot). At negative tip biases, tip-sample current is much larger, which is indicative of the hole conductivity induced by the SAM in the crystal. The diagram depicts the model in which a nanoscale tunneling gap forms between the tip and SAM-induced holes in this biasing regime.

large area over the crystalline facet can be measured. Crystallographic properties of high-quality molecular crystals allow molecular steps to extend over great distances on flat facets without intercepting each other. Frequently, molecular steps have similar orientations over the whole area of a large facet (confirmed by AFM). This feature allowed us to use macroscopically large structures with contacts prepared by thermal evaporation to measure the anisotropy in transport properties of samples with SAM-decorated steps. We fabricated a number of samples with four Ag contacts that defined two perpendicular conduction channels of the same length $L=50\ \mu\text{m}$, but different widths, $W=0.5\text{--}4\text{ mm}$, determined by the sizes of the crystals. These channels probe charge transport in the a and b crystallographic directions at the surface of rubrene (Fig. 4). Using these structures, we simultaneously measured sheet conductivities in the a and b directions *in situ*, while the crystal was treated with FTS vapor.

Figure 4 shows the dynamics of the current, $I(t)$, flowing in one of the channels (solid line) and the ratio of sheet conductivities, $\sigma_a/\sigma_b(t)$ (circles), for the sample with molecular steps preferentially oriented along b -axis. According to our observations, typical values of σ_a/σ_b before the treatment and after a full monolayer is grown are between 2.1 and 3, which is consistent with the transport anisotropy measured in field-effect transistors.^[20–24] This anisotropy is a consequence of the slipped-stack packing motif of rubrene molecules resulting in a good π -orbital overlap in b direction of the crystal (Fig. 5), which is consistent with quantum chemical calculations.^[24] During the initial stages of SAM growth, i.e., when a rapid increase of the current is observed, σ_a/σ_b shows a maximum at about 1–2 min after the beginning of FTS exposure. Comparison with the AFM data (Fig. 1) suggests that this maximum corresponds to the formation of SAM-decorated conducting steps running preferentially in b direction. This measurement provides a timescale, at which SAM decoration of molecular steps occurs ($\sim 1\text{--}2\text{ min}$), as well as an additional confirmation that the SAM-decorated steps are conducting.

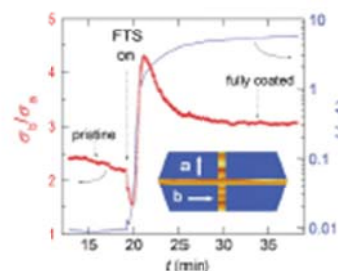


Figure 4. Circles: Anisotropy of sheet conductivity, σ_a/σ_b , measured *in situ* at the surface of a macroscopic rubrene single crystal during the growth of the SAM. This is obtained by simultaneously measuring two channels oriented along the a - and b -axis (see inset diagram). Solid line: the corresponding dynamics of the current flowing in the b -axis channel at 4 V applied between the contacts. The crystals chosen for these measurements have molecular steps preferentially oriented along the b -axis, as shown in the inset. The maximum in σ_a/σ_b is reached when molecular steps are decorated with SAM.

The data collected in this work imply that a) molecular steps of pristine p -type organic crystals comprise species responsible for binding FTS SAMs to these materials and b) these species are likely oxygen-containing molecules of the semiconductor (here, a form of rubrene oxide, such as an epoxy or hydroxy group), that preferentially forms along the molecular steps, when freshly grown crystals are exposed to ambient air.

Our observations are supported by the recent theoretical work by Tietzer and Parnellides, which shows that formation of

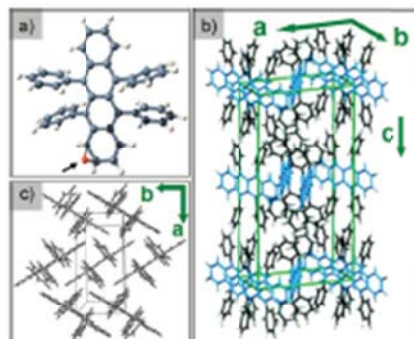


Figure 5. a) Calculations show that the most easily formed oxidative state of rubrene molecule is an epoxy group on a) Calculations show that the most easily formed oxidative state of rubrene molecule is an epoxy group on the end ring of the rubrene core [26]. According to the bulk crystal structure of rubrene (b) and the slipped-stack packing motif at the (a,b) crystal facet (c), the end rings of rubrene core are exposed to the ambient along the molecular steps at this largest natural crystal facet.

Appendix II.

Modification of Electronic Properties of Graphene with Self-Assembled Monolayers

B. Lee,[†] Y. Chen,[†] F. Duerr,[‡] D. Mastrogianni,[‡] E. Garfunkel,^{†,§} E. Y. Andrei,[†] and V. Podzorov^{*,†,§}[†]Department of Physics, [‡]Department of Chemistry, and [§]Institute for Advanced Materials and Devices, Rutgers University, Piscataway, New Jersey 08854

ABSTRACT Integration of organic and inorganic electronic materials is one of the emerging approaches to achieve novel material functionalities. Here, we demonstrate a stable self-assembled monolayer of an alkylsilane grown at the surface of graphite and graphene. Detailed characterization of the system using scanning probe microscopy, X-ray photoelectron spectroscopy, and transport measurements reveals the monolayer structure and its effect on the electronic properties of graphene. The monolayer induces a strong surface doping with a high density of mobile holes ($n > 10^{13} \text{ cm}^{-2}$). The ability to tune electronic properties of graphene via stable molecular self-assembly, including selective doping of steps, edges, and other defects, may have important implications in future graphene electronics.

KEYWORDS Graphene, self-assembled monolayers, graphene edge functionalization, doping of graphene, transport in graphene

Self-assembled monolayers (SAMs) are ultrathin molecular films spontaneously formed at surfaces or interfaces due to chemical or physical interactions of molecules with a substrate, frequently without necessity of high-vacuum or high-temperature processing.¹ SAMs have received considerable attention due to their use in organic electronics as active materials or insulators.^{1–4} Recently, it has been demonstrated that electronic properties of small-molecule and conjugated polymer organic semiconductors can be drastically modified by SAMs.^{5–7} In this Communication, we report the effect of a self-assembled monolayer of (tridecafluoro-1,1,2,2-tetrahydrooctyl)trichlorosilane ($\text{C}_{13}\text{H}_9\text{F}_{13}\text{SiCl}_3$), or simply fluoroalkyltrichlorosilane (FTS),⁸ on the electronic properties of highly ordered pyrolytic graphite (HOPG) and graphene. The latter system has attracted considerable attention due to the massless character of quasiparticles and the related novel mesoscopic transport properties.⁹ Our studies using atomic-force microscopy (AFM), scanning electron microscopy (SEM), X-ray photoelectron spectroscopy (XPS), and Hall effect measurements reveal that a dense, uniform, and stable FTS SAM can be grown at the surface of graphene, inducing an excess of holes with a density of up to $n \sim 1.5 \times 10^{13} \text{ cm}^{-2}$. Such a level of doping is unattainable in conventional field-effect transistor (FET) devices. In addition, the SAM–graphene system is found to be very stable (even at elevated temperatures) in high-vacuum and ambient environment. Such robustness and the large electronic effect suggest that integration of SAM with graphene provides a new and reliable method of achieving ultrahigh doping levels in graphene.

The samples used in this study were rectangular pieces of multilayer HOPG and single-layer graphene FETs. The HOPG samples had length and width, $L \sim W = 2\text{--}5 \text{ mm}$, and thickness $d = 3\text{--}20 \mu\text{m}$, comprising $1\text{--}6 \times 10^4$ individual layers (Figure 1). The electrical contacts to HOPG were prepared by applying colloidal graphite paint to the sides of the samples, thus forming electrical contacts to all the layers. Graphene FETs were prepared on $\text{SiO}_2/\text{n-Si}$ wafers using mechanical exfoliation techniques and e-beam lithography (the details can be found elsewhere⁹). Before the SAM growth, devices were annealed in a flow of ultrahigh purity

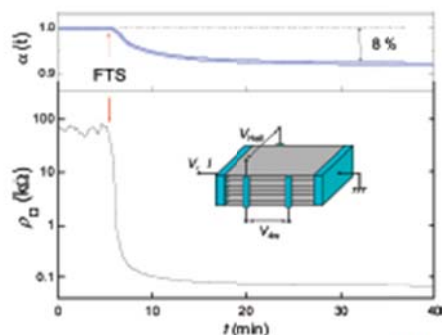


FIGURE 1. The effect of an FTS self-assembled monolayer on the resistivity of HOPG. (Top) Normalized resistivity $\rho(t) = R(t)/R_0$ of multilayer ($>10^4$ layers) HOPG measured as a function of FTS treatment time (t). Initial values of R vary from sample to sample by as much as 100%. The red arrows indicate the onset of FTS exposure. (Bottom) The corresponding effect on the resistivity of an individual single layer of graphite calculated using eq 1. The sketch shows a Hall-bar sample geometry used throughout this study.

* To whom correspondence should be addressed; podzorov@physics.rutgers.edu.
Received for review: 02/18/2010
Published on Web: 05/26/2010

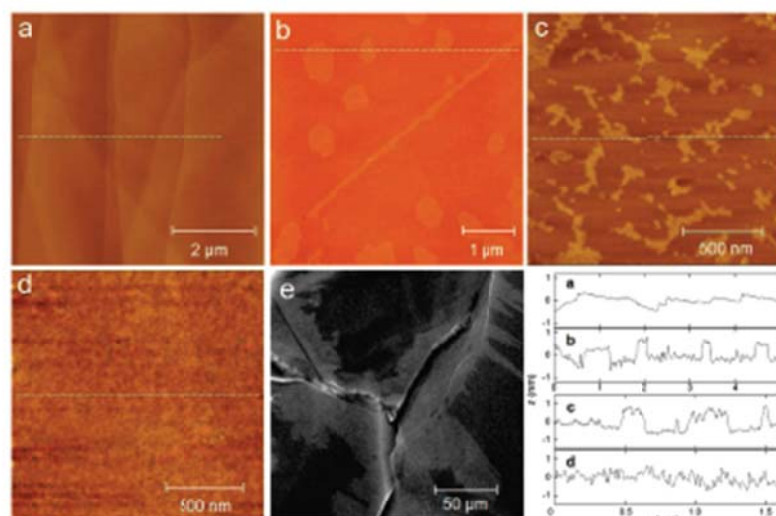


FIGURE 2. AFM (a–d) and SEM (e) images of a graphite surface functionalized with FTS SAM. (a) AFM of pristine HOPG surface (0.1 nm rms roughness); (b) and (c) AFM images of partially coated samples (1–2 min FTS exposure), showing different morphologies of SAM islands, including a SAM-decorated graphene edge in (b); (d) AFM of a fully coated sample (1 h exposure) showing a “fuzzy” surface morphology with 0.37 nm rms roughness; (e) a large-area SEM image of a HOPG sample partially coated with the SAM (10 min exposure), with lighter shade corresponding to SAM-coated regions. The last panel shows AFM profiles taken along the dotted lines in panels a, b, c, and d, indicating that the SAM layer is 1 nm thick.

(UHP) argon at 120 °C for 90 min and transferred under argon to the FTS growth chamber (this step is necessary for achieving a high-quality SAM on graphene). The chamber was evacuated, and then the samples were exposed to a saturated vapor of FTS. Electrical characteristics of the samples were measured in situ during the SAM growth. We have performed control experiments verifying that no intercalation of SAM molecules or any byproduct of their growth occurred in the bulk of the HOPG samples, confirming that the changes of the electrical conductivity observed are indeed due to a very strong doping of the top (exposed) graphite layer.

As the result of an FTS treatment, the resistance of HOPG samples typically decreases by 5–20%, observed both in two-probe and four-probe configurations (Figure 1, top panel). The magnitude of the decrease depends on the thickness and the initial resistance, R_0 , of these macroscopically thick samples: $R(t) = \alpha(t)R_0$, where $\alpha = 0.8–0.95$ in a saturated state. Such a considerable decrease of R in samples with a typical number of layers $N = 1–6 \times 10^4$ suggests that SAM modification of the top graphite layer is very strong. Indeed, since the screening length in graphite is only ~ 0.5 nm,¹⁰ only resistance of the top layer should be affected, and the sample can be represented by $N - 1$ undoped and one (top) doped layers

connected in parallel. Hence, the resistivity of the top layer can be expressed as

$$\rho = \left(\frac{W}{L} \right) \frac{\alpha N}{N(1 - \alpha) + \alpha} R_0 \quad (1)$$

where the coefficient $\alpha(t) = R(t)/R_0$ is determined experimentally from $R(t)$ measurements (upper panel of Figure 1). Hence, for a $3.5 \mu\text{m}$ thick sample with $N \approx 1.16 \times 10^4$ and $\alpha(t \geq 30 \text{ min}) = 0.92$ (the 8% blue curve in the upper panel of Figure 1), eq 1 gives the resistance of the top layer, $\rho_0(t)$, decreasing from $\sim 70 \text{ k}\Omega/\square$ to $\sim 65 \Omega/\square$ (i.e., by $\sim 10^3$ times), as the result of the SAM doping (lower panel of Figure 1).

In order to understand nanoscale morphology of the SAM–graphene system, we have performed AFM and SEM studies of partially and fully coated samples. Figure 2a shows an AFM of a pristine HOPG (~ 0.1 nm rms roughness): faint thin lines are ~ 0.3 nm high graphene steps. AFM images of a partially coated surface are shown in parts b and c of Figure 2. We have observed three types of morphology: round islands sparsely distributed on the surface (Figure 2b), ribbon-like regions corresponding to the SAM growing along the graphene steps (Figure 2b), and smaller, irregular shaped

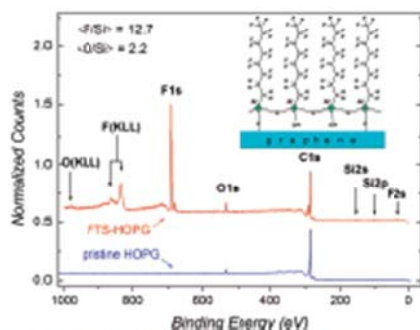


FIGURE 3. XPS of pristine (lower spectrum) and FTS-coated (upper spectrum) HOPG. Quantitative analysis based on the comparison of peak areas gives the following elemental ratios: F/Si = 12.7 ± 0.5 and O/Si = 2.2 ± 0.2 (compare with the theoretical values F/Si = 13 and O/Si = 2 for the model in the sketch). A small oxygen signal clearly present in pristine samples is consistent with oxidized graphene steps that likely play an important role in SAM nucleation. Absence of Cl in the spectra indicates that the monolayer is fully hydrolyzed. The sketch shows the suggested chemical structure of the SAM-graphene system.

islands with a higher nucleation density (Figure 2c). The topography shows that all these islands are flat regions with thickness 1.0 ± 0.2 nm, which is consistent with the length of an FTS molecule (the last panel in Figure 2). The variations in the morphology likely originate from different types and densities of defects on graphene surfaces that form SAM nucleation sites. AFM of a fully coated surface has a flat, but "fuzzy", morphology with a ~ 0.37 nm rms roughness (Figure 2d), which is consistent with the interaction of an AFM tip with a soft SAM. Figure 2e shows a $200 \times 200 \mu\text{m}^2$ SEM image of HOPG partially coated with FTS. A surprisingly high (for a monolayer) electronic contrast in this SEM image is likely due to the electron-rich fluoroalkyl groups of the SAM, which allows for a clear identification of the monolayer growth pattern on a large scale. In this sample, it appears that the SAM nucleation had occurred along the cracks, followed by a lateral spreading of the monolayer along the surface. These images, taken at various stages of the SAM formation, confirm that FTS forms a monolayer at graphite surface. It is worth noting that the growth is a self-limiting process, because we have not been able to observe any evidence of a second layer nucleation on top of the fully coated samples.

Elemental composition of SAM on graphite has been investigated by XPS (Figure 3). By obtaining statistics on many FTS-HOPG samples, we have concluded that a clean graphite surface is very important for successful SAM growth. We accomplished this by using a freshly exfoliated graphite samples and annealing them in a flow of UHP Ar at 120°C for ~ 90 min with a subsequent transfer into the FTS chamber without exposure to air. Comparison of the areas

of F 1s and Si 2p peaks of the FTS-HOPG sample (the upper spectrum) gives a F/Si ratio of 12.7 ± 0.5 , which is in a good agreement with the actual molecular stoichiometric ratio of 13.

XPS also helps to understand the growth mechanism of silane SAMs on graphite. According to the trichlorosilane chemistry on SiO_2 , FTS molecules first undergo hydrolysis in the presence of water at the surface or in a vapor phase, and all three chlorine atoms are replaced by hydroxyl groups (OH). One of them then covalently bonds to the OH-terminated Si substrate by forming a Si-O-Si bond. The other two OH groups covalently bond to the adjacent FTS molecules via Si-O-Si links formed in a similar fashion.⁷ Here, we propose a similar, but somewhat different, growth mechanism for the FTS-graphite system.

First, our XPS data show no chlorine signal in the fully coated samples (the Cl peak would have appeared at ~ 200 eV in the upper spectrum), indicating that FTS undergoes a complete hydrolysis, and HCl byproduct is removed from the system. We believe that the source of water in our experiment is the residual gas in the SAM treatment chamber (the base pressure before the SAM deposition is about 3×10^{-3} Torr). Annealing of the samples in Ar prior the SAM growth, on the other hand, helps to remove some organic contaminants and excess of water from the surface of graphite. This last point is very important, because in a separate control experiment, no SAM could be grown on the samples intentionally incubated in a water vapor bath, indicating that too much water at the surface is detrimental for the SAM growth.

Second, a small O 1s signal is clearly observed in all freshly exfoliated HOPG samples (the lower spectrum) is consistent with only the graphene steps being oxidized. Oxygenated species, such as graphene oxide, hydroxyl, or carboxyl groups, may play a key role in SAM nucleation on graphite. Initially, FTS molecules covalently anchor to these defects, and once such nucleation sites are formed, other FTS molecules covalently attach to them via Si-O-Si bonds, without forming strong bonds to the substrate. This process, known in silane chemistry as 2D self-polymerization, does not require surface oxygen, except for oxygen species at the anchoring sites.⁷ As a result, most of the FTS molecules in the monolayer are covalently bonded to the neighboring FTS molecules, but only a few are covalently bonded to the graphite substrate (sketch in Figure 3). The Si/O ratio for the fully coated samples obtained from our XPS spectra is 2.2 ± 0.2 . According to the silane chemistry,⁷ in an ideal monolayer, each Si atom is connected to three O, two of which are shared between the adjacent FTS molecules in a 2D polymerized network (sketch in Figure 3). In such a structure, the expected Si/O ratio is 2. For an unpolymerized, yet fully hydrolyzed, trichlorosilane, the expected Si/O ratio is 3. Therefore, our XPS data suggest that in the SAM-graphene system FTS undergoes a complete hydrolysis and forms an almost fully cross-linked interconnected 2D SAM network

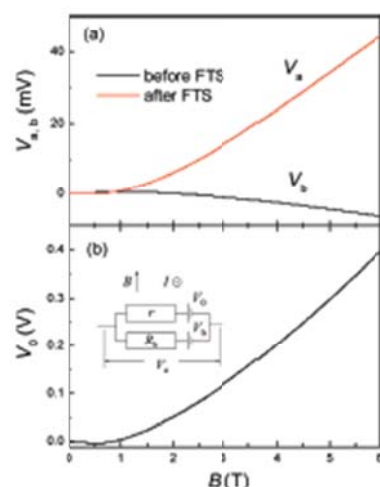


FIGURE 4. Hall effect measurements of graphite functionalized with an FTS SAM. (a) Hall voltage of a HOPG sample measured before (black) and after (red) FTS treatment. A clear change of sign at $B \sim 1$ T is observed. (b) Hall voltage of a SAM-doped single-layer graphite extracted from panel a using eq 2 and the corresponding circuit model (depicted).

(Figure 3). The fact that no Cl signal is detected in XPS measurements provides solid proof that the observed doping effect is not induced by Cl byproducts of the SAM formation.

To further investigate the effect of the SAM on the electronic properties of graphite, we have carried out Hall effect measurements of HOPG before and after the FTS growth. Although the change in the resistance of HOPG samples is only a few percent because of a large number of unaffected layers (Figure 1), the situation is drastically different in the Hall measurements. Figure 4a shows the Hall voltage measured in a typical HOPG sample. The most prominent feature is a different sign of the Hall voltage at $B > 1$ T. In addition, the magnitude of the Hall voltage becomes much larger after FTS treatment. A SAM-coated HOPG sample can be represented by two parts connected in parallel: a highly conductive hole-doped top layer and a bulk. As a semimetal, pristine HOPG has a gapless multielectronic-band structure. The sign of the Hall voltage measured in HOPG samples is determined by the relative amount of electrons and holes. At high magnetic fields, the electron and hole bands become separated by a gap of several tens of millielectronvolts.¹³ As a result, transport in HOPG becomes dominated by one type of carrier that defines the sign of the Hall voltage. The sample in Figure 4a shows a negative Hall voltage before FTS treatment, which in our experimental setup corresponds to predominantly electron conduction. After FTS treatment, the Hall voltage becomes positive,

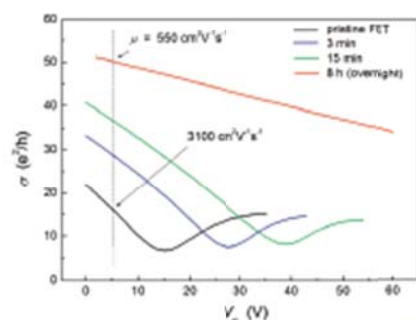


FIGURE 5. Evolution of transconductance characteristics, $g(V_g)$, of a graphene FET measured in situ as an FTS SAM grows on a graphene surface. The data have been collected at different growth times: 0 (pristine graphene), 3 min, 15 min, and 8 h. Mobilities of the pristine graphene FET and the same device treated overnight are 550 and $550 \text{ cm}^2 \text{ V}^{-1} \text{ s}^{-1}$, respectively (calculated at $V_g = 5 \text{ V}$).

indicating the addition of holes to the sample. The inset in Figure 4b shows a model of the Hall effect in FTS-coated HOPG: the transverse (i.e., Hall) voltages and longitudinal resistances are shown with an excitation current perpendicular to the page. The top layer, dominated by the SAM-induced holes, has a longitudinal resistance $r(B)$ and generates a Hall emf V_0 when the magnetic field is applied. The HOPG bulk has a longitudinal resistance $R_L(B)$ and a Hall emf V_b . The total Hall voltage after FTS coating, V_a , is a function of these four parameters. By combining the measured Hall voltages and magnetoresistance values $r(B)$ and $R_L(B)$ (not shown here for simplicity) before and after FTS growth, we can extract the contribution of the top (doped) layer to the Hall effect:

$$V_0 = V_a + (V_b - V_a)r(B)/R_L(B) \quad (2)$$

The extracted V_0 is plotted in Figure 4b. As expected, V_0 has a positive sign at high magnetic fields, corresponding to hole doping. As a first approximation, we apply the equation for a conventional band-semiconductor Hall effect to the nearly linear section of $V_0(B)$ in Figure 4b, $\Delta V_0 = \Delta B I_0 / (en)$, where the longitudinal current is $I_0 = (W/L)\sigma_{xx}V_{xx}$ and $\sigma_{xx} = en\mu$, and obtain the hole density $n = 1.4 \times 10^{13} \text{ cm}^{-2}$ and hole mobility $\mu = 3700 \text{ cm}^2/\text{Vs}$. Such remarkable carrier density is difficult to achieve electrostatically in FETs.

We have also performed FTS growth and electrical measurements on single-layer graphene FETs. Several samples were studied and showed similar results. The transconductance of graphene FETs, $g(V_g)$, was monitored in situ, as FTS SAM was growing on the surface of the sample (Figure 5). These devices show only a minor hysteresis in V_g sweeps (much smaller than the effect of SAMs reported below), and

hence for clarity we show the data recorded in one (positive) direction of the V_g sweep. There are several important observations: (1) the initial Dirac point of pristine graphene is at $V_g = 15$ V but shifts to more positive V_g as the SAM is growing and eventually goes beyond the experimentally accessible range of gate voltages; (2) away from the Dirac point, the conductivity shows a sublinear increase with V_g both for pristine and briefly treated samples (≤ 15 min), but becomes linear for a saturated monolayer SAM coverage (longer treatments); (3) the conductivity of graphene increases with FTS growth, while the field-effect mobility decreases.

A nonzero V_g of the Dirac point in as-prepared graphene is usually understood in terms of unintentional doping by species absorbed from the ambient.^{12,13} As the FTS SAM is grown on graphene, the Dirac point is shifted toward more positive V_g , indicating that holes are induced in the sample at a density $\Delta n = \gamma \Delta V_g^{\text{Dirac}}$, with $\gamma = 7.2 \times 10^{10} \text{ cm}^{-2} \text{ V}^{-1}$. The most significant and rapid changes in the electrical characteristics of the devices occur within the first ~ 60 min of the FTS growth (correlated with the time scale of the monolayer formation), after which the process slows down and saturates. To make sure that all the possible "pin-holes" are sealed by the SAM, we have prepared fully coated samples by an overnight FTS treatment. For a complete SAM (red curve in Figure 5), the position of the Dirac point is estimated by extrapolating the experimentally accessible linear portion of the curve to a minimum conductivity of $\sim 7 \text{ e}^2/h$, leading to a density of SAM-induced holes, $\Delta n \approx 1.2 \times 10^{13} \text{ cm}^{-2}$, close to the value obtained from our Hall effect measurements.

Observations (2) and (3) above can be explained by the model of long-range Coulomb scattering due to charged impurities, in which long-range scattering leads to a linear dependence of σ on carrier density, whereas short-range scattering results in a sublinear dependence.^{14–16} FTS extracts electrons from graphene, which converts SAM molecules into negatively charged static centers interacting with mobile holes through a long-range Coulomb interaction. Correspondingly, in Figure 5, the $\sigma(n)$ dependence changes from sublinear to linear with μ decreasing, as more and more SAM molecules are introduced onto the surface, and the dominant scattering mechanism becomes long-range Coulomb interactions with charged impurities. The theory of long-range scattering in graphene also shows that mobility is inversely proportional to the density of scattering centers: $\mu = 1.1 \times 10^{15} \epsilon / n_{\text{sc}} \text{ cm}^2 \text{ V}^{-1} \text{ s}^{-1}$, where ϵ is the dielectric constant of the material that contains scattering centers¹⁶ (e of an FTS monolayer is estimated to be $\sim 3.5^{17}$). Combining these results, we can estimate the density of SAM-related scattering centers for a complete monolayer on graphene: $n_{\text{sc}} = 0.67 \times 10^{13} \text{ cm}^{-2}$, i.e., about 1/2 of the density of SAM-induced holes. This result is not unexpected, since the FTS SAM is a dense cross-linked layer, and FTS molecules may not necessarily be treated as independent scatterers.

After initial measurements, the FTS-graphene devices were left in ambient air (relative humidity ~ 60 – 70%) for more than 1 week and then remeasured. The FTS-induced conductivity decreased by only a few %, compared to the result obtained on freshly coated samples while still in vacuum. In addition, neither the monolayer nor the SAM-induced conductivity has been destroyed by annealing FTS-graphene devices in forming gas at 120°C . These stability tests indicate that the SAM-graphene system is very stable even at elevated temperatures.

There is a qualitative agreement between our results on HOPG and graphene FETs: in both cases a strong p-type doping with a large carrier density has been observed. The quantitative differences in the SAM-induced single-layer σ in these cases might arise from: (a) different band structures of an isolated graphene and multilayered graphite, (b) different relative weights of various scattering mechanisms, and (c) an extra scattering in graphene FETs caused by the underlying SiO_2 .

It is worth noting that our observation of SAM decoration of graphene edges (Figure 2b) confirms the hypothesis of edge termination with oxygen species.¹⁸ Indeed, according to the trichlorosilane chemistry on SiO_2 , such groups as hydroxyl (OH) or carboxyl (COOH) are necessary for the SAM molecules to covalently bond to the surface.¹⁹ Our observation suggests that the mechanism of SAM formation on graphene is based on a defect-mediated nucleation, followed by a lateral 2D polymerization that eventually leads to a complete monolayer coverage by a cross-linked and robust 2D siloxane network (model in Figure 3). As opposed to doping by electropositive atoms such as alkali ions,²⁰ SAM doping of graphene exhibits an excellent stability in ambient and high-vacuum environments. The distinct morphology of SAM nucleation suggests that it can be used as a simple technique for visualization or electronic passivation of graphene edges and defects, as well as for complete SAM coverages. Although the mechanism of SAM-induced doping is not yet fully understood, we speculate that free silanol groups (Si-OH) at the SAM-graphene interface might be responsible for a strong protic doping of the surface due to high acidity of the protons. Interestingly, our preliminary measurements show that exposure to polar gases (such as vapors of common solvents) reversibly change the SAM-induced conductivity of graphene, which is very promising for development of novel chemical sensors.

In conclusion, we have synthesized stable self-assembled monolayers of fluoroalkyl silanes at the surface of graphite and graphene, resulting in a strong surface doping effect of graphene with carrier densities in excess of 10^{13} cm^{-2} . Nanoscale imaging and X-ray photoelectron spectroscopy confirm a simple monolayer structure with the predicted stoichiometry. The novel doping approach described here offers the potential for chemical modification of graphene electronic properties using methods of molecular engineering and self-assembly.

Acknowledgment. We thank X. Du, D. Maslov, M. E. Gershenson, and L. C. Feldman for helpful discussions, T. Choi and S.-W. Cheong for access to AFM, and J. Paramanandam for help on SEM imaging. V.P. acknowledges support through NSF-ECCS-0822036 and NSF-DMR-0843985. E.Y.A. acknowledges support through NSF-DMR-0906711.

REFERENCES AND NOTES

- (1) Di Benedetto, S. A.; Facchetti, A.; Ratner, M. A.; Marks, T. J. Molecular Self-Assembled Monolayers and Multilayers for Organic and Unconventional Inorganic Thin-Film Transistor Applications. *Adv. Mater.* **2009**, *21*, 1407–1433.
- (2) Kobayashi, S.; et al. Control of carrier density by self-assembled monolayers in organic field-effect transistors. *Nat. Mater.* **2004**, *3*, 317–322.
- (3) Takeya, J.; et al. Effect of polarized organosilane self-assembled monolayers on organic single-crystal field-effect transistors. *Appl. Phys. Lett.* **2004**, *85*, 5078–5080.
- (4) Campbell, I. H.; Kress, J. D.; Martin, R. L.; Smith, D. L.; Barashkov, N. N.; Ferraris, J. P. Controlling charge injection in organic electronic devices using self-assembled monolayers. *Appl. Phys. Lett.* **1997**, *71*, 3528–3530.
- (5) Calhoun, M. F.; Sanchez, J.; Olaya, D.; Gershenson, M. E.; Podzorov, V. Electronic functionalization of organic semiconductors with self-assembled monolayers. *Nat. Mater.* **2008**, *7*, 84.
- (6) Kuo, C.-Y.; Lee, B.; Wiedlinski, L. S.; Heeney, M.; McCulloch, I.; Grubbs, E.; Feldman, L. C.; Podzorov, V. *Adv. Funct. Mater.* **2009**, *19*, 1906.
- (7) Hydrophobicity, hydrophilicity and silane surface modification, Gelest brochure, www.gelest.com, 2006.
- (8) Castro Neto, A. H.; Guinea, F.; Peres, N. M. R.; Novoselov, K. S.; Geim, A. K. The electronic properties of graphene. *Rev. Mod. Phys.* **2009**, *81*, 109–162.
- (9) Du, X.; Skachko, I.; Barker, A.; Andrei, E. Y. Approaching ballistic transport in suspended graphene. *Nat. Nanotechnol.* **2008**, *3*, 491.
- (10) Vischer, P. B.; Falicov, L. M. *Phys. Rev. B* **1971**, *3*, 2541.
- (11) Serfaty, M. S.; Kopelevich, Y.; de Silva, R.; Torres, J. H. S.; Rettoni, C. *Solid State Commun.* **2002**, *121*, 579.
- (12) Tam, Y. W.; et al. Measurement of Scattering Rate and Minimum Conductivity in Graphene. *Phys. Rev. Lett.* **2007**, *99*, 246803.
- (13) Novoselov, K. S.; et al. Two-dimensional gas of massless Dirac fermions in graphene. *Nature* **2005**, *438*, 197–200.
- (14) Hwang, E. H. Carrier Transport in Two-Dimensional Graphene Layers. *Phys. Rev. Lett.* **2007**, *98*, 186806.
- (15) Chen, J.-H.; et al. Charged-Impurity Scattering in Graphene. *Nat. Phys.* **2008**, *4*, 377–381.
- (16) Adam, S.; Hwang, E. H.; Galitski, V. M.; Das Sarma, S. A self-consistent theory for graphene transport. *Proc. Natl. Acad. Sci. U.S.A.* **2007**, *104*, 18392.
- (17) Allison, D.; Lee, B.; Podzorov, V.; Frittle, C. D. In preparation.
- (18) Wang, X.; Tabakman, S. M.; Dai, H. *J. Am. Chem. Soc.* **2008**, *130*, 8152.
- (19) Sagiv, J. Organized monolayers by adsorption: formation and structure of oleophobic mixed monolayers on solid surfaces. *J. Am. Chem. Soc.* **1980**, *102*, 92.
- (20) Chen, J.-H.; et al. *Nat. Phys.* **2008**, *4*, 377.



Appendix III.

PHYSICAL REVIEW B 82, 085302 (2010)

Origin of the bias stress instability in single-crystal organic field-effect transistors

B. Lee,¹ A. Wan,² D. Mastrogianni,² J. E. Anthony,³ E. Garfunkel,^{2,4} and V. Podzorov^{1,4,*}¹Department of Physics, Rutgers University, Piscataway, New Jersey 08854, USA²Department of Chemistry, Rutgers University, Piscataway, New Jersey 08854, USA³Department of Chemistry, University of Kentucky, Lexington, Kentucky 40506, USA⁴Institute for Advanced Materials, Devices and Nanotechnology, Rutgers University, Piscataway, New Jersey 08854, USA

(Received 23 May 2010; published 3 August 2010)

We report a systematic study of the bias stress effect at semiconductor-dielectric interfaces using single-crystal organic field-effect transistors as a test bed. A combination of electrical transport and ultraviolet photoelectron spectroscopy suggests that this instability is due to a ground-state (i.e., occurring in the dark) charge transfer of holes from the accumulation channel of the semiconductor to localized states of a disordered insulator. The proposed model is not semiconductor specific and therefore provides a general analytical description of this instability in a variety of organic and inorganic band semiconductors interfaced with amorphous insulators.

DOI: 10.1103/PhysRevB.82.085302

PACS number(s): 73.20.AJ, 73.20.Hb, 73.25.+i

The bias stress effect is a longstanding problem in organic and inorganic semiconductor field-effect transistors (FETs) (see, e.g., Ref. 1). Investigation of this phenomenon is not only of practical importance but may also offer insights into fundamentals of energetic structure of semiconductor-dielectric interfaces.² The effect presents itself as a continuous decrease of the current in the channel (or a shift of the threshold voltage) observed under accumulation conditions. Although bias stress effect has been studied in amorphous Si and lately in organic thin-film FETs, disorder present in these materials (e.g., ubiquitous grain boundaries³) leads to a significant charge scattering, trapping, and other nonintrinsic contributions to the transport properties. Several of the proposed mechanisms of the effect (recently reviewed in Ref. 1) are indeed related to extrinsic phenomena, such as, e.g., (a) trapping of holes in the semiconductor's channel, (b) injection of electrons from the gate electrode into the dielectric, (c) ionic conduction in the dielectric, and (d) modification of contacts under the gate bias. While all these effects are important for applications, the question still remains whether there is an intrinsic mechanism of the bias stress instability at well-defined semiconductor-dielectric interfaces without any involvement of ambient environmental factors or trapping in the semiconducting channel. Recently developed highly ordered single-crystal organic field-effect transistors (OFETs) allow us to address this problem.^{4–6} The conclusions drawn from our experiment are not specific only to organic semiconductors and can be applied to any band (semi)conducting material, such as, for example, Si, carbon nanotubes (CNTs), or graphene, interfaced with an amorphous dielectric (SiO₂, high- k oxides or nonconjugated polymers).

In this study, we have investigated the bias stress effect in OFETs based on single crystals of several organic semiconductors: rubrene,⁷ tetracene,⁸ and 6,13-bis(triisopropylsilyl)ethynyl] (TIPS) pentacene,⁹ that have been interfaced with a nonconjugated polymer, parylene, previously used as an insulator in high-performance OFETs.⁴ Investigations of this type of semiconductor-insulator interfaces are critically important because practical organic electronic devices will ultimately rely on inexpensive plastic insulators rather than expensive oxides. Rubrene and tetracene single

crystals have been grown by physical vapor transport (see, e.g., Ref. 4). TIPS-pentacene single crystals have been prepared by crystallization from solution and annealed in a stream of forming gas (100 cc/min) at 120 °C for 4 h before OFET fabrication. Fabrication of optimized devices is described elsewhere.^{4,7} Field-effect mobilities, μ , were obtained from the linear transconductance curves, $I_{SD}(V_G)$ —the dependence of the source-drain current, I_{SD} , on the gate voltage, V_G , at a fixed source-drain voltage, V_{SD} . We have verified that contact resistance effects in our OFETs were negligible before and after gate stressing.

Figure 1 shows the typical bias stress characteristics of our OFETs, i.e., $I_{SD}(t)$ measured in the dark at fixed V_G and V_{SD} . We define the magnitude of the bias stress as $\Delta I/I_0 = [I_0 - I(t)]/I_0$, where I_0 is the initial source-drain current established right after the transistor is on. In rubrene OFETs, the dark bias stress effect is very small; the current decreases by only 5–7 % after a continuous stressing for 6 h at $V_G = -80$ V while in TIPS pentacene and tetracene devices it is typically about 30% and 45%, respectively. Transconductance measurements before and after a prolonged stressing indicate that the slope of $I_{SD}(V_G)$ does not change in any of the studied systems, i.e., the bias stress effect is solely due to a shift of the threshold voltage without changes in μ (inset in the top panel of Fig. 1) and hence measuring $I_{SD}(t)$ is analogous to measuring the threshold voltage shift. In addition, the preserved linear mobility in these two-probe OFETs suggests that the contact resistance is not much affected by the stress.⁷ It is also interesting that the threshold voltage shift can be partially recovered by a prolonged application of a positive V_G . However, complete recovery in these p -type OFETs cannot be achieved because at $V_G > 0$ there is no accumulation channel and hence the electric field at the interface is much weaker than the field at equivalent $V_G < 0$.

Two striking features of the bias stress instability can be seen at Fig. 1. First, the rate and the magnitude of the effect strongly depend on the type of organic semiconductor, rather than on the typical charge-carrier mobility in each system. For instance, although TIPS-pentacene OFETs have $\mu \sim 0.05 \pm 0.01$ cm² V⁻¹ s⁻¹, which is not unusual for solution-grown single crystals with rough facets,^{9,10} the bias

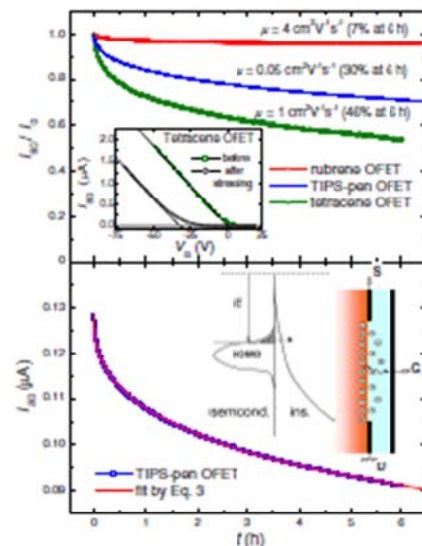


FIG. 1. (Color online). Top: normalized bias stress curves, $I_{SD}(t)/I_0$, of several single-crystal OFETs ($V_G = -80$ V, $V_{SD} = 25$ V, $C_i = 2.35$ nF/cm²). The typical linear field-effect mobilities, μ , and the bias stress values at 6 h of continuous stressing are indicated for each system. The inset shows that the slope of $I_{SD}(V_G)$ does not change after stressing for 6 h. Bottom: the bias stress curve of a TIPS-pentacene OFET fitted with a stretched hyperbola [Eq. (3)]. Similar fits are obtained for the other systems. The inset shows an energy model of the semiconductor-insulator interface: the hole transfer rate depends on the overlap between the semiconductor's HOMO and the exponential tail of localized states of the insulator. The cartoon schematically depicts the transfer and drift of holes in the insulator.

stress effect in these devices is typically smaller than that in tetracene OFETs with $\mu \approx 1$ cm²V⁻¹s⁻¹ (Fig. 1). This trend has been verified in multiple devices measured in our laboratory over the course of several years. Second, all the devices exhibit the same characteristic type of the bias stress curve independently on the overall magnitude of the effect: an initial fast decay of I_{SD} and a subsequent much slower relaxation that can continue for hours or days, as long as V_G is applied.

In the prior studies, such distinct shape has been empirically fitted with a stretched exponent, adopted from amorphous Si transistor research, where the bias stress is believed to be due to dispersive diffusion of hydrogen in α -Si.^{1,11} It is important to note that although a stretched exponential decay provides a satisfactory fit to most of the OFET data,¹ a detailed microscopic model explaining such behavior in organic semiconductors is lacking. It is especially difficult to justify such model in the case of highly ordered molecular

crystals, where the charge transport cannot be described as a dispersive hopping in exponentially distributed trap states, necessary to obtain a stretched exponential dependence.¹

We argue that the leading mechanism of the bias stress instability in our OFETs is a ground-state hole transfer from the field-induced accumulation channel of the organic semiconductor to localized states of the adjacent insulator (sketch at Fig. 1). The transferred holes, located between the accumulation channel and the gate, are screening the gate electric field, so its effective value in the channel becomes $E_G = e n_{ch}(t)/(e \epsilon_0) = (V_G/d) - e n(t)/(e \epsilon_0)$, where e is the elementary charge, ϵ and ϵ_0 are the dielectric permittivities of the insulator and free space, respectively, $n(t)$ is an areal (i.e., two-dimensional) density of the transferred holes, d is the insulator thickness, $n_{ch}(t)$ is the density of mobile holes in the OFET channel that becomes smaller as the result of screening, leading to a decreasing source-drain current: $I_{SD}(t) = (W/L) V_{SD} \mu e n_{ch}(t)$. The density of transferred charge $n(t)$ is related to $n_{ch}(t)$ as $n(t) + n_{ch}(t) = n_0$, where the constant $n_0 = n_{ch}(t=0) = e \epsilon_0 V_G/(e d)$ is the initial density of holes in the channel.

The charge-transfer rate, dn/dt , should be proportional to the density of holes available in the accumulation channel, n_{ch} , and a three-dimensional density of states, δ_0 , in the exponentially distributed tail states of the disordered insulator at an energy matching the semiconductor's highest occupied molecular orbital (HOMO) edge, where holes are accumulated in OFETs (Fig. 1). The magnitude δ_0 depends on the relative position of ionization energies (HIs) of the semiconductor and the insulator, as well as on the extent of the tail states of the latter. In addition, since the process of filling δ_0 states by interfacial charge transfer is fast, the rate of the bias stress effect will be mainly limited by the secondary process—a slow diffusion or drift of the transferred holes away from the interface (toward the gate), as the result of which some of the insulator's states near to the interface become empty and available again for further hole transfer. Therefore, dn/dt must be proportional to the sum of diffusion and drift fluxes of holes in perylene, $j_{diff} \sim D_{im} \cdot \delta_0/\lambda_0$, and $j_{drift} \sim \delta_0 \cdot v_{drift} = \delta_0 \cdot \mu_{im} \cdot E_G = \delta_0 \cdot \mu_{im} \cdot e n_{ch}(t)/(e \epsilon_0)$, where D_{im} is a diffusivity of holes in the insulator, λ_0 is a characteristic width of the spatial distribution of holes in the insulator near the interface, $v_{drift} = \mu_{im} \cdot E_G$ is a drift velocity of holes with hopping mobility μ_{im} in the insulator near the interface. μ_{im} in nonconjugated insulators is extremely small and to the first approximation does not show a Poole-Frenkel dependence because of (a) relatively small E_G used in our study and (b) undoped and nonpolar nature of perylene without spatial correlations of energetic disorder.¹² Hence, the charge-transfer rate can be expressed as $dn/dt = -dn_{ch}/dt = \chi_0 \cdot n_{ch} \cdot (j_{diff} + j_{drift})$ or

$$dn_{ch}/dt = -\chi_0 n_{ch} (D_{im} \delta_0/\lambda_0 + \delta_0 \mu_{im} E_G), \quad (1)$$

where χ_0 is a cross section of the charge-transfer process in square centimeters.

Dispersive transport in virtually all disordered systems with an exponential distribution of band tails universally exhibits a power-law time dependence of diffusivity and mobility, $D_{im} = D_0 \cdot (t/\tau_{im})^{\beta-1}$ and $\mu_{im} = \mu_0 \cdot (t/\tau_{im})^{\beta-1}$, where τ_{im}

is the characteristic trapping time in the insulator ($1/\tau_{\text{ins}}$ is the hopping rate) at the transport energy level (not to be confused with HOMO edge), and $\beta = T/T_0 < 1$ is a dispersion exponent related to the characteristic width of the band tail of the insulator.^{13,14} Hence we can rewrite Eq. (1) as

$$\frac{dn_{\text{ch}}}{dt} = -\chi_0 \cdot (t/\tau_{\text{ins}})^{\beta-1} \cdot [D_0(\delta_0/\lambda_0) \cdot n_{\text{ch}} + \delta_0 \mu_0 e / (\epsilon \epsilon_0) \cdot n_{\text{ch}}^2]. \quad (2)$$

Note that if the charge motion in the insulator is dominated by diffusion ($j_{\text{diff}} \gg j_{\text{drift}}$), the rate of the bias stress effect will be proportional to n_{ch} or V_G , and the solution of Eq. (2) will be a stretched exponent, $n_{\text{ch}}(t) = n_0 \exp[-(t/\tau)^\beta]$, where τ is a renormalized V_G -independent time constant $\tau = \tau_{\text{ins}} \cdot [\lambda_0 \beta / (\chi_0 D_0 \delta_0 \tau_{\text{ins}})]^{1/\beta}$. However, if the process is dominated by drift ($j_{\text{drift}} \gg j_{\text{diff}}$), dn/dt will be proportional to n_{ch}^2 or V_G^2 and the analytical solution of Eq. (2) for the source-drain current $I_{\text{SD}} = (W/L)V_{\text{SD}}\mu e n_{\text{ch}}$ is a stretched hyperbola

$$I_{\text{SD}}(t) = \frac{I_0}{1 + (t/\tau)^\beta}, \quad \tau = \tau_{\text{ins}} \cdot \left(\frac{\beta d}{V_G \chi_0 \mu_0 \delta_0 \tau_{\text{ins}}} \right)^{1/\beta}, \quad (3)$$

where $I_0 = I_{\text{SD}}(t=0)$ is the initial current in the channel and τ is a renormalized V_G -dependent time constant. In both cases, the time constant τ increases as $(1/\delta_0)^{1/\beta}$ for interfaces with a smaller energetic overlap δ_0 , because $\beta > 0$.

In our experimental situation, the hole motion in the insulator is drift limited. Indeed, we have estimated that the ratio $j_{\text{diff}}/j_{\text{drift}} = (\lambda_0 \mu_0 V_G) / (D_0 d) = (e V_G / k_B T) \cdot (\lambda_0 / d) \sim 10-30 \gg 1$, with $D_0 = k_B T \mu_0 / \hbar$ (k_B is the Boltzmann constant), and $\lambda_0 \sim 3-10$ nm—a reasonable lower limit of the distance at which holes are injected into the perylene. Moreover, we have confirmed the drift-limited regime experimentally by measuring the actual dependence of the bias stress rate, dI_{SD}/dt , on V_G in a number of nominally identical rubrene transistors (Fig. 2). The inset in Fig. 2 shows that the bias stress effect is indeed greater at a higher V_G , and the rate follows a V_G^2 dependence (the lower panel), as expected from Eq. (2) in this regime. In addition, fitting the four curves in the inset with a stretched hyperbola [Eq. (3)] yields a V_G -dependent τ and a value of $\beta = 0.3 \pm 0.05$. According to Eq. (3), τ should be proportional to $(1/V_G)^{1/\beta}$. Plotting $\ln(\tau)$ vs $\ln(1/V_G)$ for this set of devices indeed results in a linear dependence with a slope consistent with $\beta \sim 0.3$ (the upper panel of Fig. 2).

A stretched hyperbola [Eq. (3)] provides a perfect fit to all of the studied systems (for simplicity, the lower panel of Fig. 1 shows only the fit for TIPS-pentacene OFET). It is worth noting that τ and β obtained by fitting these systems are consistent with the underlying physics of the effect. Indeed, τ decreases in the order: rubrene (49.5×10^6 s), TIPS-pentacene (0.177×10^6 s) and tetracene (0.031×10^6 s), consistent with the bias stress rate increasing in this order and implying that δ_0 is also increasing in the same order [we confirm this trend below by ultraviolet photoemission spectroscopy (UPS)]. However, the exponent β in this set is found to be almost constant: $\beta = 0.37 \pm 0.05$.

According to our model, organic transistors with a greater energetic overlap between HOMO and localized states of the insulator should exhibit a stronger bias stress effect (Fig. 1).

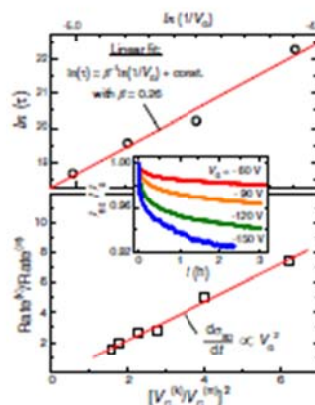


FIG. 2. (Color online). Bias stress effect in rubrene OFETs measured at different V_G (inset). Top: V_G dependence of the time constant τ , obtained for the four curves by stretched hyperbola fits [Eq. (3)]. Bottom: ratio of the bias stress rates measured at different V_G and plotted as a function of V_G ratios squared. Red line is a linear fit.

In order to test this idea, we have performed UPS studies of ionization energies (IIs) of the organic crystals and the insulator used in this study (Fig. 3) (details of UPS technique can be found elsewhere¹⁵). II₁ refers to position of the HOMO edge with respect to the vacuum level (i.e., it is an energetic position of holes in the accumulation channel in p -type OFETs). The IIs of rubrene, TIPS-pentacene, tet-

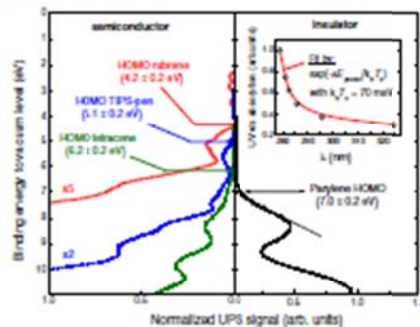


FIG. 3. (Color online) Left: UPS spectra of crystalline rubrene (red), TIPS-pentacene (blue), and tetracene (green). Photoemission onsets (i.e., HOMO edges or II₁) are shown with the arrows. Right: UPS spectrum of an ultrathin (10 ± 2 nm) perylene N on gold. The inset is a UV-visible optical-absorption spectrum of perylene N, showing a ~ 1.5 -eV-wide tail of states below the 280 nm absorption edge.

racene, and parylene are 4.2 ± 0.2 eV, 5.1 ± 0.2 eV, 6.2 ± 0.2 eV, and 7.0 ± 0.2 eV, respectively. Despite a considerable difference between the HOMOs of the organic semiconductors and parylene, the exponential tail states of the latter (seen above 7 eV in Fig. 3) allow for a small charge transfer. A better evidence of the extended in-gap tail states of parylene is provided by the UV-visible absorption of this material (inset in Fig. 3). As expected, the absorption edge (280 nm) considerably tails into the band gap. Fitting this tail with an exponential distribution yields $k_B T_0 \sim 70$ meV, in a good agreement with a room-temperature value of $\beta = 1/T_0 \sim 0.37$. The relative positions of the semiconductor's and the insulator's HOMOs determined from our UPS are consistent with the observed trend for the rate of the bias stress effect to increase for semiconductors with a "deeper" HOMO.

It is worth noting that vacuum-gap OFETs exhibit a negligible bias stress, provided that there are no polar molecules in the residual gas in the gap. However, these devices do show a bias stress effect of a different kind that occurs as a result of an introduction of polar molecules in a gaseous form in the gap (e.g., acetone or water vapor), resulting in the effect proportional to the dipole moment of the molecules due to the gate-induced polarization of the vapor.

Most of the extrinsic factors contributing to bias stress can be ruled out in our devices. For example, charge trapping in the accumulation channel cannot be the primary cause because there are examples of OFETs with a high trap density (low μ) that nevertheless show noticeably smaller bias stress effect than other devices with a much greater μ . The influence of water at the interface or in the dielectric can also be ruled out because it would not result in a systematic dependence of the effect on the HOMO energy. In addition, (a)

we have tested that *in situ* annealing of the samples at moderate temperatures in vacuum before parylene deposition does not influence the effect and (b) we have used macroscopic grain-boundary free organic crystals encapsulated in a nonhygroscopic parylene deposited in vacuum and capped with a 50-nm-thick Ag gate. Hence, postfabrication water permeation would be highly unlikely. Finally, an injection of electrons from the metal gate into the insulator in our OFETs is excluded because of the outstanding insulating properties of parylene revealed in *I-V* measurements of Ag/parylene/Ag sandwich structures, showing a typical insulating behavior with a very large resistivity, $\rho > 100$ G Ω for up to ± 200 V.

To conclude, we have systematically studied the (dark) bias stress instability in OFETs based on rubrene, tetracene, and TIPS pentacene interfaced with an amorphous polymer insulator. A combination of charge transport and UPS measurements suggests that the effect is due to a transfer of holes from the accumulation channel of the semiconductor to localized states of the insulator. The effect is smaller in systems with a greater energetic mismatch between the HOMO edges of the semiconductor and the insulator. Our model only relies on the concepts of semiconductor's ionization energy and exponential band tails of disordered insulators and hence it could be used to understand instabilities in a wider range of semiconductor devices, including organic, inorganic, CNT, and graphene FETs.

This work has been financially supported by NSF under Grants No. ECCS-0822036 and ARRA CAREER No. DMR-0843985 and Industrial Technology Research Grant Program 09E510076 (NEDO).

*Corresponding author: podzorov@physics.rutgers.edu

¹H. Sirringhaus, *Adv. Mater.* **21**, 3859 (2009).

²D. Cahen, A. Kahn, and E. Umbach, *Mater. Today*, **8**, 32 (2005).

³K. Pantambekar, J. Dong, G. Haugstad, and C. Daniel Frittle, *Adv. Funct. Mater.* **16**, 879 (2006).

⁴R. W. I. de Boer, M. E. Gerstenson, A. F. Morpurgo, and V. Podzorov, *Phys. Status Solidi* **291**, 1302 (2004).

⁵J. Takeya, T. Nishikawa, T. Takenobu, S. Kobayashi, Y. Iwasa, T. Mitani, C. Goldmann, C. Krellner, and B. Balogh, *Appl. Phys. Lett.* **85**, 5078 (2004).

⁶A. L. Briseno, R. J. Tseng, M.-M. Ling, E. H. L. Falcão, Y. Yang, F. Wudl, and Z. Bao, *Adv. Mater.* **18**, 2320 (2006).

⁷V. Podzorov, S. E. Sysoev, E. Logunova, V. M. Pudalov, and M. E. Gerstenson, *Appl. Phys. Lett.* **83**, 3504 (2003).

⁸M. F. Calhoun, C. Hsieh, and V. Podzorov, *Phys. Rev. Lett.* **98**,

096402 (2007).

⁹J. G. Park, R. Vasic, J. S. Brooks, and J. E. Anthony, *J. Appl. Phys.* **100**, 044511 (2006).

¹⁰S. Subramanian, S. K. Park, S. R. Parkin, V. Podzorov, T. N. Jackson, and J. E. Anthony, *J. Am. Chem. Soc.* **130**, 2706 (2008).

¹¹W. B. Jackson, J. M. Marshall, and M. D. Moyer, *Phys. Rev. B* **39**, 1164 (1989).

¹²Y. N. Gartstein and E. M. Conwell, *Chem. Phys. Lett.* **245**, 351 (1995).

¹³D. Monroe, *Phys. Rev. Lett.* **54**, 146 (1985).

¹⁴H. Scher and E. W. Montroll, *Phys. Rev. B* **12**, 2455 (1975).

¹⁵A. Kahn, N. Koch, and W. Gao, *J. Polym. Sci., Part B: Polym. Phys.* **41**, 2529 (2003).

Appendix IV.

Doping of Conjugated Polythiophenes with Alkyl Silanes

By Chi Yueh Kao, Bumsu Lee, Leszek S. Wielunski, Martin Heeney, Iain McCulloch, Eric Garfunkel, Leonard C. Feldman, and Vitaly Podzorov*

A strong modification of the electronic properties of solution-processable conjugated polythiophenes by self-assembled silane molecules is reported. Upon bulk doping with hydrolyzed fluoroalkyl trichlorosilane, the electrical conductivity of ultrathin polythiophene films increases by up to six orders of magnitude, reaching record values for polythiophenes: $(1.1 \pm 0.1) \times 10^3 \text{ S cm}^{-1}$ for poly(2,5-bis(3-tetradecylthiophen-2-yl)thieno[3,2-b]thiophene) (PBTtT) and $50 \pm 20 \text{ S cm}^{-1}$ for poly(3-hexylthiophene) (P3HT). Interband optical absorption of the polymers in the doped state is drastically reduced, making these highly conductive films transparent in the visible range. The dopants within the porous polymer matrix are partially crosslinked via a silane self-polymerization mechanism that makes the samples very stable in vacuum and nonpolar environments. The mechanism of SAM-induced conductivity is believed to be based on protonic doping by the free silanol groups available within the partially crosslinked SAM network incorporated in the polythiophene structure. The SAM-doped polythiophenes exhibit an intrinsic sensing effect: a drastic and reversible change in conductivity in response to ambient polar molecules, which is believed to be due to the interaction of the silanol groups with polar analytes. The reported electronic effects point to a new attractive route for doping conjugated polymers with potential applications in transparent conductors and molecular sensors.

1. Introduction

Molecular self-assembly is a surface modification technique that can be used in emerging applications in organic and molecular electronics.^[1–4] The self-assembly of silanes has recently been observed at the surface of organic semiconductors, which opens new opportunities for fundamental and applied research.^[4] Our primary interest stems from the observation of a large increase in conductivity induced by a self-assembled monolayer (SAM) deposited on the surface of organic single crystals. Here, we extended our studies of SAM-functionalized organic semiconductors to a class of solution-processable conjugated polythiophenes,^[5–6] and we demonstrate how the interaction of these polymers with hydrolyzed fluoroalkyl trichlorosilane (FTS) resulted in a drastic modification of the electrical and optical properties of these semiconducting polymers. Upon doping with FTS, the electrical conductivity of ultrathin polythiophene films increased by up to six orders of magnitude, reaching $(1.1 \pm 0.1) \times 10^3 \text{ S cm}^{-1}$ for poly(2,5-bis(3-tetradecylthiophen-2-yl)thieno[3,2-b]thiophene) (PBTtT) and $50 \pm 20 \text{ S cm}^{-1}$ for poly(3-hexylthiophene) (P3HT); the corresponding average sheet conductivities were 2.2 and 0.1 mS sq^{−1}. Simultaneously, interband optical absorption was drastically reduced, making these conducting films transparent in the visible range of the spectrum. These effects point to an attractive new route of doping conjugated polymers and could lead to the observation of interesting polaron–polaron interaction phenomena in the regime of very high carrier densities. In addition, FTS-doped polythiophenes exhibit interesting molecular sensorial properties that make this solution-processable system very attractive for electronic sensors, including artificial nose applications.

Current efforts in SAM research have been primarily focused on two experimental platforms: SAM deposited on inorganic conductors and semiconductors (e.g., noble metals, Si, Ge)^[10–13] and SAM on oxide insulators (e.g., SiO₂).^[13,14,15] SAM deposition is used to modify the work function of these materials, to functionalize the surface enabling the attachment of other chemical or biological species (e.g., for sensors), and to fabricate

[*] Prof. V. Podzorov, C. Y. Kao,^[†] B. Lee, Dr. L. S. Wielunski
Department of Physics, Rutgers University
Piscataway, NJ 08854 (USA)
E-mail: podzorov@physics.rutgers.edu

Prof. M. Heeney
Department of Materials, Queen Mary University of London
London, E1 4NS (UK)

Prof. I. McCulloch
Department of Chemistry, Imperial College London
London, SW7 2AZ (UK)

Prof. E. Garfunkel
Department of Chemistry, Rutgers University
Piscataway, NJ 08854 (USA)

Prof. E. Garfunkel, Prof. L. C. Feldman
Institute of Advanced Materials, Devices, and Nanotechnology
Rutgers University
Piscataway, NJ 08854 (USA)

[†] Present address: Department of Chemistry, The Ohio State University,
Columbus, OH 43210-1117 (USA)

DOI: 10.1002/adfm.200900120

molecular components of organic field-effect transistors (OFETs) and other electronic devices (e.g., to improve structural and/or electronic properties of organic thin films).

The recent observation of molecular self-assembly at the surfaces of small-molecule organic crystals broadens the range of materials of interest for SAM research.^[6] A dense SAM of silanes can be formed at the surface of p-type molecular crystals, e.g., rubrene or tetracene. In contrast to SAMs on Au or SiO₂, those at the surface of organic semiconductors can drastically modify the electrical conductivity of these materials. (Tridecafluoro-1,1,2,2-tetrahydrooctyl)trichlorosilane (C₁₃H₉F₁₁SiCl₃), or simply FTS, grown at the surface of rubrene induces a remarkably high conductivity, as high as $\sigma_{\square} \approx 10^{-5} \text{ S sq}^{-1}$, which is about two orders of magnitude greater than the sheet conductivities typically achieved by electrostatic doping in OFETs. The effect is thought to be due to mobile holes induced by the SAM in the top layer of the highly ordered molecules in the organic crystals.

2. Results and Discussion

Conjugated polymers are complementary solution-processable semiconducting materials with intriguing optoelectronic properties.^[7,8,14] The electronic state of these materials can be tuned from insulating to conducting by changing the carrier concentration via chemical doping or injection from contacts in an OFET geometry.^[17–20]

In this work, we performed FTS functionalization of thin films of P3HT and PBTBT and observed that exposure to FTS introduced mobile carriers into these conjugated polymers, rendering the samples highly conducting. The experiment was performed using spin-coated polymer films prepared on glass according to optimized procedures reported in the literature.^[19,20] FTS doping was performed from the vapor phase, following a similar process that was used to grow SAMs on molecular crystals.^[6] For specific details of sample preparation and doping, see the Experimental Section. As shown in Figure 1, when a film of P3HT or PBTBT with a thickness of 20 nm was exposed to FTS vapors, the conductivity rapidly increased and reached $\sigma_{\square}^{\text{P3HT}} = 30 \text{ S sq}^{-1}$ and $\sigma_{\square}^{\text{PBTBT}} = 1100 \text{ S sq}^{-1}$ in a saturated doping state; the corresponding sheet conductivities were $\sigma_{\square}^{\text{P3HT}} = 0.6 \times 10^{-4} \text{ S sq}^{-1}$ and $\sigma_{\square}^{\text{PBTBT}} = 2.2 \times 10^{-3} \text{ S sq}^{-1}$. The effect was stable in high vacuum and under an atmosphere of nonpolar gases, including oxygen. Contrary to densely packed molecular crystals, where the SAM growth is restricted to the surface, FTS molecules penetrate deep into the nanoporous polymeric materials, interact with the surface of individual nanocrystalline domains, and dope the entire film. This behavior could be detected using different methods and was most strikingly observed by a strong suppression of interband optical absorption of the polymer, which made the samples almost completely transparent (Fig. 2).

In order to characterize this “bleaching” effect, we measured optical absorption of FTS-doped samples (Fig. 3). The pristine samples exhibited a broad interband absorption peak at $\sim 560 \text{ nm}$ (2.21 eV), as expected (curve 1). Both the P3HT and PBTBT samples exhibited vibronic bands, indicating high structural order in the samples. The vibronic bands are more obvious in the P3HT spectrum, where they are separated by $0.16 \pm 0.02 \text{ eV}$, in agreement with the 1450 cm^{-1} Raman stretching mode of the C=C bond. Once doped with FTS to the maximum conductivity,

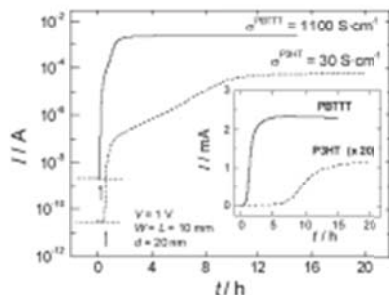


Figure 1. Time evolution of the current (I) through ultrathin P3HT and PBTBT films as the samples were exposed to the saturated FTS vapor. The arrows indicate when the vapor was introduced into the test chamber. The inset shows the same data on a linear scale. P3HT and PBTBT thin films were spin-coated on glass; the film thickness was 20 nm; the contacts were made of colloidal graphite; the width and length of the channel were $W = L = 1 \text{ cm}$; the applied dc bias was 1 V.

the interband optical absorption of the samples was almost completely suppressed (curve 2), while another broad long-wavelength band appeared simultaneously at $\lambda \geq 800 \text{ nm}$. Interestingly, if the samples were exposed to ambient air, their absorption spectra, the original purple color, and the initial high electrical resistivity recover within days in the dark or within hours under ambient illumination (curves 3, 4, and 5). At the end of this recovery process, the samples reached the initial insulating state with σ and λ_{max} similar to the pristine polymers, suggesting that the doping/dedoping cycle did not damage the conjugated backbone of the polymer. As will be shown below, this dedoping was not due to the evaporation of FTS molecules from the sample, but rather it was an electronic effect.

Atomic force (AFM) and scanning electron microscopy (SEM) imaging showed that when FTS was incorporated into the sample there was an increase in roughness resulting in a bumpy surface morphology for the doped films (swelling due to the possible self-polymerization of FTS in the polymer matrix (Fig. 4). This is consistent with the permeable nanoporous structure of the polymers, confirming the bulk character of the doping in this case. Interestingly, the AFM images of freshly doped and dedoped samples are very similar. This indicates that FTS molecules were likely not physically removed from the samples during dedoping, and the primary role of dedoping was to “switch off” the conducting state. Another indication that FTS molecules did not “escape” from the polymer film was the high stability of the conducting state during long-term storage under high vacuum. SEM images of pristine and dedoped insulating samples could not be obtained due to sample charging.

We observed that highly conductive FTS-doped polythiophenes exhibited interesting sensing properties. Figure 5 shows the dark conductivity response of an FTS-doped P3HT film to vapors of acetone, water, and hexane. An immediate and large ($\sim 100\%$) decrease of conductivity was observed on exposure to saturated acetone vapor. The conductivity recovered readily on vapor

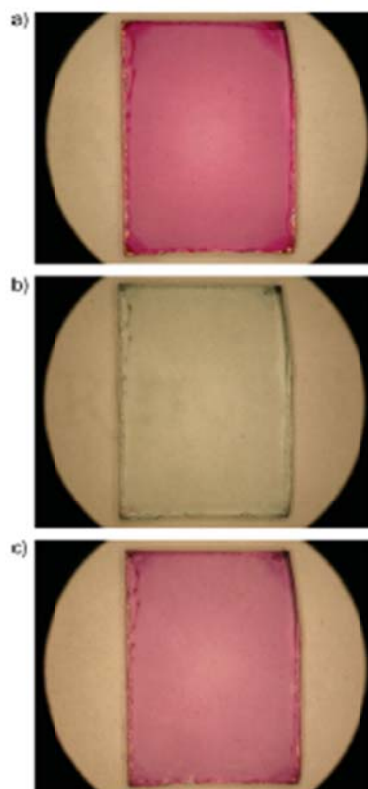


Figure 2. Photographs of a PBTT film with a thickness of 20 nm spin-coated onto a 1 cm \times 1.5 cm glass slide: a) as-spun insulating film, b) doped with FTS to saturation (highly conductive), and c) restored (dedoped) in air under ambient illumination for 16 h (insulating).

removal by pumping. A similar, but smaller in magnitude, response was observed with H₂O vapor. Hexane, which is nonpolar, did not have any effect on the conductivity. Interestingly, this behavior is similar to the sensing effect observed in FTS-coated rubrene, which suggests that the sensing mechanisms in these two systems have a common origin likely related to the dipolar interaction of analytes with FTS.^{6f} In the case of conjugated polymers, however, their solution-processability, availability of large-area samples, and mechanical flexibility make SAM-functionalized polymers especially attractive for applications.

In order to understand the dedoping effect (i.e., the recovery of optical and electrical properties, when FTS-doped polythiophenes

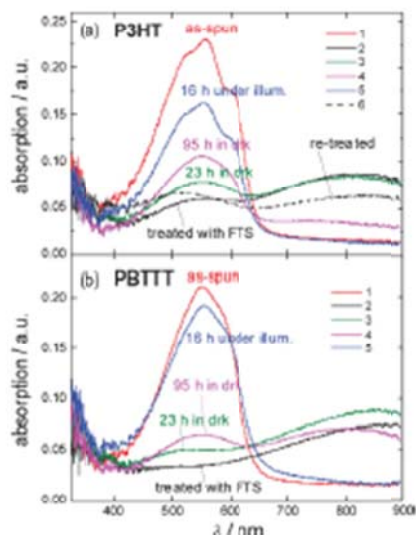


Figure 3. UV-vis absorption spectra of ultrathin films of a) P3HT and b) PBTT. A drastic reduction of absorption is evident after FTS doping. The curves are renumbered as follows: 1 (red): as-spun annealed films, 2 (black): treated with FTS to saturation, 3 (green): dedoped in air in the dark for 23 h, 4 (pink): dedoped in air in the dark for 95 h, 5 (blue): dedoped in air under illumination with a white light for 16 h, 6 (dashed line): dedoped again with FTS after dedoping.

are exposed to air), we exposed highly conducting FTS-doped P3HT samples to various ultra-high purity (UHP) gases in the dark and under illumination while monitoring the conductivity (Fig. 6). Illumination was performed using white light with a smooth spectrum in the visible range (a 20 W quartz-tungsten-halogen lamp). Intensities were kept sufficiently low to avoid radiative heating of the sample. We observed that inert gases (e.g., Ar and He) and nonpolar gases present in air (O₂ and N₂) have no effect on the conductivity of FTS-doped polymers: there is only a very slow, gas-independent drift of σ at a very slow rate of $\sim 0.3\%$ h⁻¹ (the initial portion of the curve in Fig. 6).

However, when saturated water vapor was introduced into the test chamber, an obvious decay of σ occurred. Under illumination, this decay proceeded much faster, with the rate proportional to the illumination intensity (inset in Fig. 6). Instantaneous changes in light intensity resulted in almost instantaneous changes in the decay rate; the inset in Figure 6 shows that reducing the illumination intensity by a factor of 4 caused the decay rate to decrease by a factor of ~ 4 , which produces a kink-like feature in the curve of the time-dependent current. This indicated that dedoping under illumination is a photo-induced electronic effect, rather than an artifact of the sample heating under illumination. Overall, this experiment showed that the analyte

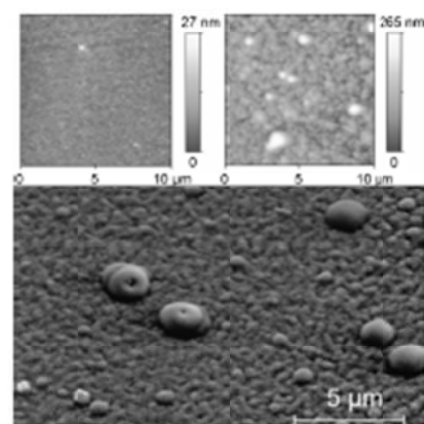


Figure 4. AFM image of pristine P3HT (top left) and FTS-doped P3HT (top right) films, and an SEM image of an FTS-doped P3HT film (bottom). An SEM image of pristine P3HT samples could not be reliably obtained because of severe charging issues with nonconducting samples. Both AFM and SEM images show swelling of the polymer after FTS-doping. Dedoped (recovered) samples exhibited the same swelled morphology identical to the freshly doped films, suggesting that FTS molecules were not removed from doped films.

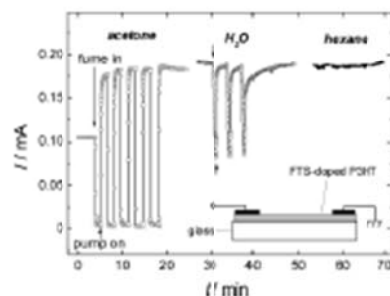


Figure 5. Conductivity response of FTS-doped P3HT films to polar analytes (sample geometry is shown schematically). When the sample was exposed to saturated vapors of polar solvents, the conductivity rapidly decreased; it fully recovered on vapor removal by pumping. The greatest and fastest response was observed for highly polar vapors (e.g., acetone). There was no sensitivity to nonpolar molecules (e.g., hexane). Measurements were carried out at an applied voltage of 1 V in the dark.

responsible for dedoping these samples in air is H_2O , in agreement with the humidity-related degradation of p-type conductivity observed in polythiophene FETs.^[20] The sensing effect shown in Figure 5 can be more generally interpreted as reversible dedoping caused by polar molecules. Full reversibility

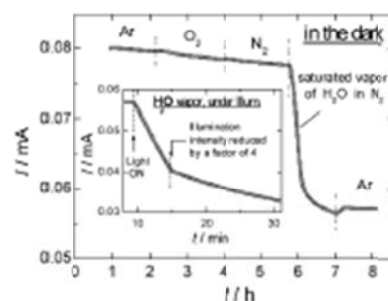


Figure 6. Effect of exposure to various gases on the conductivity of FTS-doped P3HT films, measured in the dark (main panel) and under illumination with white light (inset). H_2O vapor was the main cause of conductivity decrease in air. The decay rate increased under the illumination.

of this effect indicated that volatile analyte molecules were easily removed from the sample by pumping, while FTS molecules remained in the film. This suggests that the molecules of polar solvents were more weakly absorbed in the sample, while FTS molecules were bound to the polymer much more strongly.

The conductivities that we obtained by doping polythiophenes with fluoroalkyl silanes are among the highest previously obtained in this class of polymers using small-sized dopants, such as I_2 , PF_6^- , and CD_3 .^[8,14,18,22] The saturation conductivities of our optimized samples are $\sigma_{\text{P3HT}}^{\text{SAT}} = 70 \text{ S cm}^{-1}$ and $\sigma_{\text{P3HT}}^{\text{PVT}} = 1300 \text{ S cm}^{-1}$ (i.e., $\sigma_{\text{P3HT}}^{\text{PVT}} = 1.4 \times 10^{-4} \text{ S sq}^{-1}$ and $\sigma_{\text{P3HT}}^{\text{PVT}} = 2.2 \times 10^{-3} \text{ S sq}^{-1}$). Typically, polymer samples doped with small ions and molecules display relatively poor stability (especially in vacuum), because of the rapid diffusion of small-sized dopants in the polymer matrix. On the contrary, the FTS-doped samples exhibited remarkable stability: the conductivity did not show any decay in high vacuum and only a very minor drift ($\sim 0.5\% \text{ h}^{-1}$) in an atmosphere of nonpolar gases. It is important to emphasize that doping in our experiment was performed at a solid/vapor interface, using highly ordered polythiophene films, which allowed the use of the well-characterized structural, morphological and transport properties of these polymers as a starting point for data analyses.^[10,23] The above σ values were calculated using the thickness of undoped films ($20 \pm 1 \text{ nm}$). Despite some degree of swelling that occurred on doping, these estimates are justified because silane molecules are not conducting even in the cross-linked state, and therefore, the total number of conjugated chains in the cross-section of the film (the conducting channels) remained roughly the same as that before doping.

Although the nature of silane-polythiophene chemical interaction is not clear at this stage of investigation, the stability of the doped state in high vacuum points to a relatively strong interaction. Our X-ray photoelectron spectroscopy (XPS) and Rutherford back scattering (RBS) data show that there was virtually no chlorine present in the films after vapor-phase FTS doping,^[24] which suggests that the FTS has hydrolyzed *in situ*, either as a result of water trapped in the polymer film or water vapor present in the doping chamber.^[25] Such hydrolyzed silanes

are known to readily self-condense and polymerize to form partially cross-linked siloxane polymers.^[14,15] On silicon dioxide surfaces, these can bind to the free surface hydroxyl groups to form monolayers. In the present case, we believe the FTS was to form into a nonvolatile, partially cross-linked siloxane polymer within the film, accounting for the high stability of the samples under vacuum. In addition, low-concentration oxygen defects known to be present in polythiophenes might serve as anchoring sites for hydrolyzed FTS.^[17] The mechanism of the doping of the conjugated polymer by FTS is unclear, but it may be similar to the mechanism of SAM-induced surface conduction in small-molecule organic crystals, where an electronegative SAM molecule induces an electron transfer across the SAM-crystal interface.^[6] Additionally, free silanol groups [Si(OH)] within the partially cross-linked siloxane are known to exhibit relatively high acidities;^[18] they may result in protonic (acid) doping of the organic semiconductor.

To fully understand the mechanism of FTS incorporation and functioning, nanoscale structural details of FTS-polythiophene samples should be investigated. For instance, one of the intriguing questions is whether FTS molecules break apart individual π - π stacked crystalline nanofibrils and domains, known to constitute P3HT and PHTTT films,^[19,20,26,40] or if they merely bind to the surface of these crystallites. The monolayer character of FTS on molecular crystals and the very high (nearly metallic) conductivity of FTS-doped polythiophenes point to the latter scenario, in which the π - π stacking required for good charge transport is preserved.

Understanding the detailed chemical structure and composition of these functionalized electronic materials is very important. We used ion scattering spectroscopy and XPS to study the elemental composition of FTS-doped polythiophene films.^[41] Our preliminary data indicate that fully doped samples contain approximately one FTS molecule per thiophene ring, with an areal density of fluorine atoms of $11.7 \times 10^{15} \text{ cm}^{-2}$, which corresponds to the 3D density of FTS molecules, $n_{\text{FTS}} = 4.5 \times 10^{21} \text{ cm}^{-3}$, associated with the 13F atoms per FTS molecule. Using simple conductivity arguments ($\sigma = en\mu$), in which $\sigma = 70 \text{ S cm}^{-1}$ is the 3D saturated conductivity of doped P3HT, e is elementary charge, and $\mu \sim 0.1 \text{ cm}^2 \text{ V}^{-1} \text{ s}^{-1}$ is a typical hole mobility in P3HT,^[21,24] the density of FTS-induced holes can be estimated: $n_h = 4.4 \times 10^{18} \text{ cm}^{-3}$, which is comparable to the very high carrier density induced in P3HT by electrolyte gating.^[6] Quantitative agreement between the density of FTS molecules and that of charge carriers doped into the system obtained by the two independent techniques (ion scattering and conductivity) suggests that on average, one hole was doped into the polymer per FTS molecule. The very large doping level (approximately one hole per thiophene ring), the very good stability of the conducting state in high vacuum, and the lack of chlorine in the XPS and RRS spectra indicate that the doping effect was due to hydrolyzed FTS.

Our experiment clearly shows that the dedoping of SAM-polythiophene samples in air was caused by water vapor. More generally, this indicates that dedoping can be deliberately induced by exposing the samples to vapors of polar analytes, such as ketones, alcohols or water. In the dark, dedoping is fully reversible, which is beneficial for the development of electrical chemosensors. One explanation for this effect is that it is caused by conformational changes of the polymer backbone induced by a

dipolar interaction of fluoroalkyl SAM molecules with polar analytes. Such conformational changes are known to effectively reduce the conjugation length of polymers and affect their physical properties.^[9,11] Alternatively, polar analytes would be expected to interact strongly with the free silanol groups within the siloxane backbone formed *in situ*, which might reverse the protonic doping effect and switch off the conducting state. Understanding the actual mechanism of this effect requires further studies.

It has been shown that due to the nondegenerate ground state of polythiophenes, the lowest-energy excitation in these polymers involves the formation of a bipolaron, that is, two solitons on a conjugated chain attracted to each other and creating a weakly localized pair.^[12] Prior studies of optical absorption of P3HT have shown that the interband transition of pristine (undoped) polymer centered at 2.2 eV (560 nm) decreases upon dilute doping with LiClO₄ and NOPF₆, with a simultaneous appearance of two new broad absorption bands at 0.4 eV ($\sim 3 \mu\text{m}$) and 1.6 eV ($\sim 800 \text{ nm}$) indicative of bipolaron formation.^[12,13] The two new bands correspond to optical transitions from the highest occupied molecular orbital (HOMO) to the new gap states associated with bipolarons. An increase of doping to the highest concentration (saturation doping) leads to a complete "bleaching" (suppression) of the interband transition and transformation of the bipolaronic bands into a very broad low-energy shoulder in the absorption spectrum, which corresponds to delocalized polarons in highly conducting samples. The absorption spectrum approaches that of a metal with free carriers.^[42] Similar effects have been observed in doped polyaniline.^[9,43] In our case, the spectral range of our apparatus did not allow the observation of the full evolution of bipolaronic bands. Nevertheless, the drastic suppression of the interband absorption at 560 nm ($\sim 2.2 \text{ eV}$) and the appearance of the broad long-wavelength peak at $\lambda > 650 \text{ nm}$ ($< 1.9 \text{ eV}$) shown in Fig. 3 are both consistent with prior studies and indicate that FTS-doping of P3HT and PHTTT results in a metallic-like state with a high density of mobile polarons. Interestingly, calculations predict that wavefunctions of polarons and bipolarons should significantly overlap at these high carrier densities, which might lead to the formation of "polaron or bipolaron lattices."^[44]

Studies of temperature-dependent conductivity, the Hall effect, IR absorption, and surface analysis are underway in order to elucidate the details of the conduction mechanism and chemical structure of the SAM-polythiophene system. Particularly, IR spectroscopy has been proven to be very useful for the studies of polarons in polythiophene films,^[13] polymer OFETs,^[45] and small-molecule crystalline OFETs.^[46] For instance, the position of the polaronic peak in the mid-IR range is associated with the polaron relaxation energy, and therefore, is indicative of the degree of order in polymer chains.^[47]

3. Conclusion

To summarize, we have demonstrated that the interaction of ultrathin solid films of polythiophenes with the vapors of hydrolyzed fluoroalkyl trichlorosilanes results in a drastic increase of the electrical conductivity and a strong suppression of interband optical absorption of these polymers. Upon doping with fluoroalkyl silanes, the electrical conductivity

increased by up to six orders of magnitude, reaching $(1.1 \pm 0.1) \times 10^4 \Omega^{-1} \text{cm}^{-1}$ in poly(thieno-thiophenes) and $50 \pm 20 \Omega^{-1} \text{cm}^{-1}$ in poly(3-hexylthiophene). The effect is tentatively attributed to the protonic doping of the polymer chains by silanol groups of the hydrolyzed trichlorosilanes available within the partially polymerized siloxane network. The doped polymer films exhibited a very good stability in high vacuum and nonpolar gases and showed an interesting electrical response to polar vapors. These effects point to an attractive new route of doping of conjugated polymers that might be interesting for applications in molecular sensors, transparent conductors, and organic electronics.

4. Experimental

Regioregular P3HT from Alfa-Aesar and P3HTT from Merck were dissolved in chloroform and chlorobenzene, respectively. The concentration of P3HT in chloroform was 1.0 mg mL^{-1} (0.07 wt%). The concentration of P3HTT in chlorobenzene was 0.5 wt%. In the case of P3HTT, hot was applied through a water bath to dissolve it thoroughly. Both solutions were spin-coated on glass substrates at 2000 rpm for 40 sec in ambient air. The spin-coated P3HT and P3HTT films were then annealed at $160\text{--}180^\circ\text{C}$ for 10 min in a flow of UHP Ar. The film thickness was $20 \pm 3 \text{ nm}$, as determined by AFM. Handling of annealed samples was done in ambient air. An aqueous solution of colloidal graphite (Ted Pella, Redding, CA) was deposited onto the two opposite edges of the annealed samples to form electrical contacts, defining an approximately square film with a width and length of $1 \pm 0.1 \text{ cm}$. After the graphite paint was dried, samples were placed on a sample holder for electrical measurements and loaded into an FTS treatment chamber. The chamber was evacuated by a chemically resistive mechanical pump that used Solvay Solids Fomblin SV inert PFPE fluid (Kurt J. Lesker, Clairton, PA) with an extremely low backstreaming rate. Electrical measurements were performed using Keithley (Cleveland, OH) K2400 source-meters and K6512 electrometers. SEM and AFM images were collected using a Sirion SEM (FEI Company, Hillsboro, OR) and a Pacific Nanotechnology AFM (Santa Clara, CA), respectively. Optical absorption spectra were measured with an Ocean Optics transmittance spectrometer (Dunedin, FL).

Acknowledgements

This work was supported by the NSF ECCS 0822036 grant and Rutgers Academic Excellence Fund 2-35153.

Received: January 12, 2009
Published online: May 4, 2009

- [1] *Organic Field-Effect Transistors* (Eds Z. Bao, J. Locklin), Taylor & Francis, London, UK 2007.
- [2] C. Reese, M. Roberts, M. M. Ling, Z. Bao, *Mater. Today* 2004, 7, 20.
- [3] S. R. Wasserman, Y. T. Tao, G. M. Whitesides, *Langmuir* 1989, 5, 1074.
- [4] H. B. Akerman, P. W. M. Blom, D. M. de Leeuw, B. de Boer, *Nature* 2006, 441, 69.

- [5] N. B. Zhitenev, A. Erbe, Z. Bao, *Phys. Rev. Lett.* 2004, 92, 136805.
- [6] M. F. Gohoun, J. Sanchez, D. Clays, M. E. Gershenson, V. Podzorov, *Nat. Mater.* 2008, 8, 84.
- [7] R. J. Haeger, *Radiat. Mat. Phys.* 2001, 71, 681.
- [8] R. D. McCullough, *Adv. Mater.* 1998, 10, 93.
- [9] M. J. Pinner, C. D. Frisbie, *Adv. Funct. Mater.* 2006, 16, 1051.
- [10] J. C. Love, L. A. Estroff, J. K. Kriebel, R. G. Nuzzo, G. M. Whitesides, *Chem. Rev.* 2005, 105, 1103.
- [11] A. Bechtem, M.-H. Yoon, T. J. Marks, *Adv. Mater.* 2005, 17, 1705.
- [12] A. Salomon, T. Bockling, C. K. Chan, F. Amy, O. Grubbeitz, D. Cahen, A. Kahn, *Phys. Rev. Lett.* 2005, 95, 266307.
- [13] Y.-L. Lo, J. W. P. Hsu, R. L. Willett, K. W. Baldwin, K. W. West, J. A. Rogers, J. Vac. Sci. Technol., 2002, 20, 2833.
- [14] L. L. Chua, J. Zoumal, J. F. Chang, E. C. W. Ou, P. K. H. Ho, H. Srimangshu, R. H. Friend, *Nature* 2005, 434, 194.
- [15] H. C. Yang, T. J. Shin, M. M. Ling, K. Cho, C. Y. Rye, Z. Bao, *J. Am. Chem. Soc.* 2005, 127, 11542.
- [16] A. J. Epstein, *MRS Bull.* 1997, 22, 16.
- [17] K. Lee, S. Cho, S. H. Park, A. J. Haeger, C.-W. Lee, S.-H. Lee, *Nature* 2006, 441, 65.
- [18] A. J. Haeger, *Angew. Chem. Int. Ed.* 2001, 40, 2591.
- [19] Z. Bao, A. Dodabalapur, A. J. Lovinger, *Appl. Phys. Lett.* 1996, 69, 4103.
- [20] I. McCulloch, M. Heeney, C. Bailey, K. Gernardus, I. McDonald, M. Shklyarsky, D. Sparrow, S. Tierney, R. Wagner, W. Zhang, M. L. Chalmers, R. J. Kline, L. D. McCulloch, M. E. Tunney, *Nat. Mater.* 2006, 5, 328.
- [21] H. Srimangshu, P. J. Brown, R. H. Friend, M. M. Nielsen, K. Bechgaard, B. M. W. Langeveld-Voss, A. J. H. Spiering, R. A. J. Janssen, E. W. Meijer, P. Henning, D. M. de Leeuw, *Nature* 1999, 401, 655.
- [22] A. Salom, *Mater. Today* 2007, 10, 38.
- [23] M. L. Chalmers, M. E. Tunney, R. J. Kline, I. McCulloch, M. Heeney, *J. Am. Chem. Soc.* 2007, 129, 3226.
- [24] a) A. S. Wan, D. Mastroianni, B. Lee, E. Garfunkel, L. E. Feldman, V. Podzorov, unpublished. b) A. S. Wan, D. Mastroianni, B. Lee, E. Garfunkel, L. E. Feldman, V. Podzorov, unpublished. c) L. C. Feldman, J. W. Mayer, *Fundamentals of Surface and Thin Film Analysis*, North Holland-Elsevier, New York 1986.
- [25] Y. Wang, M. Lieberman, *Langmuir* 2003, 19, 1159.
- [26] C. R. Topp, M. L. Hatz, *Langmuir* 1992, 8, 1120.
- [27] M. L. Chalmers, R. A. Street, J. E. Northrup, *Appl. Phys. Lett.* 2007, 90, 123508.
- [28] P. D. Lickiss, *Adv. Inorg. Chem.* 1995, 42, 147.
- [29] R. Zhang, B. Li, M. C. Jara, M. Jellison-B, G. Savva, J. Cooper, S. J. Jia, S. Tristram-Nagle, D. M. Semak, D. N. Lambeth, R. D. McCulloch, T. Kowalczyk, *J. Am. Chem. Soc.* 2006, 128, 3480.
- [30] H. Yang, J. W. Lefmans, C. Y. Rye, Z. Bao, *Appl. Phys. Lett.* 2007, 90, 172116.
- [31] J. Kim, T. M. Swager, *Nature* 2001, 411, 1030.
- [32] T.-C. Chung, J. H. Koo, A. J. Haeger, F. Wudl, *Phys. Rev. B* 1994, 50, 702.
- [33] Y. H. Kim, D. Spiegel, S. Hotta, A. J. Haeger, *Phys. Rev. B* 1988, 38, 5490.
- [34] A. G. MacDiarmid, A. J. Epstein, *Synth. Met.* 1995, 68, 85.
- [35] J. E. Yoo, J. L. Cross, T. L. Buchholz, K. S. Lee, M. P. E. Lee, Y.-L. Lo, *J. Mater. Chem.* 2007, 17, 1268.
- [36] M. Uggdang, R. Lazzaroni, S. Stafström, W. R. Salaneck, J.-L. Brédas, *Phys. Rev. Lett.* 1989, 63, 1841.
- [37] X. Jiang, E. Oosterbacka, O. Konovalov, C. P. An, B. Horowitz, E. A. J. Janssen, Z. V. Vardeny, *Adv. Funct. Mater.* 2002, 12, 587.
- [38] Z. Q. Li, G. M. Wang, N. Sai, D. Moen, M. C. Martin, M. Di Ventra, A. J. Haeger, D. N. Basov, *Nano Lett.* 2006, 6, 224.
- [39] Z. Q. Li, V. Podzorov, N. Sai, M. C. Martin, M. E. Gershenson, M. Di Ventra, D. N. Basov, *Phys. Rev. Lett.* 2007, 91, 016403.

Curriculum Vitae

Bumsu Lee

Education

- Ph.D.**, Physics May 2012
 Organic Semiconductors Experiments (Advisor : Prof. Vitaly Podzorov)
 Department of Physics and Astronomy
 Rutgers University, NJ
- M.S.**, Physics 2004
 Theoretical Nuclear Physics (Advisor: Prof. Suhong Lee)
 Yonsei University, Seoul, Korea
- B.S.**, Physics *Graduated with Honors* 2002
 Yonsei University, Seoul, Korea

Publications

- [12] **B. Lee**, B. Yakshinskiy, R. A. Bartynski and V. Podzorov, “*Impact of photooxidation on charge transport of rubrene OFETs combined with XPS investigation*” in preparation (2012).
- [11] **B. Lee**, D. Fu, K. Czelen and V. Podzorov, “Anisotropic Surface Conductivity and Hall-effect at Organic Charge Transfer Interface” to be submitted (2012).
- [10] **B. Lee**, Y. Chen and V. Podzorov, “*Doping of Carbon Nanotube by Organosilane Self-assembled monolayers*” submitted (2012).
- [9] Y. Chen, **B. Lee**, D. Fu and V. Podzorov, “*Origin of 650nm photoluminescence band in Rubrene*”, **Adv. Mater.** 23, 5370 (2011).
- [8] D. J. Ellison, **B. Lee**, V. Podzorov and C. D. Frisbie, “*Surface potential mapping of SAM-functionalized organic semiconductors by Kelvin Probe Force Microscopy*”, **Adv. Mater.** 23, 502 (2011).
- [7] H. Najafov, **B. Lee**, Q. Zhou, L. C. Feldman and V. Podzorov, “*Observation of long-range exciton diffusion in highly ordered organic semiconductors*”, **Nature Mater.** 9, 938 (2010).
- [6] **B. Lee**, A. Wan, D. Mastrogiiovanni, J. E. Anthony, E. Garfunkel and V. Podzorov, “*Origin of the bias stress instability in organic field-effect transistors*”, **Phys. Rev. B** 82, 085302 (2010).
- [5] **B. Lee**, Y. Chen, F. Duerr, D. Mastrogiiovanni, E. Garfunkel, E. Y. Andrei and V. Podzorov, “*Modification of electronic properties of graphene with self-assembled*

monolayers”, **Nano Lett.** 10, 2427-2432 (2010).

[4] O. Khatib, **B. Lee**, J. Yuen, Z. Q. Li, M. Di Ventra, A. J. Heeger, V. Podzorov, and D. N. Basov, “*Infrared signatures of high carrier densities induced in semiconducting poly(3-hexylthiophene) by fluorinated organosilane molecules*”, **J. Appl. Phys.** 107, 123702 (2010).

[3] W. Leszek, S. Katalinic, **B. Lee**, M. Connors, E. Garfunkel, L.C. Feldman and V. Podzorov, “*Ion-scattering analysis of self-assembled monolayers of silanes on organic semiconductors*”, **Nucl. Inst. & Meth. Phys. Res. Sec. B-Beam. Intraction Mater. Atoms** 268, 1889 (2010)

[2] **B. Lee**, T.-J. Choi, S.-W. Cheong and V. Podzorov, “*Nanoscale conducting channels at the surface of organic semiconductors formed by decoration of molecular steps with self-assembled molecules*”, **Adv. Funct. Mater.** 19, 3726 (2009).

[1] C.-Y. Kao, **B. Lee**, L. S. Wielunski, M. Heeney, I. McCulloch, E. Garfunkel, L. C. Feldman and V. Podzorov, “*Doping of conjugated polythiophenes with alkyl silanes*”, **Adv. Funct. Mater.** 19, 1 (2009).